IMAGING THE REALM OF THE STRONGLY CORRELATED: VISUALIZING HEAVY FERMION FORMATION AND THE IMPACT OF KONDO HOLES IN URu_2Si_2

A Dissertation

Presented to the Faculty of the Graduate School

of Cornell University

in Partial Fulfillment of the Requirements for the Degree of

Doctor of Philosophy

by

Mohammad H. Hamidian

May 2011

IMAGING THE REALM OF THE STRONGLY CORRELATED: VISUALIZING HEAVY FERMION FORMATION AND THE IMPACT OF KONDO HOLES IN URu_2Si_2

Mohammad H. Hamidian, Ph.D.

Cornell University 2011

The methods of spectroscopic imaging scanning tunneling microscopy (SI-STM) are used to study the physics of heavy fermion compounds. The representative sample, URu_2Si_2, notable for its elusive 'hidden' order state below $T_0 = 17.5K$, exhibits the spectroscopic spatial image of a Kondo lattice via the Fano lattice observed through conductance measurements on the Si-terminated surface. The periodic array of Fano spectra observed above T_0 describe a system of many-body states commensurate with the U-atom matrix. Descending into the 'hidden' order phase these spectra develop a soft gap and the local density of states on the U-terminated surface show a simultaneous redistribution of spectral weight near the chemical potential. At the same time that spatial signatures accompany the onset of the 'hidden' order, the momentum space structure shows the splitting of a light band, crossing the chemical potential at $\mathbf{Q}^* \approx 0.3(2\pi/a_0)$ into two new heavy bands in splendid accord with Kondo lattice theory. The ensuing effective mass of $m^* \approx 30m_e$, is in accord with bulk thermodynamic measurements demonstrating that most if not all of the density of states about the chemical potential is contained in the newly formed heavy bands. The exact relationship between the 'hidden' order and the formation of a heavy fermion electronic structure is most likely a bootstrap effect and further investigations are needed to understand the link.

Having established the robust heavy fermion character of URu_2Si_2 at low temperature, the first known spectroscopic visualization studies of the effect of Kondo holes is made. The consequence of removing local moments, which contribute to the formation of heavy quasiparticles, achieved by replacing a small number of U-atoms with Th-atoms, produces spatial ripples in the hybridization strength between the Fermi sea and the f-states. Astonishingly, the period of oscillations is not associated with any wavevector on the Fermi surface of the heavy state, but rather with the Fermi wavevector $\mathbf{Q}^*$ of the unhybridized electronic structure. Calculations of the Kondo hole response of an Anderson lattice model directly confirm these observations and further support that URu_2Si_2 exhibits an almost conventional behavior of a heavy fermion material.

BIOGRAPHICAL SKETCH

Mohammad Hossein Hamidian was born in Isfahan, Iran in 1980, where he spent the first six years of his life before immigrating to Canada with his family. Growing up in Toronto, Mohammad commenced his science career at the University of Toronto pursuing undergraduate studies in Engineering Science and mathematics. Specializing in the field of engineering physics, his early research included experimental work on the forward calorimeter of the ATLAS project at C.E.R.N. and theoretical work for his senior thesis on group theoretic methods for quantum dynamical problems. He continued with theoretical physics at Toronto earning him a Masters degree in the study of the ocean dynamics of the El-Niño Southern Oscillation and the application of solitary wave theory to describe the phenomenon. Seeking a change of venue, Mohammad moved to Ithaca, New York in 2005 and began his Ph.D. at Cornell University under the guidance of J.C. Séamus Davis in the field of strongly correlated electronic materials. Much to the dismay of his advisor, Mohammad also invests in many other serious pursuits including classical piano performance, triathlons, and the culinary arts.

اکنون می دانیم که از راه مطالعه علل و
سرمنشاء اتفاقات (اصولا اگر علل و
سرمنشایی وجود داشته باشد) دانش نه
کسب می شود و نه کامل می گردد، مگر این
که از خود اتفاقات و حواشی آن نیز آگاهی
داشته باشیم.

AVICENNA (980-1037)

To my family and friends, the pillars of my support through the trials of science

ACKNOWLEDGEMENTS

There are no greater contributors to my success than my parents, Elahe and Bijan. From their immensely difficult journey from Iran to Canada with me in hand to the endless support, love, and selflessness from thereon, there is no way to thank them for how much they have done. Till the very last few months of my Ph.D. they would call everyday, sometimes twice a day, to make sure I was eating, sleeping, and still sane. And beyond the support for my education, they instilled on me a sense of compassion, determination and perseverance. They also taught me to never forget my Iranian heritage.

My younger brother, Arman, is in some ways quite different than I am but we both share the desire to make the world a better place. He deserves my thanks for his humor, spontaneity, and the wrestling matches. My uncle, Amir, whom I consider an older brother, has been my role model not only because of an extremely rational mind, a level head, and a curiosity for learning but for his boundless sense of responsibility and love for his family. Of course, where would I be without my grandmother Maheen, who always told me to have fun and enjoy life. Every one of my girlfriends has loved my grandmother! To the rest of my wonderful family, Aziz, Assi, Bahareh, Shaheen, Yashar, Reyhaneh, Gholamreza, Shadi, Saghi, Farhang, Reza, Maryam, Farshad, Inge, Armin, Anice, Gazaleh, and Masoud, thank you for adding brightness and color to the last five and a half years.

Life in Ithaca could not have been as wonderful as it was without the company of wonderful friends. Amgad, my first roomate in Ithaca had an infectious smile and wonderful outlook on life. Darren was my equal crazy, revising homework solutions starting at 3:00am in first year, and my unwavering friend even as he moved to Europe to finish his degree. His heart is as big as his shoes,

and I cannot express enough gratitude for the last few months in particular. Tien, you strength and resolve were inspirational. Robin, thanks for always remembering me and helping our friendship mature. Frank, you were my pillar in Solid State II and I'll never forget Florida spring break! Tristan, who took my friendly jibes for years, never failed to come through from saving me on the side of a road from a flat bike tire, or helping me design RF circuits. Bryan 'Peahces', we will always have the trilogy of sketches. Dave, with all of the ups and downs we both made it. Pooneh, thanks for being there during the good and the hard times. Jay, no one could roast me as well as you and make me laugh so hard about it. Julia, you stand as the one person who has baked the most cakes for me at Cornell. Your kindness and generosity will always be remembered. Ted, thanks for the lively discussions of art, music, politics, the intelligence of experimentalists versus theorists and just for understanding. Chris, you took my outdoors experiences to a whole new level and if we had to get stuck on a really windy mountain again I know we'd make it. Sheryl, your strength of character and your composure are inspiring. Thanks for helping me get to the finish line in one piece. Annie, your generosity and spirit always lifted mine. Carolyn, while you would always claim that you didn't understand my research you were certainly one of the most relentlessly encouraging and in trying times that meant a lot. Mark taught me that even at the busiest of times, one can always take a break to enjoy life, build a snow man and have a beer. My fellow Canadian compatriot, Ben, your friendship and support, our dinner parties, our discussions, late nights at the bar after being in the lab made me appreciate my time at Cornell in a completely new way. Vivi, thank you for sharing wisdom, good gin, wonderful food, joie de vivre and unwavering encouragement and unending true friendship. Sarah, I cannot even begin to imagine what the last

few months would have been without your help. You sat with me at Stella's for weeks as I worked on my defense and made sure I never felt alone. Thanks for climbing with me to the summit.

My life in the lab has been deeply enriched by my colleagues whom I am also happy to call my friends. Milan, you gave me that first essential piece of STM code to get me going so this thesis is partially your fault! Thanks for invaluable conversations about physics, coding, science politics, and joining me for expensive dinners. Ming, your skill and spirit are inspiring only second to your wonderful humor and light heartedness which made working with you a pleasure. Kazu, your extreme generosity, willingness to help and vast knowledge made my transition to the cuprate world much smoother. I have been most fortunate within the last year to have been joined by a wonderful lab mate on STM2, Inês. From helping me prepare figures, being on top of lab matters and extremely insightful, for never letting my glass run empty and caring for my well being, she deserves special gratitude.

My development as a scientist and experimental physicist were greatly enhanced by two of my friends and colleagues. Ethan, who had the 'pleasure' of initiating me into the world of low temperature physics taught me that all problems can be solved, the need for exacting standards, and that every design must be a composite of foresightful functionality and elegance. Andy, whom I met as I joined the STM world instilled in me that every data set must be of the highest quality and that it can always be made better. His deeply insightful understanding of physics helped push my own to a whole new level. Balancing the analytical side with the artistic side, my piano teacher, Sezi, teacher for the last several years deserves special recognition. Having to deal with my lack of practice time she still continued to challenge me and further my musicianship.

I am grateful to her for sharing in my journey and helping me reach my artistic aspirations.

I finally turn to my research committee. While I have warned other graduate students of putting experts in their field on their committee, my thesis and scientific work has greatly benefitted from both Professor Kyle Shen and Professor Eun-Ah Kim's keen eye, wealth of knowledge, and high standards. They would not let me settle for anything less than my full capability would offer. And to Professor Séamus Davis, my advisor, who has taught me to sharpen my decision making, to ask the really important fundamental questions, to always dig deeper, to never let a theorist set an experimentalist's agenda and to always be prepared to defend my beliefs I express a heart-felt gratitude. To be immersed in a vibrant, influential and always active research program has been a wonderful, challenging, and rewarding experience. My time as a Ph.D. student could not have been more well spent.

TABLE OF CONTENTS

LIST OF FIGURES

CHAPTER 1

INTRODUCTION

> If the earth were taken into very cold regions, for instance, to those of Jupiter or Saturn, the water of our rivers and oceans would be changed into solid mountains. The air, or at least some of its constituents, would cease to remain an invisible gas and would turn into the liquid state. A transformation of this kind would thus produce new liquids of which we as yet have no idea.
>
> Antoine Lavoisier (1743-1794)

1.1 The Realm of the Correlated

If metals were the only materials we encountered then our understanding of the full implications of physical laws in condensed matter systems would be severely truncated. For it is a fantastic observation that even though we are able to concretely state such laws, their aggregate manifestations in collective many-body systems, innumerably varied, are unexpected, surprising, and mysterious. Of course, even metals, which can be almost completely described in the context of a non-interacting electron gas, are themselves far from simple for exactly the reason that the strong electromagnetic interactions of the constituent electrons should yield something far more complicated. The Fermi liquid resolution, in terms of composite quasiparticles emerging from a sea of mutually screened electrons is then the starting point from which any residual interactions are the basis for behavior beyond that of a 'simple' metal.

Strongly correlated materials are those for which the residual interactions are extreme and the last 30 years in the field are marked by fantastic discov-

eries of their kind including heavy fermions [1], the fractional quantum Hall effect [2], and high temperature superconductivity [3]. With each new exotic material comes the need for new techniques both theoretical and experimental to describe the tapestry of interactions and the range of novel behavior which ensue.

The scope of this dissertation focuses on the heavy fermions and one of its most studied oddities, the 'hidden' order phase of URu_2Si_2. While there is a basic premise for understanding this class of materials, there remains a great deal of confusion regarding the spectrum of observations which seem not to consistently fall within the paradigms of the underlying theory. As the active physics crucially involves the strong interactions of localized and delocalized states there is a need for simultaneously measuring both elements. Thus, the presentation of heavy fermion materials is within the context of employing a new probe capable of such a feat, the scanning tunneling micrscope, and the associated techniques of scanning imaging spectroscopy, to explore the fundamental characteristics of these strongly correlated systems.

1.2 Probing the Correlated - SI-STM

1.2.1 Tunneling Spectroscopy

Understanding the single-particle behavior of condensed matter system requires a way to measure how electrons propagate as a function of energy. The most straight forward way to achieve this is to insert or extract an electron at a definite energy and in general there are very few ways to do this because most

probes measure two-particle properties. For example, the response to an electromagnetic field couples to the charge or current and effectively is a measure of the charge-charge or current-current correlation functions which are two-particle propagators [4].

The only way to measure the single-particle properties is to insert/remove an electron into/out of a many-body system. Tunneling methods, originally and beautifully pioneered by Giaver to study superconductivity [5] provide the most direct way, though perhaps not the easiest to implement. The experimental setup consists of bringing into proximity two conducting materials such that they are separated by an insulating layer whereby the traversal of electrons can only happen via quantum tunnelling. Each system has its own respective Hamiltonian composed of single particle operators $c_{1,\mu}$ and $c_{2,\nu}$, with μ and ν being the respective quantum numbers of the individual complete bases. The coupling of the two systems, facilitated by the finite overlap of their wavefunctions gives rise to a term in the Hamiltonian for the aggregate system:

$$H_T = \sum_{\mu,\nu} \left(T_{\mu\nu} c_{1,\mu}^\dagger c_{2,\nu} + T_{\mu\nu}^* c_{2,\nu}^\dagger c_{2,\mu} \right). \tag{1.1}$$

$T_{\mu\nu}$ is tunnel matrix element defined in terms of the wave functions of each of the isolated systems and the first quantized one particle Hamiltonian $H(\mathbf{r})$,

$$T_{\mu\nu} = \int d\mathbf{r} \psi_\mu^*(\mathbf{r}) H(\mathbf{r}) \psi_\nu(\mathbf{r}). \tag{1.2}$$

The steady state current through the tunnel junction is just the average rate of the change of particles, $I_T = -e\langle \dot{N}_1 \rangle_t$ and thus by the Ehrenfest theorem

$$I_T = i[H_T, N_1] = -i \sum_{\mu,\nu} \left(T_{\mu\nu} c_{1,\mu}^\dagger c_{2,\nu} - T_{\mu\nu}^* c_{2,\nu}^\dagger c_{2,\mu} \right). \tag{1.3}$$

For current to flow there must be a shift in the chemical potential between the two sides of the barrier which can be realized by applying a voltage V. For

weak coupling, in which a large tunneling barrier diminishes the perturbations of one system on the other due to the exponential suppression of the tunnel matrix element, the current can be calculated to lowest order in the coupling using linear response theory [4],

$$I_T = \int_{-\infty}^{\infty} \frac{d\omega}{2\pi} \sum_{\mu\nu} |T_{\mu\nu}|^2 A_1(\mu,\omega) A_2(\nu,\omega+eV)[f(\omega+eV) - f(\omega)], \tag{1.4}$$

where the A_i are the spectral functions of the individual systems, and f the Fermi-Dirac distribution. The last expression states that the tunneling current is dependent on two key factors: 1) the availability of states and 2) the density of states at a given energy. Therefore, by sweeping the voltage across the junction and measuring the current one can obtain information about $A_1(\mu,\omega)$.

To simplify the scheme, one of the systems can be replaced with a simple metal which, for a broad range of energies, would have a constant density of states. It is then permissible to make the approximation [4]

$$\sum_{\nu} |T_{\mu\nu}|^2 A_2(\nu,\omega+eV) \approx \text{const} \tag{1.5}$$

and subsequently calculate the conductance in the simplified form

$$\frac{dI_T}{dV}(eV) \propto \int_{-\infty}^{\infty} d\omega \left(-\frac{\partial f(\omega+eV)}{\partial\omega}\right) \sum_{\mu} A_1(\mu,\omega). \tag{1.6}$$

At low temperatures the Fermi-Dirac distribution becomes sharply peaked further reducing the the expression for the conductance to

$$\frac{dI_T}{dV}(eV) \propto \sum_{\mu} A_1(\mu,-eV). \tag{1.7}$$

Therefore, a measure of the conductance of the tunnel junction in which one system is a metal is equivalent to a measure of the spectral function of the other system. A schematic of this process is presented in figure 1.1.

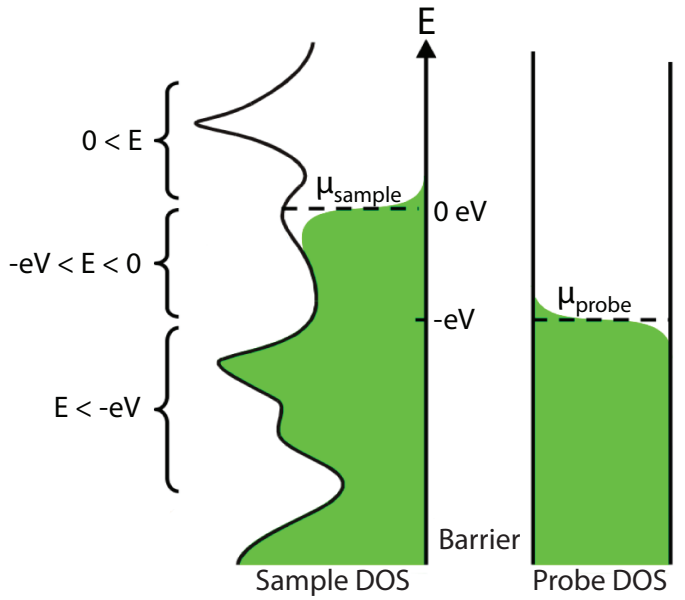

Figure 1.1: Schematic of tunneling spectroscopy. When a voltage V, is applied between a metal, the probing system, and another sample material, the shift in the chemical potential between the two allows for electrons to tunnel across the insulating barrier. In the graphic, the tunnel current is generated from electrons which tunnel from the filled states of the sample to the empty states of the probe in an the energy range $-eV < E < 0$. Figure adapted from [6]

There are inherent assumptions in deriving the above expressions. First, that both the probe and the sample are good conductors so that the electric field due to the applied bias falls to zero at the surface [7]. This allows for an accurate determination of the energies being probed. Requiring that the sample be a good conductor, however, also means that only a shallow layer of the sample can be probed: an injected electron from the probe would be screened at length scales comparable to the Thomas-Fermi screening depth, typically a few angstroms. Consequently, the second assumption embedded in equation 1.7 is that the spectral function is representative of the electronic states near the surface of the sample. Of course, it is possible and proven that in certain cases the surface measurements are representative of the bulk properties. Indeed, in all tunneling spectroscopy measurements great care needs to be taken to find the

connection before making any conclusions about the system under study.

1.2.2 Scanning Tunneling Spectroscopic Imaging

The presentation of tunneling spectroscopy in the last section assumed a geometry in which both sample and probe are equally spatially extended and that the current density is thus spatially uniform across the whole the sample. This is an example of a planar tunnel junction and is used to measure the average density of states (DOS) over an area large compared to interatomic distances. The Nobel prize winning *scanning tunneling microscope (STM)*, pioneered by Gerd Binning and Heinrich Rohrer at IBM Zürich in 1981 [8], replaces the planar metallic probe with an atomically sharp tip capable of being scanned over the surface of the sample so that the tunneling current is locally generated. Then in addition to an energy resolved measure of the sample's spectral function, spatial information can also be acquired.

Returning to equation 1.4 for the general form of the current, the tunneling matrix element acquires a specific form for a STM configuration in which the tip is spherically symmetric [7]

$$T_{\mu\nu} = \frac{\hbar^2}{2m} 4\pi \Omega_t^{-1/2} R \mathrm{e}^{-\kappa R} \psi_\nu(\mathbf{r}_0) \tag{1.8}$$

where κ is the minimum inverse decay length defined in terms of an effective work function, Ω_t is the tip volume, R the radius of curvature of the tip apex, and $\mathbf{r}_0$ the position of the center of curvature for the tip which also sets the minimum distance to the sample. Substituting this expression into equation 1.4 and changing to a real space basis [9] the tunneling current takes the form

$$I_T = \left| \frac{\hbar^2}{2m} 4\pi R \mathrm{e}^{-\kappa R} \right|^2 \int_{-\infty}^{\infty} \frac{d\omega}{\hbar} A_2(\mathbf{r}_0, \omega) g_1(\omega + eV)[f(\omega + eV) - f(\omega)] \tag{1.9}$$

where $g_1(\omega)$ is the density of states per unit volume of the tip. By once again assuming that the tip has a constant density of states for a large energy bandwidth and taking the low temperature limit, the tunneling conductance can be determined

$$\frac{dI_T}{dV} \propto R^2 \mathrm{e}^{-2\kappa R} g_1(\epsilon_F) A_2(\mathbf{r}_0, \omega = eV). \tag{1.10}$$

It is precisely because of this expression that an STM can resolve the spatial dependence of the spectral function, also known as the *local density of states* (LDOS).

Spectroscopic imaging entails the spatial mapping of the local density of states and serves as a powerful tool in the study of electron materials. Figure 1.2 illustrates how the collection of individual conductance spectra obtained over an area of a sample can be represented as a 3-dimensional stack, with each layer being a slice in energy of the LDOS over the entire field of view. Having access to the spatial variation in the LDOS opens up a whole new realm of analysis particularly suited for the study of strongly correlated systems, including maps of superconducting gaps, bosonic mode energies, work functions, dopant positions, and others also to be discussed further is this dissertation. One of the most impressive applications is that of *quasiparticle interference imaging* (QPI), providing access to not just the real space electronic structure but also to that of momentum space.

1.2.3 Imaging Quasiparticle Interference

Imaging standing waves in the electron density of a metal, Crommie, Lutz, and Eigler [10] were able to infer a great deal of information about the respective

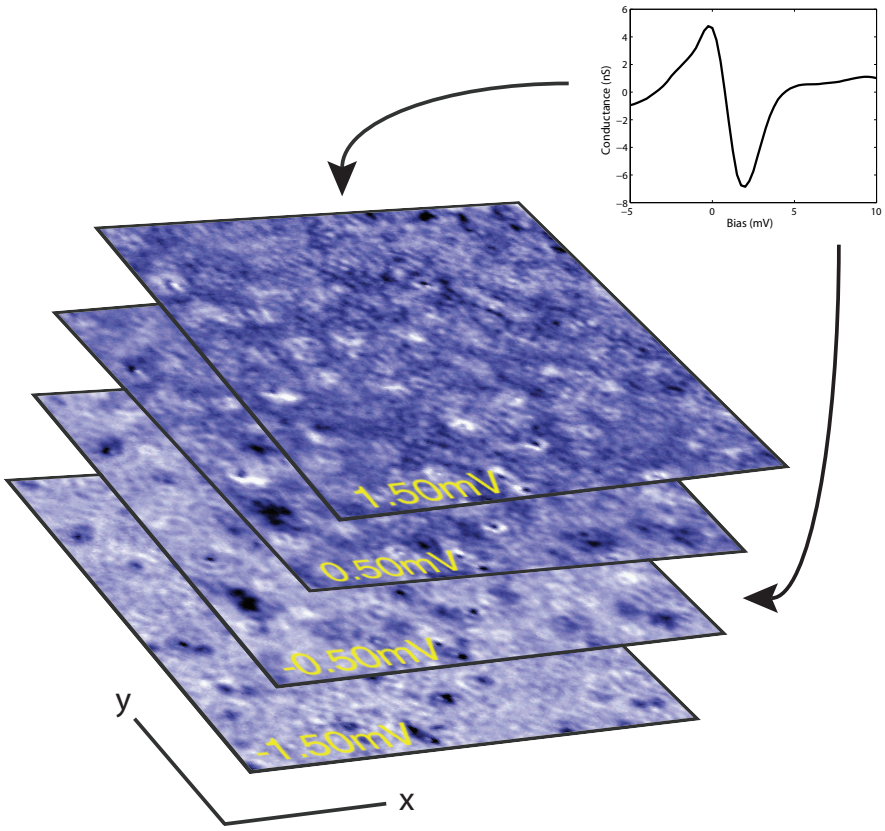

Figure 1.2: Illustration of Spectroscopic Imaging. Spectroscopic imaging involves the measurement of the the LDOS across a spatial area. The plot in the upper right hand corner represents a sample conductance spectrum as a function of the applied bias. By measuring across the entire field of view, the data can be represented a 3-dimensional stack resolved in spatial dimensions x and y, as well as energy E. Each sheet is a separate conductance layer proportional to the LDOS at the given energy.

band structure by relating the source of the oscillations to a Friedel response. The presence of defects in a sample which break translational invariance perturb the Hamiltonian of the clean system for which Bloch momentum states are the associated basis set. The new eigenstates of the perturbed Hamiltonian, a mixture of the original basis states, no longer have the same translational symmetry as the underlying clean system and thus project out onto the conjugate variable representation in real space.

Consider an equivalent description in terms of interference effects. The clean system can be represented by a set of Bloch states commensurate with the symmetry of lattice, $\Psi_{\mathbf{k}}(\mathbf{r}) = e^{i\mathbf{k}\cdot\mathbf{r}}u_{\mathbf{k}}(\mathbf{r})$. Consequently, the LDOS, $\rho(\mathbf{r},\omega) = \sum_{\mathbf{k}}|\Psi_{\mathbf{k}}|^2\delta(\omega-\epsilon_{\mathbf{k}})$, only contains modulations of the underlying lattice. If scatterers are introduced into the system then elastic processes generate scattered states which are a combinations of Bloch states of equal energies, ϵ_κ: $\Psi_\kappa(\mathbf{r}) = a_1\Psi_{\mathbf{k}_1}(\mathbf{r}) + a_2\Psi_{\mathbf{k}_1}(\mathbf{r})$, with $\epsilon_\kappa = \epsilon_{\mathbf{k}_2} = \epsilon_{\mathbf{k}_2}$, where for simplicity only a mixture of two states is considered. The resulting LDOS in the dirty system then contains cross terms modulating with the momentum transfer wavevector $\mathbf{q}(\epsilon_\kappa) = \mathbf{k}_1(\epsilon_\kappa) - \mathbf{k}_2(\epsilon_\kappa)$:

$$|\Psi_\kappa(\mathbf{r})|^2 = |a_1u_{\mathbf{k}_1}|^2 + |a_2u_{\mathbf{k}_2}|^2 + a_1a_2^*u_{\mathbf{k}_1}u_{\mathbf{k}_2}^*e^{i(\mathbf{k}_1-\mathbf{k}_2)\cdot\mathbf{r}} + a_1^*a_2u_{\mathbf{k}_1}^*u_{\mathbf{k}_2}e^{-i(\mathbf{k}_1-\mathbf{k}_2)\cdot\mathbf{r}}. \qquad (1.11)$$

Thus, the modulations arising from elastic scattering imprint themselves on the LDOS and can be detected through spectroscopic imaging. As the wavelength of the interference oscillations contains information about the momentum states it is possible, in principle, to reconstruct the $\mathbf{k}$-space structure by first determining the $\mathbf{q}$ vectors.

While the argument above has been made for a simple metallic system, its application to strongly correlated systems including the cuprate high temperature superconductors [11, 12, 13], pnictide high temperature superconductors [14], and ruthenates [15] has been immensely successful. The extension to the heavy fermion field is one of the main topics of the present dissertation.

1.3 Experimental Apparatus

The implementation of a SI-STM requires a complex setup capable of carrying out ultra-sensitive measurements with angstrom scale spatial resolution and microvolt energy resolution at cryogenic temperatures. This entails 1) a mechanically rigid STM head , 2) an extremely stable electronic feedback system controlling actuators with high precision to scan the probe tip across a sample while simultaneously executing a protocol for spectroscopic data acquisition, 3) low noise amplifiers with picoamp sensitivity, 4) mechanically quiet refrigeration, and 5) a multi-stage vibration isolation system shielding the entire apparatus from the mechanical noise of the outside world.

A short description of the STM used in acquiring the data for this dissertation is given below. For greater detail the reader is referred to the Ph.D. thesis of C. Taylor [16].

1.3.1 Feedback Circuitry

Figure 1.3 illustrates a schematic of the basic STM feedback loop circuit. In constant-current mode, a constant bias voltage is applied by the Electronic Control Unit (ECU) across the tip-sample tunnel junction. The resulting current signal is fed into a current-to-voltage preamplifier before being recorded by the ECU. A standard feedback control algorithm executed by the ECU constantly adjusts the height of the tip relative to the sample surface in order to maintain a constant current. The actuator dedicated to the vertical motion of the tip is a piezo tube whose height can be regulated by the application of an ECU-supplied

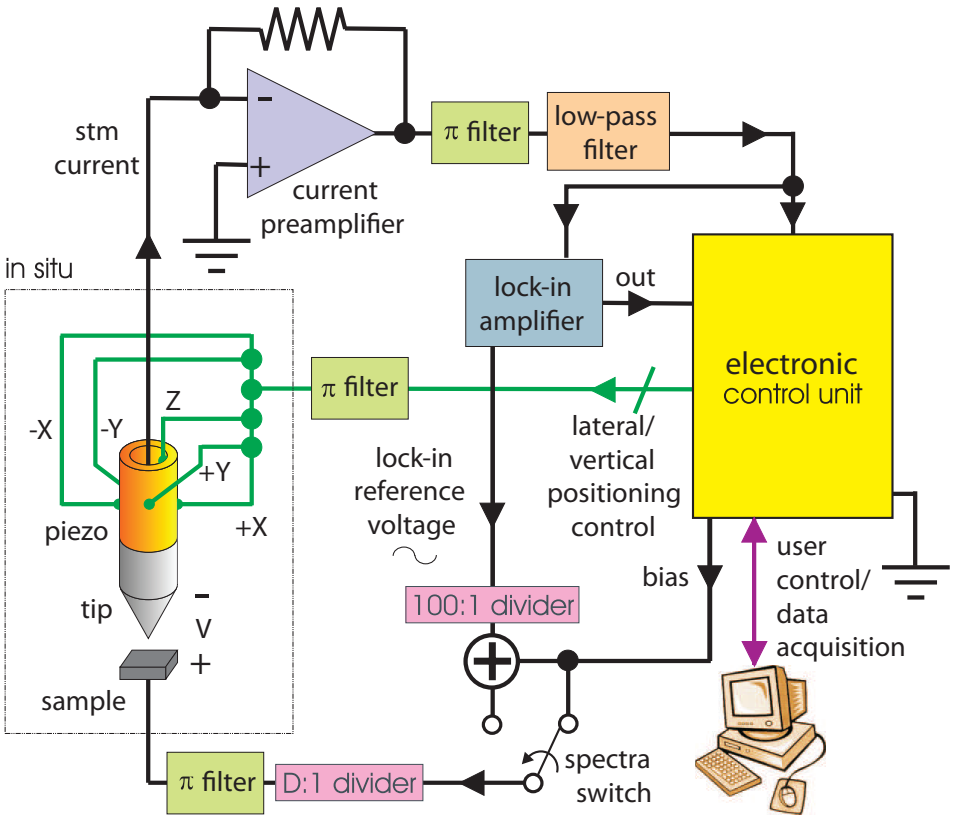

Figure 1.3: Schematic of STM feedback circuitry. The tunnel current arising from the tip-sample bias voltage, supplied by the ECU, is converted to a voltage signal by the current-to-voltage preamplifier and subsequently filtered before it is read by the ECU. In constant-current feedback mode, the ECU continuously adjusts the tip-sample distance by changing the Z-voltage on the piezo tube. Positioning along the sample surface is achieved by controlling the lateral X and Y voltages. For spectroscopic conductance measurements, a lock-in technique is used and the lock-in amplifier provides the necessary bias ripple and the measurement channel from which the ECU records the data. Adapted from [16]

voltage along the its length. In the same way, the lateral position of tip is controlled by applying a voltage perpendicular to the high symmetry direction of the piezo tube, in either the X or the Y directions.

In active tunneling feedback, the STM can be operated in constant-current topographic mode, with the X and Y voltages continuously swept to raster the tip across the sample surface. By following the feedback Z-piezo voltage needed

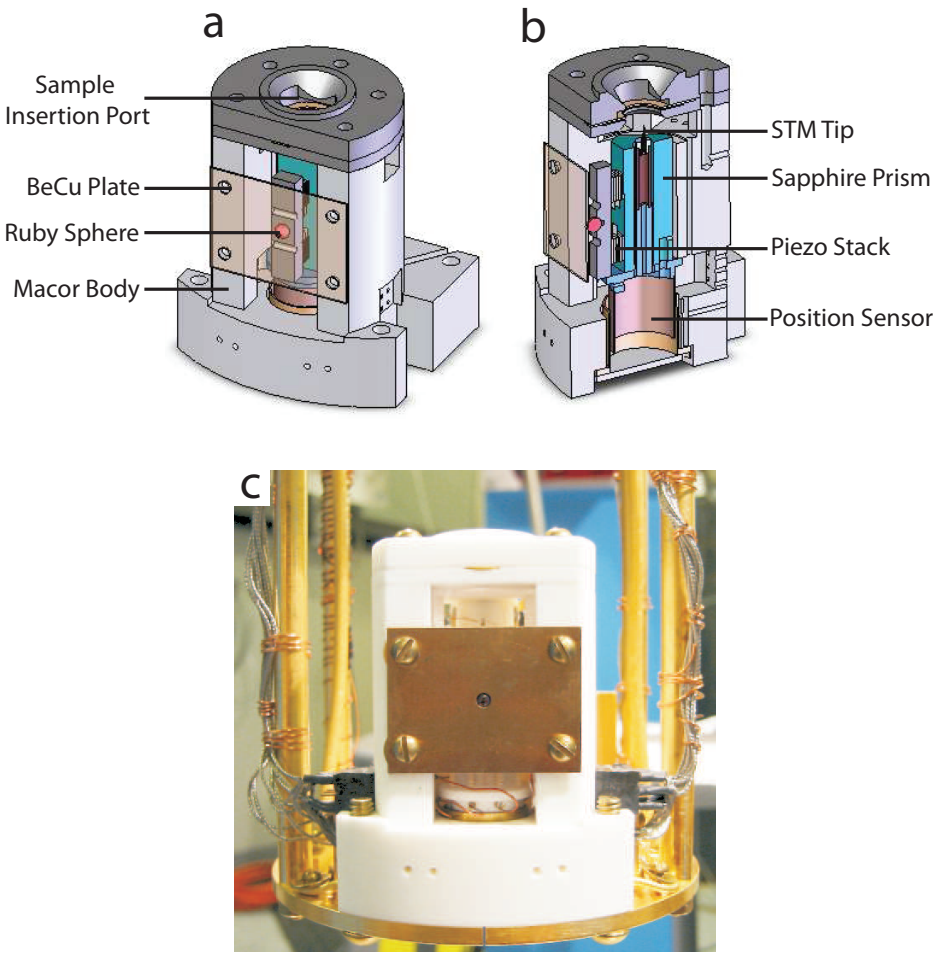

Figure 1.4: STM head. **a**, Front view. **b**, Sectioned view. **c**, Photograph of experiment STM head.

for constant-current operation, a height-resolved image of the surface can be obtained. Alternatively, by turning off the tunneling feedback, the tip can be parked at a height of specified junction resistance. Then the the applied bias voltage can be swept, the resulting current profile measured, and a bias dependent conductance calculated. In actuality, a lock-in technique is used to measure the conductance as it offers a far higher signal-to-noise ratio.

1.3.2 STM Head

The STM head provides the mounting stage for the sample under study and thus also encapsulates the set of all components needed to make measurements. The design described in this section is attributed to S. H. Pan, for which the details can be found in [17] and the references therein. Figure 1.4 shows the STM head and its essential components. The body is made of the ceramic Macor, a highly rigid material with high thermal but low electrical conductivity. The scanner assembly, comprised of the tip and scanner piezo tube, is housed within a highly-polished, sapphire, triangular prism held tightly in place by 6 shear piezo stacks mounted on the inside walls of the STM head and the BeCu plate. Coarse vertical motion of the scanner assembly is achieved by activating the piezo stacks and shifting the sapphire prism. The pressure against the stacks, regulating the coarse motion step size, is mediated by a small ruby sphere, and can be altered by adjusting the tension in the BeCu plate. For relative position measurements of the scanner assembly, two concentric conducting cylinders, one attached to the prism and the other to the STM body, form a capacitive sensor.

1.3.3 Vibration Isolation

Figure 1.5 depicts the inner and outer STM sound rooms which are designed for mechanical vibration isolation as well as RF shielding. The STM and the cryogenic probe on which it is mounted reside within the liquid He dewar. The dewar is affixed to a Pb filled triangular table weighing approximately 1.5 tons and mounted on three air springs. Each air spring in turn is supported by a

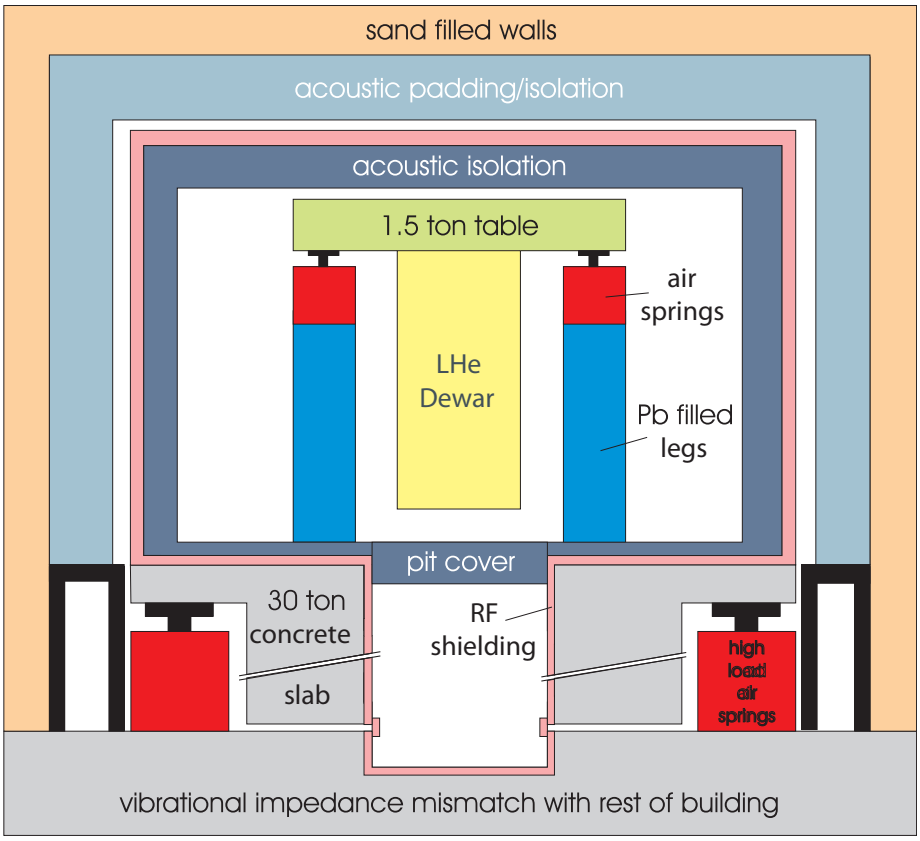

Figure 1.5: Vibration Isolation System. Adapted from [16]

wooden leg filled with a half ton of Pb. The resulting structure is extremely rigid whereas the air springs' vibration transfer function is peaked at only a few Hz. The assembly then rests on a large, 30-ton block of concrete which forms the perimeter of the inner experiment room. This inner room, outfitted with acoustic padding to insulate from external sound and a Faraday shield to reduce RF noise, itself sits on six larger air springs providing further mechanical isolation. Additional acoustic padding is mounted on the outer sound room whose walls are also filled with sand to provide acoustic dampening. Finally, the entire laboratory rests on a concrete foundation which has a mechanical impedance mismatch with the rest of the building.

REFERENCES FOR CHAPTER 1

[1] Andres, K., Graebner, J., and Ott, H. R. *Physical Review Letters* **35**, 1779–1782 (1975).

[2] Tsui, D. C., Stormer, H. L., and Gossard, A. C. *Physical Review Letters* **48**, 1559–1562 May (1982).

[3] Bednorz, J. G. and Müller, K. A. *Zeitschrift für Physik* **64**, 189–193 June (1986).

[4] Bruus, H. and Flensberg, K. *Many-Body Quantum Thoery in Condensed Matter Physics*. Oxford University Press, (2004).

[5] Giaever, I. *Physical Review Letters* **5**, 147–148 August (1960).

[6] Hoffman, J. E. *A Search for Alternative Electronic Order in the High Temperature Superconductor $Bi_2Sr_2CaCu_2O_{8+\delta}$ by Scanning Tunneling Microscopy*. Ph.D. Thesis, UC Berkeley, (2003).

[7] Wiesendanger, R. *Scanning Probe Micrscopy and Spectroscopy: Methods and Applications*. Cambridge University Press, (1994).

[8] Binnig, G., Rohrer, H., Gerber, C., and Weibel, E. *Applied Physics Letters* **40**, 178–180 (1982).

[9] Schmidt, A. R. *Quasiparticle Interference and the Impact of Strong Correlations on High Temperature Superconductivity*. Ph.D. Thesis, Cornell Univeristy, (2009).

[10] Crommie, M. F., Lutz, C. P., and Eigler, D. M. *Nature* **363**, 524–527 June (1993).

[11] Hoffman, J. E., McElroy, K., Lee, D. H., Lang, K. M., Eisaki, H., Uchida, S., and Davis, J. C. *Science* **297**, 1148–1151 (2002).

[12] McElroy, K., Simmonds, R. W., Hoffman, J. E., Lee, D.-H., Orenstein, J., Eisaki, H., Uchida, S., and Davis, J. C. *Nature* **422**, 592–596 April (2003).

[13] Kohsaka, Y., Taylor, C., Wahl, P., Schmidt, A., Lee, J., Fujita, K., Alldredge, J. W., McElroy, K., Lee, J., Eisaki, H., Uchida, S., Lee, D.-H., and Davis, J. C. *Nature* **454**, 1072–1078 August (2008).

[14] Chuang, T.-M., Allan, M. P., Lee, J., Xie, Y., Ni, N., Bud'ko, S. L., Boebinger, G. S., Canfield, P. C., and Davis, J. C. *Science* **327**, 181–184 January (2010).

[15] Lee, J., Allan, M. P., Wang, M. A., Farrell, J., Grigera, S. A., Baumberger, F., Davis, J. C., and Mackenzie, A. P. *Nature Physics* **5**, 800–804 September (2009).

[16] Taylor, C. *Coexistence of Bogoliubov Quasiparticles and Cluster Domains in Lightly Hole-Doped Cuprates*. Ph.D. Thesis, Cornell Univeristy, (2008).

[17] Pan, S. H., Hudson, E. W., and Davis, J. C. *Review of Scientific Instruments* **70**, 1459–1463 (1999).

CHAPTER 2

HEAVY FERMIONS AS A KONDO LATTICE

2.1 Introduction

The term heavy fermion originated in the late 1970s to describe the electronic excitations in a new class of intermetallic compound with an electronic density of states as much as 1000 times larger than copper. Since the original discovery of heavy-fermion behavior in $CeAl_3$ by Andres, Graebner and Ott [1], a diversity of additional heavy-fermion compounds, including superconductors, antiferromagnets, and insulators have been discovered.

The current class of heavy-fermion materials contain rare-earth or actinide ions, forming a matrix of localized magnetic moments at higher temperatures. The distinguishing physics of these materials originates from the interactions of the local moments with a sea of itinerant conduction electrons. In most rare-earth metals and insulators, local moments tend to order antiferromagnetically, but, in heavy-electron metals, as the temperature is lowered, the strong interactions of the local moments with delocalized electrons is fierce enough to melt the magnetic order.

Shortly after their initial discovery, Doniach [2] proposed a lattice extension of the Kondo effect to describe heavy fermion behavior. In the classic Kondo effect, a single magnetic ion leads to enhanced spin flip scattering processes as the temperature is lowered resulting in an upturn in resistivity,(figure 2.2a). At temperatures and magnetic fields below an energy scale defined by the Kondo temperature, T_K, the complex interaction ultimately forms a spinless scattering

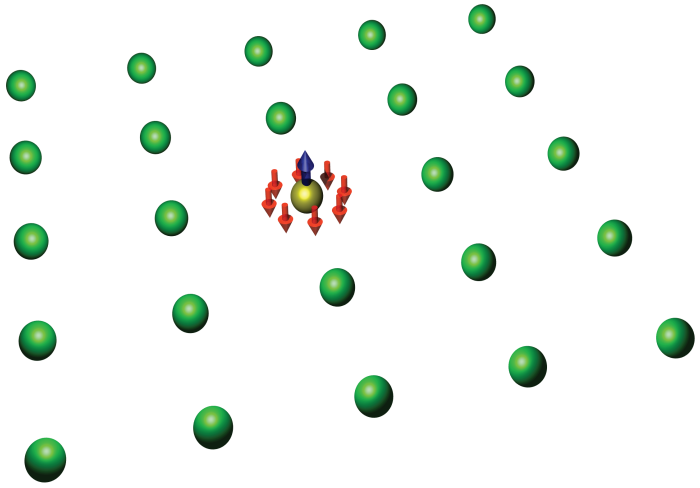

Figure 2.1: Screened Kondo impurity. At low temperatures the magnetic moment (blue) from the impurity atom (gold) is quenched by the conduction electrons (red).

center, with a quenching of the local moment (figure 2.1). In its original inception, the Kondo effect attributes the low temperature resistance minimum in metals to the strong elastic scattering potentials at magnetic impurity sites. When the same screening process takes place in a heavy fermion material, it leads to a spin quenching at every site in the lattice, except that the strong potential scattering at each site develops coherence, leading to a sudden drop in the resistivity at low temperatures (figure 2.2b). The net effect of the lattice Kondo effect is a profound transformation. The localized moments dissolve into the conduction sea thus increasing the volume of the Fermi surface. As mobile excitations, the newly dressed quasiparticles acquire charge and enhanced effective mass.

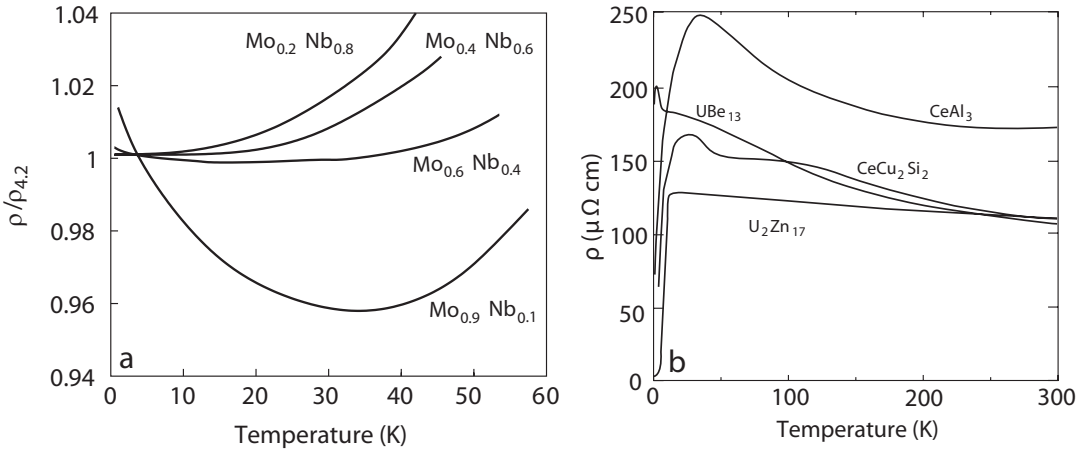

Figure 2.2: Resistivity of dilute Kondo and heavy fermion materials. **a**, The resistivity minimum in Mo_xNb_{1-x} resulting from the onset of enhanced potential scattering from the Kondo resonance centers which have developed around the magnetic Mo impurities for $x > 0.4$. **b**, The resistivity drops dramatically at low temperatures in heavy fermion materials, suggesting the development of phase coherent scattering from the Kondo resonance centers [3].

2.2 The Kondo Effect

2.2.1 Local Moment Formation - The Anderson Model

The Kondo effect is the physics of screening local moments for which the theory begins with the Anderson model:

$$H = \sum_{\mathbf{k},\sigma} \epsilon_{\mathbf{k}} n_{\mathbf{k}\sigma} + \sum_{\mathbf{k},\sigma} V(\mathbf{k}) \left[c^{\dagger}_{\mathbf{k}\sigma} f_{\sigma} + f^{\dagger}_{\sigma} c_{\mathbf{k}\sigma} \right] + \epsilon_f n_f + U n_{f\uparrow} n_{f\downarrow} \tag{2.1}$$

The first two terms describe the hybridization of f-electrons from the impurity ion with the set of delocalized states in the conduction sea. The last pair of terms describes the atomic limit of an isolated ion. The presence of impurity f-electrons embedded in a metal is not a sufficient condition for local moment formation. In the atomic limit, a magnetic ground state is obtained for a doublet, in which the localized f-states are singly occupied, $|f^1\ \uparrow\rangle$ and $|f^1\ \downarrow\rangle$, and for

which the excitation energies from this state are greater than zero. The energy condition sets up one of the essential constraints for local moment formation:

$$U/2 > |\epsilon_f + U/2| \tag{2.2}$$

In the opposite limit, the f electrons within the core of the impurity atom hybridize with the itinerant states of the surrounding electron sea. In the absence of any local correlations, the hybridization broadens the localized f-state, producing a resonance of width

$$\Gamma = \pi V^2 N(0) \tag{2.3}$$

where V^2 is the average of the hybridization matrix element around the Fermi surface, and $N(0)$ is the density of states at the Fermi level. When both the local and hybridization elements are combined, yielding an approximate model for an impurity atom embedded in a metal, a mean field solution demonstrates that local moments form only when $U > U_c \sim \Gamma\pi$. For example, a dilution of iron in niobium fails to form moments owing to the higher density of states and large Γ whereas a similar alloying in molybdenum satisfies $U > U_c$ allowing for local moments to form [3]. Figure 2.3 illustrates the two limits of the Anderson model and most importantly how increasing U splits the localized f-resonance in the density of states to form the local moments.

2.2.2 The Kondo Regime

The mean field description of the Anderson model, in terms of an effective hybridization strength, in equation 2.1, explains the formation of local moments but naturally does not capture the effect of fluctuations which are essential to the

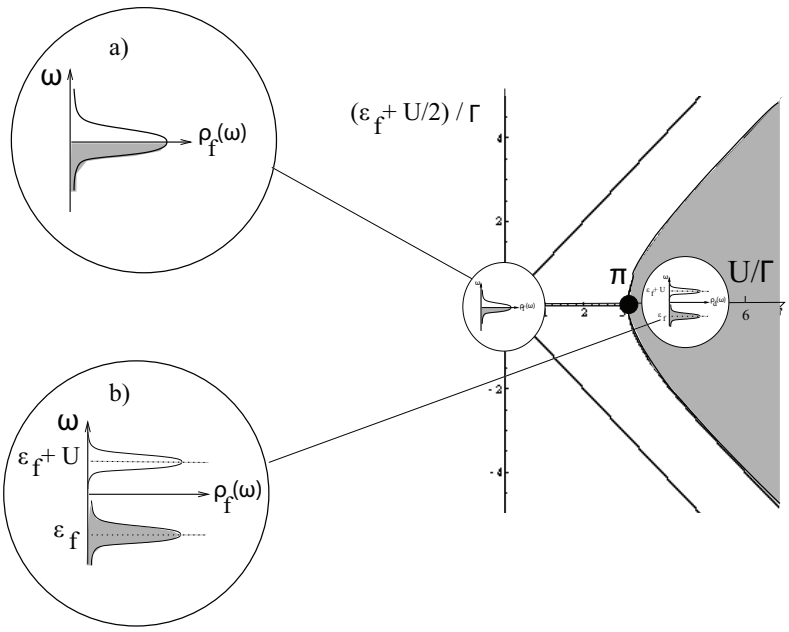

Figure 2.3: Splitting of the f-electron resonance density of states to form local moments. **a**, $U < \Gamma\pi$, formation of a single resonance state dominated by the hybridization of the localized f-states with the conduction electrons. **b**, $U > \Gamma\pi$, splitting of the resonance by an energy U, attributed to the effect of local correlations, which forms the local moments. [4]

physics of the Kondo effect. Once the local moment is formed, the purely spin degrees of freedom which remain interact with the conduction sea. Whereas the large on-site repulsion makes it energetically unfavorable for additional electrons to occupy the impurity f-levels, virtual charge fluctuations lead to spin-exchange in between the local moment and the itinerant background. By considering the allowed intermediate states in the second-order exchange processes, including their energies and symmetries, the interaction must be antiferromagnetic and have the form

$$H_{int} = J\sigma(0) \cdot \mathbf{S}_f \tag{2.4}$$

where $\mathbf{S}_f$ is the spin of the localized moment, $\sigma(0)$ is the electron spin density operator of the background states, and J is the spin-exchange coefficient $\sim V^2/U$.

Finally the *Kondo Model* can be stated as

$$H_{Kondo} = \sum_{\mathbf{k},\sigma} \epsilon_{\mathbf{k}} n_{\mathbf{k}\sigma} + J\sigma(0) \cdot \mathbf{S}_f \tag{2.5}$$

describing a simple point-interaction between the spin density of the metal and the local moment [3, 5].

A complete derivation of the Kondo model involves the renormalization of energy scales. The energy associated with valence fluctuations in the Anderson model are on the order of several electronvolts whereas the key features which develop from the Kondo effect reside at the millelectronvolt scale. Rigorously, there is a canonical transformation, the Schrieffer-Wolff transformation, which scales away all charge fluctuations generating the effective Hamiltonian, H_{Kondo}, with residual antiferromagnetic interactions between the local moment and conduction electrons [3, 4]. The path to the reduced scale proceeds as the energy excitation bandwidth, D, is successively reduced with the strength of the interaction terms $\{g_j\}$ in the Hamiltonian evolving correspondingly. In general a scaling equation makes the connection

$$\frac{\partial g_j}{\partial \ln D} = \beta_j(\{g_i\}) \tag{2.6}$$

where β is the scaling function. For $\beta < 0$, the interaction terms grow as the bandwidth is reduced while they diminish for $\beta > 0$. The flow of $\{g_i\}$ with D can result in one of two scenarios: a crossover or a fixed point. When the scale D shrinks to a value smaller than the characteristic energy scale of a particular class of high energy excitations, then these excitations are only expressed at small scales through virtual processes. This once again is a statement of how the Kondo model crosses over from the Anderson model as valence fluctuations begin to fall outside the range of the diminishing conduction electron bandwidth. With further reductions in D, the bandwidth drops below the lowest energy

scale and no further changes can be induced in the Hamiltonian thus leaving the interaction terms invariant under scaling. This is equivalent to $\beta \to 0$ and is the limit describing the low energy physics.

Anderson and Yuval [6], through a weak coupling perturbative scaling analysis, showed that below a certain energy scale T_K called the *Kondo temperature*, the Kondo coupling J scales to a value of order $O(1)$ at which point weak coupling is no longer valid. It was not until Kenneth Wilson's seminal work at Cornell on the renormalization group approach and its application to the Kondo problem that this crossover to strong coupling could be treated in a controlled way [7]. Wilson demonstrated definitively that the limit, where J is larger than D, is actually an attractive fixed point of the renormalization flow and consequently that the antiferromagnetic exchange would lead to a screening of the local moment, forming a *Kondo singlet*. Additionally, from the linear temperature dependence of the calculated specific heat, $C_V = \gamma T$, the Fermi liquid character of the dilute magnetic alloy was established.

As a visual summary, figure 2.4 depicts the evolution of the f-spectral function, A_f, in the Anderson model as the correlation strength U is increased, eventually leading to the *Kondo resonance* for large U. The formation of such a sharp peak near the chemical potential is directly tied to the strong coupling which screens the local moment with its width set by the strong coupling crossover scale, T_K. At $U = 0$, the spectral weight at $E = 0$ is $A_f(E = 0) = 1/\Gamma$ and for $U \gg \Gamma$ the local formation will produce two peaks at $\pm U/2$. As the spectral weight must be conserved, the two peaks will each contain approximately half of the weight. However, from considerations of adiabatic continuity, the spectral function right at $E = 0$ cannot change [4] and will keep its $U = 0$ value. This

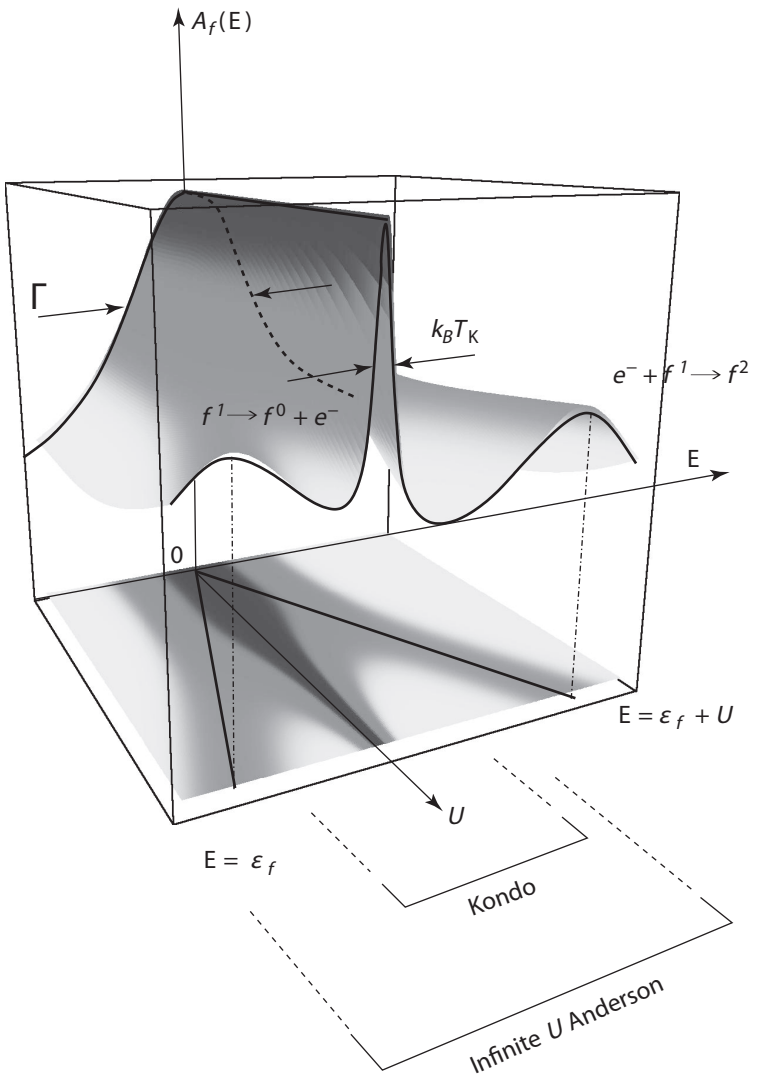

Figure 2.4: Effect of correlation on the f-spectral function in the Anderson model. As the strength U is turned up continuously in the Anderson model, and passes U_c, the broadened bare f-level splits while maintaining a constant occupancy, indicating the formation of local moments. As U is increased so that charge fluctuations are frozen out, the sharp Kondo resonance peak forms. [4]

can only be satisfied if a peak remains at E=0 with a vanishingly small width as U is increased. Physically, the narrow width of the peak is representation of the high frequency virtual hopping processes which couple the conduction electrons to the local moment state.

2.3 The Kondo Lattice

In 1976 Andres, Ott and Graebner discovered the heavy fermion metal $CeAl_3$ [1]. The unique properties of this material included

* A Curie susceptibility $\chi^{-1} \sim T$ at high temperatures.
* A paramagnetic spin susceptibility $\chi \sim$ const at low temperature.
* A linear specific $C_V = \gamma T$, where $\gamma \sim 1600 mJ/mol/K^2$.
* A quadratic temperature dependence of the low temperature resistivity $\rho = \rho_0 + AT^2$

Based on the Fermi liquid expression for the magnetic susceptibility and the linear specific heat,

$$\chi = (\mu_B)^2 \frac{N^*(0)}{1 + F_0^a} \tag{2.7}$$

$$\gamma = \frac{\pi^2 k_B^2}{3} N^*(0) \,, \tag{2.8}$$

where $N^*(0) = \frac{m^*}{m} N(0)$ and F_0^a is the spin-dependent part of the s-wave interaction between quasiparticles, the authors postulated that the low temperature properties of the material were Fermi liquid-like except that the quasiparticle effective masses were approximately 1000 times larger than that of a normal metal. Based on the inferred mass renormalization and knowledge of the large moment formation in rare-earth semi-metals, Doniach [2] proposed that such systems should be modelled by the *Kondo Lattice* Hamiltonian with $S = 1/2$ local moments

$$H_{KL} = \sum_{\mathbf{k},\sigma} \epsilon_{\mathbf{k}\sigma} c^\dagger_{\mathbf{k}\sigma} c_{\mathbf{k}\sigma} + J \sum_i \vec{S}_i \cdot c^\dagger_{\mathbf{k}\alpha} \left(\frac{\vec{\sigma}}{2} \right)_{\alpha\beta} c_{\mathbf{k}'\beta} e^{i(\mathbf{k}'-\mathbf{k})\cdot\mathbf{R}_i} \,. \tag{2.9}$$

Doniach argued that there are two scales in the Kondo lattice, the Kondo temperature T_K and T_{RKKY}, set by the conduction electron density of states ρ and the antiferromagnetic exchange coupling J,

$$T_K = De^{-1/2J\rho} \tag{2.10}$$

$$T_{RKKY} = J^2\rho \ . \tag{2.11}$$

When $J\rho$ is small, then $T_{RKKY} \gg T_K$, and an antiferromagnetic state is formed. Alternatively, when the Kondo temperature is larger than the RKKY interaction scale, Doniach postulated that a dense Kondo lattice ground-state is formed in which each site resonantly scatters electrons. Blochs theorem then ensures that the resonant elastic scattering at each site will form a band, of width $\sim T_K$. The coherence effect in the lattice scenario, which causes a precipitous drop in resistance in heavy fermion systems (see figure 2.2), distinguishes it from the impurity case where resonant scattering leads to an upturn in resistivity at low temperatures. A simple illustration of the Kondo lattice with its array for many-body resonances is given in figure 2.5.

The Kondo lattice as proposed by Doniach is a limiting case of the Periodic Anderson Model, the lattice generalization of the impurity Anderson model [8]:

$$\begin{aligned} H_{PAM} &= H_f + H_d + H_{fd} \\ H_f &= \sum_{i,\sigma} \epsilon^f f^\dagger_{i,\sigma} f_{i,\sigma} + \sum_i \frac{U_{ff}}{2} f^\dagger_{i,\uparrow} f_{i,\uparrow} f^\dagger_{i,\downarrow} f_{i,\downarrow} \\ H_d &= \sum_{\mathbf{k},\sigma} E_{\mathbf{k}} d^\dagger_{\mathbf{k},\sigma} d_{\mathbf{k},\sigma} \\ H_{fd} &= N_S^{1/2} \sum_{i,\mathbf{k},\sigma} \left[V_{\mathbf{k}} \mathrm{e}^{-i\mathbf{k}\cdot\mathbf{R}_i} f^\dagger_{i,\sigma} d_{\mathbf{k},\sigma} + \mathrm{h.c} \right] \end{aligned} \tag{2.12}$$

H_f represents the Hamiltonian describing the lattice of localized f electrons, H_d describes the conduction states and H_{fd} the hybridization between the two. In

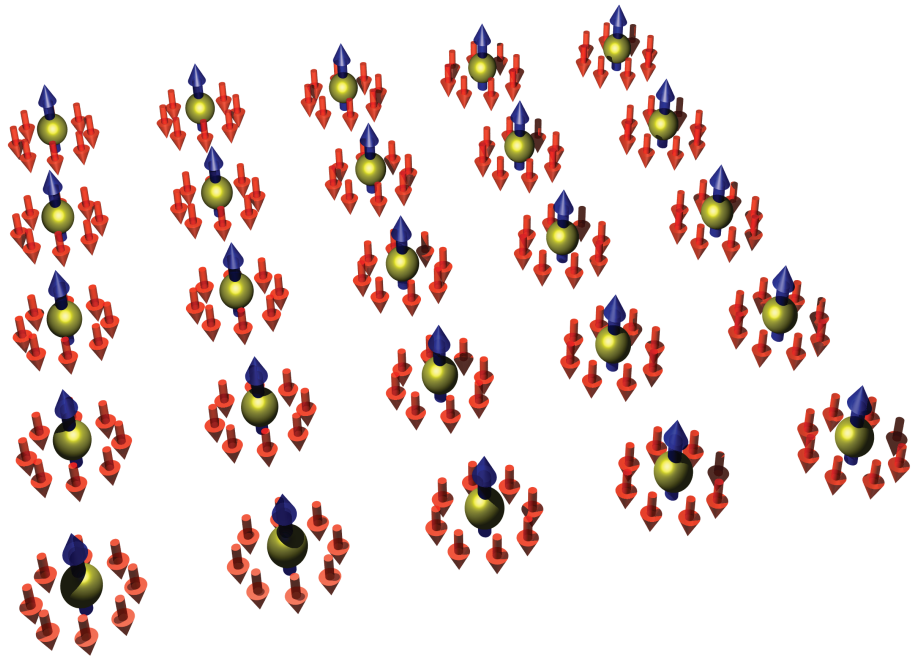

Figure 2.5: Illustration of a Kondo lattice. The local moments, drawn with blue arrows, form a lattice of localized spins which at low temperatures become screened by conduction electrons (red arrows) through the Kondo effect, forming a matrix many-body singlet states.

the simplest version of the Anderson model, the ion is taken to have $s = 1/2$, but more realistically atoms produce much larger moments. For example, an electron in a rare-earth Cerium Ce^{3+} ion atom lives in a $4f^1$ state. The spin-orbit coupling combines orbital and spin angular momentum into a total angular moment $j = l - 1/2 = 5/2$. Thus, the Cerium ion that forms has a moment of $j = 5/2$ and a spin degeneracy of $2j + 1 = 6$. Now, the degeneracy can be further reduced by considering crystal field splitting and typically calculations in rare-earth compounds only consider a degeneracy of 2. Further complexity arises when additional electrons live in the f levels and Hunds coupling must be factored in. Actinide heavy fermion materials are exactly of this last type making for an intricate spin manifold to consider in the Kondo screening scenario.

2.3.1 Renormalized Bands

To demonstrate the nature of the lattice problem consider the periodic Anderson model in equation 2.12 and the effective Hartree approximation which allows for the construction of the one-electron Green's function for the conduction electrons and the f electrons as a function of ω and $\mathbf{k}$

$$\begin{bmatrix} \omega - \mu - \epsilon^f_{\mathbf{k}} - \Sigma_\sigma(\omega, \mathbf{k}) & -V_{\mathbf{k}} \\ -V_{\mathbf{k}} & \omega - \epsilon_{\mathbf{k}} \end{bmatrix} \begin{bmatrix} G^{ff}_{\mathbf{k}\sigma} & G^{cf}_{\mathbf{k}\sigma} \\ G^{fc}_{\mathbf{k}\sigma} & G^{cc}_{\mathbf{k}\sigma} \end{bmatrix} = I \tag{2.13}$$

where μ is the chemical potential and $\Sigma_\sigma(\omega, \mathbf{k})$ is the proper self-energy derived from the two-body interaction between the f electrons [3]. For the non-interacting case, $U_{ff} = 0$, the self-energy is zero from which the quasiparticle states are easily determined by looking at the poles of G^{ff} and G^{cc}

$$G^{ff}_{\mathbf{k}\sigma} = \frac{1}{\omega - \mu - \epsilon^f_{\mathbf{k}} - |V_{\mathbf{k}}|^2/(\omega - E_{\mathbf{k}})} \tag{2.14}$$

$$G^{cc}_{\mathbf{k}\sigma} = \frac{1}{\omega - E_{\mathbf{k}} - |V_{\mathbf{k}}|^2/(\omega - \mu - \epsilon^f_{\mathbf{k}})} \,. \tag{2.15}$$

where $E_{\mathbf{k}}$ is the conduction electron dispersion. The two bands that emerge are of mixed f and d character given by

$$E^{\pm}_{\mathbf{k}} = \frac{\epsilon^f_{\mathbf{k}} + E_{\mathbf{k}} \pm \sqrt{\left(\epsilon^f_{\mathbf{k}} - E_{\mathbf{k}}\right)^2 + 4\,|V_{\mathbf{k}}|^2}}{2} \,. \tag{2.16}$$

This electronic structure has no associated Kondo effect since such an effect would require local moment formation which is contingent upon a large on-site repulsion U_{ff}. The effect of correlations can be introduced in by assuming that the self-energy has a Taylor expansion about a point on the Fermi surface, $\omega = \mu,\ \mathbf{k} = \mathbf{k}_F$

$$\begin{aligned} \Sigma(\omega, \mathbf{k}) &= \Sigma^R(\mu, \mathbf{k}_F) \\ &\quad + (\mathbf{k} - \mathbf{k}_F) \cdot \nabla \Sigma^R(\mu, \mathbf{k})_{\mathbf{k}=\mathbf{k}_F} + (\omega - \mu) \left(\frac{\partial \Sigma^R(\omega, \mathbf{k}_F)}{\partial \omega} \right)_{\omega=\mu} + \ldots \end{aligned} \tag{2.17}$$

with $\Sigma = \Sigma^R + i\Sigma^I$. In this region $\Sigma^I(\omega, \mathbf{k}_F) \sim (\omega - \mu)^2$ [3] and hence is not explicitly stated in the expansion above. Truncating the series to first order, a revised set of quasiparticle Green's functions can be defined

$$\tilde{G}^{ff}_{\mathbf{k}\sigma}(\omega) = \frac{1}{\omega - \mu - \tilde{\epsilon}^f_{\mathbf{k}} - |\tilde{V}_{\mathbf{k}}|^2/(\omega - E_{\mathbf{k}})} \tag{2.18}$$

$$\tilde{G}^{cc}_{\mathbf{k}\sigma} = \frac{1}{\omega - E_{\mathbf{k}} - |\tilde{V}_{\mathbf{k}}|^2/(\omega - \mu - \tilde{\epsilon}^f_{\mathbf{k}})} \tag{2.19}$$

where

$$\tilde{\epsilon}^f_{\mathbf{k}} = z_{\mathbf{k}_F}(\epsilon^f + \Sigma(\mu, \mathbf{k}_F) + (\mathbf{k} - \mathbf{k}_F) \cdot \nabla\Sigma^R(\mu, \mathbf{k}_F)) \tag{2.20}$$

and

$$|\tilde{V}_{\mathbf{k}}|^2 = z_{\mathbf{k}_F}|V_{\mathbf{k}}|^2 \quad , \quad z_{\mathbf{k}_F} = \left(1 - \left(\frac{\partial\Sigma^R(\omega, \mathbf{k}_F)}{\partial\omega}\right)_{\omega=\mu}\right)^{-1} . \tag{2.21}$$

The poles of 2.18 and 2.19 satisfy the quadratic

$$(\omega - \mu - \tilde{\epsilon}^f_{\mathbf{k}})(\omega - E_{\mathbf{k}}) - |\tilde{V}_{\mathbf{k}}|^2 = 0 \tag{2.22}$$

and hence give rise to two bands

$$E^{\pm}_{\mathbf{k}} = \frac{\widetilde{\epsilon}^f_{\mathbf{k}} - \mu + E_{\mathbf{k}} \pm \sqrt{\left(\widetilde{\epsilon}^f_{\mathbf{k}} - \mu - E_{\mathbf{k}}\right)^2 + 4\left|\widetilde{V}_{\mathbf{k}}\right|^2}}{2} . \tag{2.23}$$

The new quasiparticle bands have the same form as those for the $U_{ff} = 0$ case except that the f-character energy band as well as the hybridization matrix elements have been renormalized. In the limit $U_{ff} \to \infty$, the f states at each site cannot be more than singly occupied, $0 < n_f \leq 1$, and thus the effective f band must lie right at or just above the chemical potential. The dispersion described in the strong correlation limit is the *Heavy Fermion* band structure and is depicted in figure 2.6.

There are a number of features requiring further elucidation. First, because there is a one-to-one correspondence between the non-interacting band structure and the interacting one, adiabaticity and Luttinger's theorem tells us that

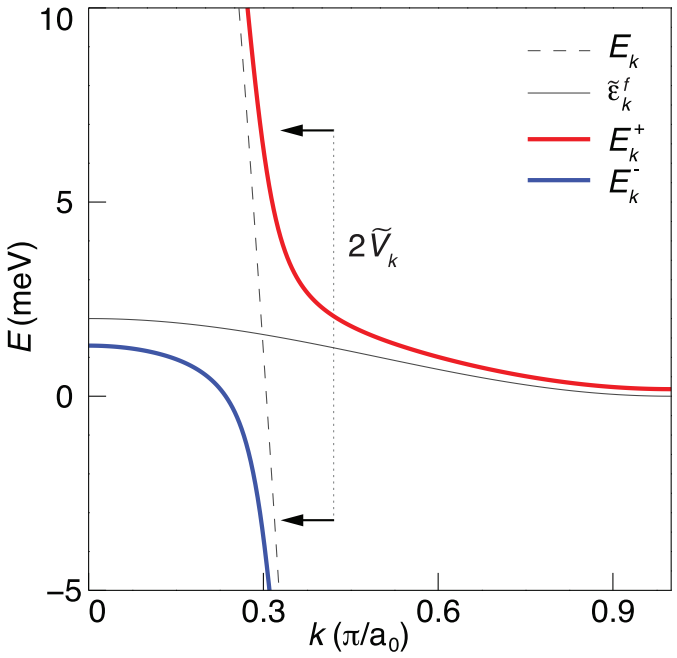

Figure 2.6: Heavy fermion band structure. The electronic structure in equation 2.23 as derived from the periodic Anderson model in the $U_{ff} \to \infty$ limit. The approximate hybridization energy range is shown by horizontal arrows.

the total number of band electrons $n_{tot} = 2/(2\pi)^3 \times$ Volume of the Fermi surface. Thus, if the ground state is metallic, the chemical potential must lie in the lower band thus defining a Fermi surface which has expanded in volume to accommodate the additional f electrons which melted into the Fermi sea. As illustrated in figure 2.6, the expansion of the Fermi surface derives from a flattening of the quasiparticle dispersion near the chemical potential as the light conduction band hybridizes with the effective f-band at low temperatures. Consequently, the effective mass grows substantially and heavy quasiparticles are born. Second, the splitting of the electronic structure into an effective upper and lower Fermi band defines a direct gap of size $2\tilde{V}_{\mathbf{k}}$ (see figure 2.6). There is also an indirect *hybridization gap*, $\Delta_g \sim |\tilde{V}_{\mathbf{k}}|^2$ [4] which is only properly defined when the upper and lower band are truly separated and not as depicted in figure 2.6, where the weak effective f-band dispersion allows for crossover. If one were

to measure the density of states, this could mean the difference between a true gap, flanked by two sharp peaks derived from the flat bands, and possibly a pseudogap in which such features are convolutedly expressed.

2.4 Applicability of Kondo Physics to the Heavy Fermions

2.4.1 Ce-based Materials

The role of Kondo physics in the Ce-based heavy-fermion compounds is supported by the fact that both the thermodynamic properties at low temperatures as well as the temperature-dependence of the spectroscopic data can be reproduced by an Anderson model. The most direct evidence, has come from photoelectron spectroscopy. The characteristic features of a Kondo system can be summarized as follows [9]: At high temperatures, the combined photoelectron spectrscopy/bremsstrahlung-isochromat (PES/BIS) spectra from photoemission and inverse photoemission exhibit two distinct peaks below and above the Fermi energy. These two features correspond to the valence transitions $f^n \rightarrow f^{n\pm1}$, respectively whose energy scales are on the order order electron-volts. The low-energy scale is marked by the appearance of a sharp peak in the f-spectral density near the Fermi energy when the temperature is lowered past some characteristic scale T^*. Figure 2.7b shows the temperature dependent results in one such high resolution photoemission experiment for the heavy fermion compound $CeCu_2Si_2$ [10] and supports the idea that a Kondo resonance forms in the lattice at low temperatures. However, the calculations which support the data derive from the impurity Anderson model, providing the interpre-

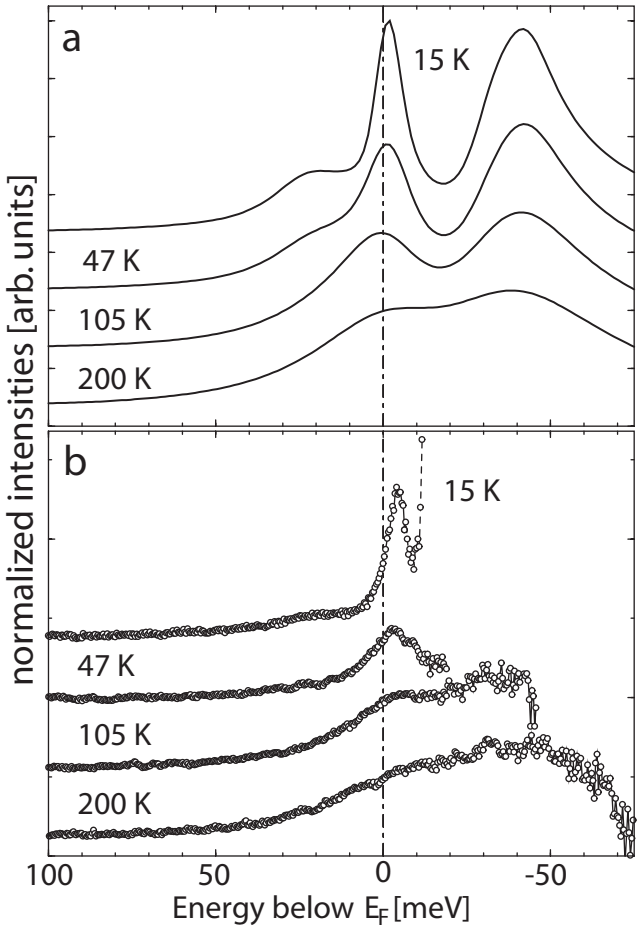

Figure 2.7: Temperature evolution of Kondo feature in PES. **a**, Theoretical T dependence of the $4f$ spectral function of $CeCu_2Si_2$ as derived from the impurity Anderson model. **b**, Photoemission spectra for T = 15, 47, 105, and 200 K, normalized to the same intensity at 100 meV. [10]

tation that $CeCu_2Si_2$ is a lattice of localized, non-dispersive Kondo many-body states [11, 10, 12]. This is in stark contrast to the physics of heavy fermions, as presented above, which describes a set of itinerant quasiparticles emerging from the Kondo many-body states. On the other hand, there are photoemission studies [13, 14, 15, 16] which require invoking the periodic Anderson model to explain band dispersions, intensities and temperature dependent behavior.

2.4.2 U-based Materials

The applicability of the Anderson model in the Kondo limit for U-based compounds is tenuous. First, the $5f$ wavefunctions of uranium are less localized than the $4f$ ones of cerium, potentially allowing for greater inter-site coupling and a lower value of U_{ff}. Second, the nominal configuration of U atoms in heavy fermion materials is believed to be $5f^2$ or $5f^3$ instead of $4f^1$ as in Ce-based materials [17, 3, 15, 18]. This leads to a much larger set of ground and excited state configurations boasting a complex angular momentum manifold which would have to be considered in deriving an effective model. Finally and perhaps most importantly, U-based compounds exhibit more mixed valence behavior which weakens local moment formation. The spectroscopic fingerprint of $f^n \rightarrow f^{n+\pm 1}$ transitions, seen in Ce compounds as two sharp f-derived peaks is replaced by one very broad peak indicating a mixed valence regime [3, 18]. Some early mean field theory calculation treated U-based heavy fermions in the context of the Anderson model [19, 20] by accounting for both the mixed valency as well as the f^2 and f^3 configurations. The results preserve the form of the quasiparticle bands in equation 2.23, however, with a substantially reduced energy scale describing the renormalized heavy fermion bandwidth.

Dual Model of $5f$ Electrons

Because of the varying degree of localization of the $5f$ electrons in certain U-compounds, a dual model was proposed [21] to account for some properties which reflect an itinerant character and others reflective of a localized one. In such a framework for heavy fermion materials, primarily based on the observations UPt_3 [22] and $UPdAl_3$ [23], two of the three $5f$ electrons are localized in

orbitals of specific symmetry and are CEF split of the order of a few meV. The mechanism for heavy quasiparticle formation then derives via the scattering of delocalized $5f$-electrons by the internal crystal-electric-field (CEF) excitations of their localized counterparts. In fact, the model has also been applied to Ce-based compounds such as $CeCoIn_5$ and $CeIrIn_5$ [24] with promising results.

Quadrupolar Kondo Effect

In certain U-based heavy fermion compounds, like UBe_{13}, the weak magnetic field response in such quantities as the electronic specific heat at low temperature, as compared to Ce-based compounds like $CeCu_2Si_2$ is a puzzling observation. [25]. Both sets of materials are believed to exhibit Kondo physics and yet the former group lacks the supposed natural response to magnetic fields. This lead Cox [17] to propose the quadrupolar Kondo effect as an alternative Kondo-like mechanism for heavy fermion formation in actinide-based compounds. For a U ion with a nominally $5f^2$ configuration placed at a site of cubic symmetry, it is possible to have a low lying *non*-magnetic quadrupolar doublet which is quenched.

The model considers a set of model U-sites in cubic symmetry sites with the following properties:

* stable $5f^2$, $j = 4$ Hund's rule ground state
* CEF split $j = 4$ multiplet with non-magnetic doublet ground state, Γ_3.
* $5f^1$ levels lie above the Γ_3 states, the closest being the magnetic doublet state Γ_7, ϵ_f away.

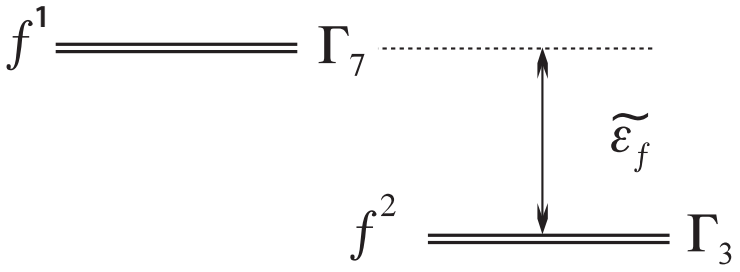

Figure 2.8: Simplified level scheme for U^{4+} ions in cubic symmetry undergoing quadrupolar Kondo effect. This simple model involves a doublet in each of the two lowest lying configurations, with the f^2 having the non-magnetic quadrupolar Γ_3 doublet, and the f^1 configuration having the magnetic Γ_7 doublet. Conduction electrons mix the two configurations through hybridization processes. From symmetry selection rules, only a Γ_8 conduction state can couple the two doublet states [26].

* the Γ_3 and Γ_7 states hybridize with conduction states of the appropriate symmetries

Other states are discarded by taking all other crystal field, spin orbit and exchange splittings to infinity, effectively leaving only the magnetic to non-magnetic doublet $f^1 \leftrightarrow f^2$ transition as illustrated in figure 2.8. The transition $f^1 \leftrightarrow f^2$ generated by emitting or removing a conduction electron, restricts the symmetry of the conduction states which may hybridize with the uranium $5f$ states. From group theoretical considerations only the Γ_8 conduction quartet partial waves may couple to the U ion through hybridization. These are derived from conduction partial waves with orbital angular momentum $l = 3$ spin-orbit coupled to produce $j = 5/2, 7/2$ manifolds, with each angular momentum manifold giving a Γ_8 partial wave quartet [17, 26]. The relevant states, which only considers the $j = 5/2, \Gamma_8$ quartet, are presented in table 2.1. The effective Anderson Hamiltonian in this restricted Hilbert space is termed the '3-7-8' model and by the equivalent canonical transformation as that used in the classic Kondo problem, can be mapped onto an effective multichannel Kondo model with an

Config.	State	Parent j	Form	$\langle j_z \rangle$	$\langle 3j_z^2 - j(j+1) \rangle$
f^2	$\Gamma_3(+)$	4	$\sqrt{\frac{5}{24}}\|4\rangle + \|-4\rangle + \sqrt{\frac{7}{12}}\|0\rangle$	0	+8
f^2	$\Gamma_3(-)$	4	$\sqrt{\frac{1}{2}}\,[\|2\rangle + \|-2\rangle]$	0	-8
f^1	$\Gamma_7(\uparrow)$	5/2	$\sqrt{\frac{1}{6}}\|-5/2\rangle - \sqrt{\frac{5}{6}}\|3/2\rangle$	$+\frac{5}{6}$	0
f^1	$\Gamma_7(\downarrow)$	5/2	$\sqrt{\frac{1}{6}}\|5/2\rangle - \sqrt{\frac{5}{6}}\|-3/2\rangle$	$-\frac{5}{6}$	0
c^1	$\Gamma_8(2)$	5/2	$\sqrt{\frac{5}{6}}\|5/2\rangle + \sqrt{\frac{1}{6}}\|-3/2\rangle$	$+\frac{11}{6}$	+8
c^1	$\Gamma_8(\bar{2})$	5/2	$\sqrt{\frac{5}{6}}\|-5/2\rangle + \sqrt{\frac{1}{6}}\|3/2\rangle$	$-\frac{11}{6}$	+8
c^1	$\Gamma_8(1)$	5/2	$\|1/2\rangle$	$+\frac{1}{2}$	-8
c^1	$\Gamma_8(\bar{1})$	5/2	$\|-1/2\rangle$	$-\frac{1}{2}$	-8

Table 2.1: Angular momentum character of states for Kondo models for U^{4+} in cubic symmetry. The second column is standard notation describing the symmetry of the given states. The fourth column gives information about the states of definite azimuthal quantum number values which are mixed to form the state in cubic symmetry. The last two columns give information about the expectation values of magnetic and quadrupolar moments. [26, 27].

antiferromagnetic exchange interaction [17]:

$$H_{ex} = -2J_{ex}\sigma_3 \cdot (\sigma_8 + \sigma_{\bar{8}}) \,. \tag{2.24}$$

To make the connection even stronger to the Kondo scenario, the double degeneracy of the ground level allows one to treat it as a two-level system, which can be further regarded as a manifold with a pseudo-spin of 1/2.

The presence of crystal field states is an essential element of the quadrupolar Kondo effect and yet it is a controversial point in the actinide intermetallics, for which the model was originally intended. Sharp crystal field excitations have only been observed in UPd_3 [28], UPd_2Al_3 [29], and URu_2Si_2 [30], whereas their presence in rare-earth intermetallcs is far more numerous [26]. However, it is exactly for this reason that the quadrupolar Kondo effect and its modern derivatives have attracted attention in solving one of the most baffling and singular transitions in the heavy fermion family: the 'hidden' order in URu_2Si_2, the

subject at the core of this thesis.

2.4.3 Further Inconsistencies

One of the key predictions of the Anderson/Kondo lattice model is a scaling relationship between the magnitude of the direct energy gap in the excitation spectrum and the enhancement of the quasiparticle effective mass [3, 4]. However, not all heavy fermions follow this pattern. Infrared experiments have revealed that the scaling relationship is followed by most heavy fermion systems with nonmagnetic ground states whereas those which order magnetically show distinct deviations [31].

2.5 Outlook

The underlying theoretical framework for heavy fermions rests primarily on the Anderson model, and more specifically on its representation in the Kondo limit. And while the elegance captures the underlying physics of a large number of heavy fermion materials, there naturally remain unreconciled elements between theory and experiment. This is related to a particularly worrisome classification of materials as *heavy fermion* based on one class of observables, such as specific heat or magnetic susceptibility, consistent with theory but not other classes, such as the presence of the microscopic signature of the hybridization gap, with $CeAl_3$ and URu_2Si_2 as prime examples of materials lacking the latter. More directly posed, is a compound a heavy fermion based on phenomenological macroscopic metrics associated with effective mass or on microscopic sig-

natures predicted by theory, or both? The confusion arises when the criteria are mixed and an overarching effective model is sought to capture the conflicting observations.

The content of the following chapters will bring to the foreground facets of basic heavy fermion physics which have yet been untested and in some cases unexpected. The context, the mysterious 'hidden' order phase of URu_2Si_2, further serves to highlight the great scope of correlated electron physics yet to be understood in the heavy fermion field and the need for new and powerful experimental and theoretical tools to make progress in a subject that is already over 30 years old.

REFERENCES FOR CHAPTER 2

[1] Andres, K., Graebner, J., and Ott, H. R. *Physical Review Letters* **35**, 1779–1782 (1975).

[2] Doniach, S. *Physica B* **91**, 231–234 (1977).

[3] Hewson, A. C. *The Kondo Problem to Heavy Fermion*. Cambridge University Press, (1993).

[4] Coleman, P. *Heavy Fermions: electrons at the edge of magnetism*, 95–148. John Wiley (2007).

[5] Phillips, P. *Advanced Solid State Physics*. Westview Press, (2003).

[6] Anderson, P. W. and Yuval, G. *Physical Review Letters* **23**, 89–92 July (1969).

[7] Wilson, K. *Reviews of Modern Physics* **47**, 773–840 October (1975).

[8] Coleman, P. *Physical Review B* **35**, 5072–5116 April (1987).

[9] Malterre, D., Grioni, M., and Baer, Y. *Advances in Physics* **45**, 299–348 (1996).

[10] Reinert, F., Ehm, D., Schmidt, S., Nicolay, G., Hüfner, S., Kroha, J., Trovarelli, O., and Geibel, C. *Physical Review Letters* **87**, 3–6 August (2001).

[11] Garnier, M., Breuer, K., Purdie, D., Hengsberger, M., Baer, Y., and Delley, B. *Physical Review Letters* **78**, 4127–4130 May (1997).

[12] Jung, R.-J., Choi, B.-H., Oh, S.-J., Kim, H.-D., Cho, E.-J., Iwasaki, T., Sekiyama, A., Imada, S., Suga, S., and Park, J.-G. *Physical Review Letters* **91**, 157601 October (2003).

[13] Arko, A., Joyce, J., Andrews, A., Thompson, J., Smith, J., Mandrus, D., Hundley, M., Cornelius, A., Moshopoulou, E., Fisk, Z., Canfield, P., and Menovsky, A. *Physical Review B* **56**, R7041–R7044 September (1997).

[14] Tahvildar-Zadeh, A., Jarrell, M., and Freericks, J. *Physical Review Letters* **80**(23), 5168–5171 June (1998).

[15] Denlinger, J. *Journal of Electron Spectroscopy and Related Phenomena* **117-118**, 347–369 June (2001).

[16] Im, H., Ito, T., Kim, H.-D., Kimura, S., Lee, K., Hong, J., Kwon, Y., Yasui, A., and Yamagami, H. *Physical Review Letters* **100**, 176402 April (2008).

[17] Cox, D. *Physical Review Letters* **59**, 1240–1243 (1987).

[18] Thalmeier, P. and Zwicknagl, G. *Unconventional superconductivity and magnetism in lanthanide and actinide intermetallic compounds*, volume 34, 135–287. Elsevier (2004).

[19] Rasul, J. and Harrington, A. *Journal of Physics C: Solid State Physics* **20**, 4783–4800 (1987).

[20] Evans, S. and Gehring, G. *Journal of Physics: Condensed Matter* **1**, 10487–10505 (1989).

[21] Schoenes, J., Vogt, O., Löhle, J., Hulliger, F., and Mattenberger, K. *Physical Review B* **53**, 14987–14995 June (1996).

[22] Zwicknagl, G., Yaresko, A., and Fulde, P. *Physical Review B* **65**, 081103 February (2002).

[23] Zwicknagl, G., Yaresko, A., and Fulde, P. *Physical Review B* **68**, 052508 August (2003).

[24] Nakatsuji, S., Pines, D., and Fisk, Z. *Physical Review Letters* **92**, 016401 January (2004).

[25] Stewart, G. *Reviews of Modern Physics* **56**, 755–787 October (1984).

[26] Cox, D. and Zawadowski, A. *Advances in Physics* **47**, 599–942 (1998).

[27] Tinkham, M. *Group theory and quantum mechanics*. Dover Publications, New York, (2003).

[28] Buyers, W., Murray, A., Holden, T., Svensson, E., Devduplessis, P., Lander, G., and Vogt, O. *Physica B+C* **102**, 291–298 October (1980).

[29] Krimmel, A., Loidl, A., Eccleston, R., Geibel, C., and Steglich, F. *Journal of Physics: Condensed Matter* **8**, 1677–1685 (1996).

[30] Broholm, C., Lin, H., Matthews, P., and Mason, T. *Physical Review B* **43**, 12809–12822 (1991).

[31] Dordevic, S., Basov, D., Dilley, N., Bauer, E., and Maple, M. *Physical Review Letters* **86**(4), 684–687 January (2001).

CHAPTER 3

THE HEAVY AND THE 'HIDDEN' - URu_2Si_2

3.1 Introduction

URu_2Si_2 is a modest heavy fermion compound (γ = 110mJ/mol K^2 [1]) whose claim to fame rests in one of the most perplexing phase transitions in the field, that leading to the 'hidden' order (HO). From the time of its discovery over 25 years ago as a heavy fermion superconductor [2], the yet unexplained ordering at $T_0 = 17.5K$, has resisted the barrage of experimental and theoretical efforts to unveil its source. The label 'hidden' is misleading as the second order transition is clearly detectable by a wide range of probes including specific heat, magnetic susceptibility, Hall-resistivity, neutron scattering, muon spin resonance, photoemission and STM, and only ignorance of the underlying ordering furnishes the brand. The range of proposals to describe the HO include conventional and exotic density waves as well as multipolar order each with distinct starting points regarding the degree of localization of the f-electrons and the nature of their interactions with the lattice. As a U-based heavy fermion compound, most likely in a mixed-valent regime, even the 'normal' state above the 'hidden' order is not well understood and its associations with Kondo lattice theory remains tenuous. In this sense, the problem of determining the nature of the 'hidden' order as one emerging from a parent state is ill-posed.

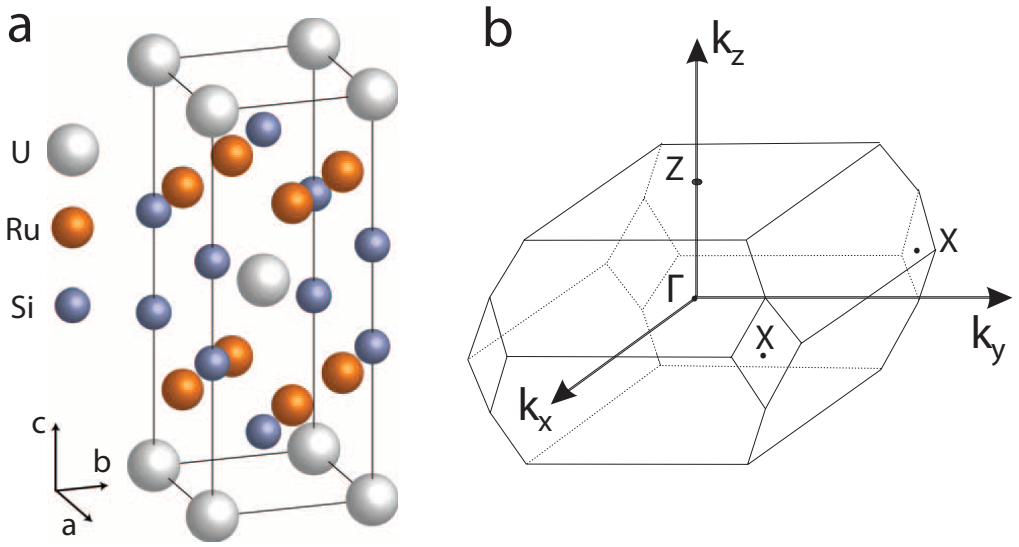

Figure 3.1: Crystal and reciprocal lattice structure of URu_2Si_2. **a**, Unit cell of URu_2Si_2 showing a body-centered tetragonal (bct) configuration. Both Si and U layers have equal in-plane sub-lattice spacings of a_0 = 4.12 Å while the Ru atoms are spaced at $a_0/\sqrt{2}$. **b**, Brillouin zone of bct configuration with high symmetry points identified. [4]

3.2 Basic Electronic Structure

Figure 3.1 shows both the basic unit cell of URu_2Si_2 and its Brillouin zone in the paramagnetic state above the 'hidden' order transition. The crystal structure is body-centered tetragonal (bct) with each layer in the lattice mono-elemental. Both the Si and U layers share a common sub-lattice periodicity of a_0 = 4.12 Å while the Ru atoms have a spacing of $a_0/\sqrt{2}$ = 2.19 Å [3]. The Brillouin zone of the bct structure and its high symmetry points are shown in figure 3.1b. The region around the Γ point marks the region in momentum space from which the measurement presented in chapter 5 are believed to originate.

In the paramagnetic state, the basic electronic structure of URu_2Si_2 has been probed in detail by photoemission and compared with LDA calculations [5, 4]. The main body of the valence-band structure is comprised of the Ru 4*d* and

the Si $3p$ states spread over several slowly dispersive bands extending out to a few electronvolts. At lower energies, there are strong disagreements between photoemission and LDA, in particular regarding the strength of hybridization between the Ru $4d$ and U $5f$ states. Nonetheless, there is some evidence that the top most Ru $4d$ band is flattened near E_F brought upon by hybridizing with the U $5f$ states. Inelastic neutron scattering [6], using the time-of-flight method suggests that the valence state in URu_2Si_2 is U^{4+} corresponding to a $5f^2$ configuration. Accounting for the intermultiplet transition energies and comparing to free ion parameters for U, the lowest lying multiplet was identified as $j = 7/2$ state, nominally having a ninefold degeneracy. In tetragonal symmetry the degenerate multiplet should be split by the CEF potential into five singlets and two doublets [7]. There is indeed an indication of four strongly broadened CEF transitions at energies ranging from $\delta = 5$ meV to 159 meV. However, the data are not sufficient to determine the CEF potential and states. There is one particular transition at 49 meV which might be associated with the $\Gamma_3 \rightarrow \Gamma_5$ transition from the non magnetic Γ_3 ground state. The evidence for CEF states supports a view of mostly localized $5f$ states in URu_2Si_2 in the normal phase since f-bandwidth is very narrow. However, this raises the question of the origin of heavy fermion behavior in this compound for in a nonmagnetic $5f$ singlet ground state system there is no standard Kondo mechanism to generate heavy quasiparticles [7]. Consequently, the low-lying multiplet structure has led to proposals that the normal state of URu_2Si_2 can be explained by CEF states [8, 9].

3.3 The 'Hidden' Order

The two decades of intense research devoted to uncovering the elusive 'hidden' order of URu_2Si_2 was instigated by the discovery of the compound's coexistent magnetic order below the same transition temperature [2]. Initially, not drawing a distinction between the two facets of the ordering, early thermodynamic [1] and optical conductivity [10] measurements attributed it to spin and charge density wave transitions with proposed gapping of the Fermi surface, a notion also supported by Hall-effect studies [11]. Neutron scattering experiments further supported the idea of magnetic ordering by revealing an antiferromagnetic structure connected with a partial removal of the electronic density of states below T_0 [12, 13]. With a very small moment of $0.03\mu_B$, however, the weak antiferromagnetism failed to account for the large entropy loss, 0.2Rln2 [2], associated with the phase transition. The seemingly evident nature of the phase transition quickly turned enigmatic.

The creative foray of theory to demystify the 'hidden' order in URu_2Si_2 is richly varied but not completely successful in reproducing the basic set of observations. For in as much as there is contention about the ordered state, uncertainty about the unordered regime insufficiently constrains the problem. Even the most fundamental of predictions that heavy quasiparticles bands are born out of the hybridization of light conduction and renormalized f states is not universally applicable (see Chapter 2). One theory has propounded that the 'hidden' order transition arises from the quadrapolar ordering of localized f-states and that the observed gap in the ordered state could be attributed to the CEF singlet-singlet excitation energy [8, 14]. Alternatively, temperature independence of the nonlinear susceptibility in the unordered phase seems to rule

out a solely local-moment picture. An itinerant quadrapolar order parameter, on the other hand, would account for both the jump in the nonlinear susceptibility at the phase transition as well as its temperature dependence above [15].

Such exotic spin ordering of URu_2Si_2 was originally inspired by generalizations of the work on weak ferromagnetism. Multispin correlators emphasized the importance of exchange interactions yielding observables that could be probed by neutron scattering if one were to properly account for them in the magnetic generalizations of the Born approximation [16]. A more classic route to spin ordering derives from the theoretical result that heavy fermion ground states are renormalized Fermi liquids making them susceptible to the standard Landau-Pomeranchuk instabilities. Helicity order [17], for instance, is one such realization in which the Fermi surface distorts along the symmetry direction of the $l = 1$ angular momentum channel of the Fermi liquid representation. And while many theories of 'hidden' order in URu_2Si_2 attempt to directly integrate coexistant spin ordering, there is also the possibility of orbital ordering [18].

Recent studies point strongly to a significant restructuring of the Fermi surface in the ordered state. Point contact measurements support a scenario in which the Fermi surface is partially gapped [19, 20]. More definitively, inelastic neutron spectroscopy (INS) measurements claim to account for the missing entropy in the transition to the 'hidden' ordered state by the gapping of itinerant spin excitations [21]. Since the modes were attributed to itinerant heavy quasiparticle excitations, it points strongly to a gapping of the Fermi surface. The presence of gapped spin excitations has also prompted phenomenology whereby spectral weight changes brought upon by an assumed electronic state gap lead to a peak in the spin susceptibility [22]. Such a peak would then be

detectable as an incommensurate spin resonance in INS experiments, providing a test of the underlying conjectures.

The latest evidence for Fermi surface reconstruction has come from ARPES revealing that for the filled states above T_0, a light band crosses E_F near $(0, \pm 0.3)\pi/a_0$; $(\pm 0.3, 0)\pi/a_0$ close to a band of incoherent f spectral weight which upon descending into the 'hidden' order state evolves into a heavy band sitting just below the chemical potential [23, 24]. Impressively, the inferred effective mass, $m^* \approx 25m_e$ is in accord with thermodynamics [1]. While the full structure of the heavy band is somewhat shrouded, the sharpening of the band in the hidden ordered state suggests that the formation of heavy quasiparticles is directly linked to the phase transition, the first reported observation of its kind. The link has recently been further strengthened by high resolution laser ARPES experiments [24].

As more powerful microscopic measurement techniques such as high resolution ARPES and STM enter the heavy fermion stage, complementary computational tools are developing alongside. In a tour-de-force calculation producing both real and momentum space resolved observables, the latest set of DMFT results gives new insight into *both* phases of URu_2Si_2 across the T_0 transition [9, 25]. At the heavy fermion coherence temperature, well above T_0, the two lowest lying U CEF f-states of a $j = 4$ multiplet begin to conspire with multiple light *spd* bands leading to a multichannel Kondo effect and consequently the enhancement of f spectral weight within a thin energy band of the chemical potential. For temperatures above the narrow energy level splitting, $\delta = 35$K, the ground state is degenerate as the two CEF states are effectively smeared into one another. However, upon lowering the temperature through $T = 35$K,

the degeneracy begins to lift and the Fermi surface reorganizes itself, opening a partial gap by sending a large portion of f-spectral weight to just above the chemical potential. What remains generates the modest effective heavy masses of the quasiparticles above the HO transition. In passing to the HO regime, the partial gap above the transition deepens to a full gap in accord with what now is a well established feature of the HO state. The atomic U CEF states involved in the Kondo effect are featured again with their relative mixing at each lattice site providing the basis for the proposed complex order parameter. The real part describes the HO phase while the imaginary part the large antiferromagnetic phase which is induced under pressure. If such a mechanism were responsible for the HO, it would manifest itself as a hexadecapole and possibly be detectable through resonant X-ray techniques.

The proposals to explain the mysterious transition to a 'hidden' order state can be approximately separated into two basic classes. The first considers **k**-space susceptibilities of the Fermi surface to a conventional density wave state [1, 22, 26, 17, 18] while the second considers ordering of the **r**-space states at the U atoms, with the corresponding alteration (via hybridization changes) to the band structure [9, 13, 16, 8, 25, 27]. However, despite two decades of research, which of these classes correctly describes the hidden-order transition in URu_2Si_2 remains unknown. Addressing the problem requires a probe which can simultaneously measure the real space and momentum space structure, making spectroscopic imaging STM a powerful tool in the study of this long standing problem in condensed matter physics.

3.4 Cleavage Planes and Surface States

The pure compound URu_2Si_2 exhibits one excellent cleave surface that is Si-terminated, whereas the alloy $U_{0.99}Th_{0.01}Ru_2Si_2$, which was used for quasiparticle interference studies, exhibits a different excellent cleave surface that is U-terminated. Each of these two cleave surfaces has the same lattice periodicity and orientation, which is highly distinct from that of the Ru layer (inset in Fig. 3.1a). They can be distinguished from each other because the U-termination layer exhibits the correct density of impurity states generated by the 1% of U sites upon which Th atoms are substituted (black spots in Fig. 4.5a).

In conducting surface measurements such as in STM or photoemission, the presence of 2-D states at the termination layer can lead to observations that are not directly representative of the bulk system requiring a more careful interpretation of the data. In Kondo impurity systems observed through SI-STM, the involvement of surface states in forming spectra representative of the many-body state, was clearly demonstrated by the visualization of quantum mirages at sites away from the magnetic moment contributing adatom [28]. In the case of URu_2Si_2, there is firm evidence of a surface state from ARPES [23, 29], which had been mistakenly interpreted as a bulk band in past experiments [5]. The new measurements [29] describe the surface feature as a hole-like band bound below $E = -35$ meV likely arising in the projected gap of a light hole-like Ru-4d band and a lighter band of Si-p character. Bolstering recent ARPES experiments which show clear band structure changes associated with the 'hidden' order transition [23, 24], the surface state was shown to be unrelated to the observed band structure changes coincident with the onset of the 'hidden' order state, a fact of great relevance for SI-STM investigations of the low temperature phase

of URu_2Si_2.

3.5 Misinterpreting the Heavy Fermion Character

In anticipation of the results in the following chapters, the interpretation of the transition into the 'hidden' order phase deserves comment. Most of the work on URu_2Si_2, until very recently [23, 9], has treated the heavy fermion state, believed to develop starting at $T \sim 60K$ [2, 1], as a persistent character which is only modified by the onset of the phase transition at $T_0 = 17.5$K. Consequently, all observables consistent with heavy fermion behavior down to low temperatures were believed to have their origin in the high temperature crossover regime where the composite many-body states, formed from the localized f-states and the conduction band, begin to develop coherence. In fact, the reduction of the effective mass by one half across the 'hidden' order transition [1] is evocative of partially gapping an already existent heavy band, as would occur in a density wave scenario, for example. It is then not surprising why the recent results probing the temperature dependence of the electronic structure of URu_2Si_2, as presented in this thesis, are so surprising for they reveal for the first time the progenerate connection between the 'hidden' order and the heavy fermion state.

REFERENCES FOR CHAPTER 3

[1] Maple, M., Chen, J., Dalichaouch, Y., and Kohara, T. *Physical Review Letters* **56**, 185–188 (1986).

[2] Palstra, T., Menovsky, A., Berg, J., and Dirkmaat, A. *Physical Review Letters* **55**, 2727–2730 (1985).

[3] Mason, T., Gaulin, B., Garrett, J., Tun, Z., Buyers, W., and Isaacs, E. *Physical Review Letters* **65**, 3189–3192 December (1990).

[4] Denlinger, J. *Journal of Electron Spectroscopy and Related Phenomena* **117-118**, 347–369 June (2001).

[5] Ito, T., Kumigashira, H., Takahashi, T., Haga, Y., Yamamoto, E., Honma, T., Ohkuni, H., and nuki, Y. *Physical Review B* **60**(19), 13390–13395 November (1999).

[6] Park, J.-G., McEwen, K., and Bull, M. *Physical Review B* **66**(9), 094502 September (2002).

[7] Thalmeier, P. and Zwicknagl, G. *Unconventional superconductivity and magnetism in lanthanide and actinide intermetallic compounds*, volume 34, 135–287. Elsevier (2004).

[8] Santini, P. and Amoretti, G. *Physical Review Letters* **73**, 1027–1030 (1994).

[9] Haule, K. and Kotliar, G. *Nature Physics* **5**(11), 796–799 September (2009).

[10] Bonn, D. and Garrett, J. *Physical Review Letters* **61**, 1305–1308 (1988).

[11] Schoenes, J., Schönenberger, C., and Franse, J. *Physical Review B* **35**, 5375–5378 (1987).

[12] Broholm, C., Kjems, J., Buyers, W., and Matthews, P. *Physical Review Letters* **58**, 1467–1470 (1987).

[13] Broholm, C., Lin, H., Matthews, P., and Mason, T. *Physical Review B* **43**, 12809–12822 (1991).

[14] Santini, P. *Physical Review B* **57**, 5191–5199 March (1998).

[15] Ramirez, A., Coleman, P., Chandra, P., Brück, E., Menovsky, A., Fisk, Z., and Bucher, E. *Physical Review Letters* **68**, 2680–2683 (1992).

[16] Barzykin, V. and Gorkov, L. *Physical Review Letters* **70**, 2479–2482 (1993).

[17] Varma, C. and Zhu, L. *Physical Review Letters* **96**, 036405 January (2006).

[18] Chandra, P., Coleman, P., Mydosh, J., and Tripathi, V. *Nature* **417**, 831–834 (2002).

[19] Rodrigo, J. G., Guinea, F., Vieira, S., and Aliev, F. G. *Physical Review B* **55**(21), 14318–14322 June (1997).

[20] Escudero, R. and Morales, F. *Physical Review B* **49**, 15271–15275 (1994).

[21] Wiebe, C. R., Janik, J. a., MacDougall, G. J., Luke, G. M., Garrett, J. D., Zhou, H. D., Jo, Y.-J., Balicas, L., Qiu, Y., Copley, J. R. D., Yamani, Z., and Buyers, W. J. L. *Nature Physics* **3**(2), 96–99 January (2007).

[22] Balatsky, A., Chantis, A., Dahal, H., Parker, D., and Zhu, J. *Physical Review B* **79**(21), 1–7 June (2009).

[23] Santander-Syro, A. F., Klein, M., Boariu, F. L., Nuber, A., Lejay, P., and Reinert, F. *Nature Physics* **5**(9), 637–641 July (2009).

[24] Yoshida, R., Nakamura, Y., Fukui, M., Haga, Y., Yamamoto, E., nuki, Y., Okawa, M., Shin, S., Hirai, M., Muraoka, Y., and Yokoya, T. *Physical Review B* **82**, 205108 November (2010).

[25] Haule, K. and Kotliar, G. *Europhysics Letters* **89**(5), 57006 March (2010).

[26] Ikeda, H. and Ohashi, Y. *Physical Review Letters* **81**, 3723–3726 (1998).

[27] Harima, H., Miyake, K., and Flouquet, J. *Journal of the Physical Society of Japan* **79**(3), 033705 March (2010).

[28] Manoharan, H., Lutz, C., and Eigler, D. *Nature* **403**(6769), 512–515 February (2000).

[29] Boariu, F., Nuber, A., Santander-Syro, A., Klein, M., Forster, F., Lejay, P., and Reinert, F. *Journal of Electron Spectroscopy and Related Phenomena* **181**, 82–87 July (2010).

CHAPTER 4

THE FANO LATTICE - IMAGE OF THE KONDO LATTICE

4.1 Introduction

The STM possesses the unique capability of measuring the local electronic structure of materials. In a Kondo lattice, where the complex interplay between localized and delocalized states is key to that electronic structure, access to the spatial variations of the density of states is crucial. The introduction of spectroscopic STM techniques into Kondo impurity systems began with studies of magnetic adatoms sitting on top of metallic surfaces [1, 2]. The observation of the resultant localized Kondo resonance yielded information about the renormalized local state energy, the strength of the hybridization with the conduction sea and the spatial extent of the many body state. However, rather than a sharp peak as the expected signature of the Kondo resonance, the asymmetric line shape in the conductance, the *Fano resonance*, required a deeper understanding of the probe's influence on the observables and eventually found its roots in the physics of the 1960's [3]. As there are fundamental differences in between Kondo impurity and Kondo lattice systems, the question arises as to what would be the corresponding change in observables as observed by STM and consequentially what they reveal about the nature of heavy fermion physics.

URu_2Si_2 provides a unique context for these first SI-STM studies of Kondo lattice materials. It not only allows for measurements on a purported heavy fermion system but also on the reordering of the electronic structure from within such a state with the onset of the 'hidden' order.

4.2 The Fano Spectrum

The generic problem of a discrete state interacting with a continuum of states is ubiquitous in physics. In condensed matter systems, a frequently occurring realization is comprised of an electronic state of an impurity atom immersed within a host lattice of a metal. When the impurity has magnetic character, the interaction can give rise to the Kondo effect. Within the context of atomic physics, Fano [3] discussed related effects, as they might appear on observable absorption line shapes or resonant electron scattering cross sections which are due to the configuration interaction (CI) that couples a discrete two-electron excited atomic state with a continuum of ionization states. While the typical line shape for such a resonance is Lorentzian, when studied by experiments in which an external probe interacts with the system, the line shape can instead become asymmetrically formed. Such spectra are referred to as *Fano resonances*. The asymmetry is due to interference between the excitation or decay into CI-mixed discrete and continuum states which both couple to the external probe. If the coupling between the probe and continuum is expressed in terms of an energy-independent matrix element t_c, and the interaction between the probe and the localized state, which has already been diluted by admixture into the continuum, by the matrix element $\tilde{t}_a$, then the observed line shape has was derived to have the form

$$I \propto \frac{(\zeta + 2(E - \varepsilon_0)/\Gamma)^2}{1 + (2(E - \varepsilon_0)/\Gamma)^2} \tag{4.1}$$

where ϵ_0 is the energy level of the discrete state, E the excitation energy, $\zeta = \tilde{t}_a/(2\pi V t_c)$, with V being the hybridization strength, or CI-matrix element between the local state and the continuum [4]. The latter coupling results in the discrete state acquiring a width $\Gamma = 2\pi\rho_s V^2$, with ρ_s the density of continuum

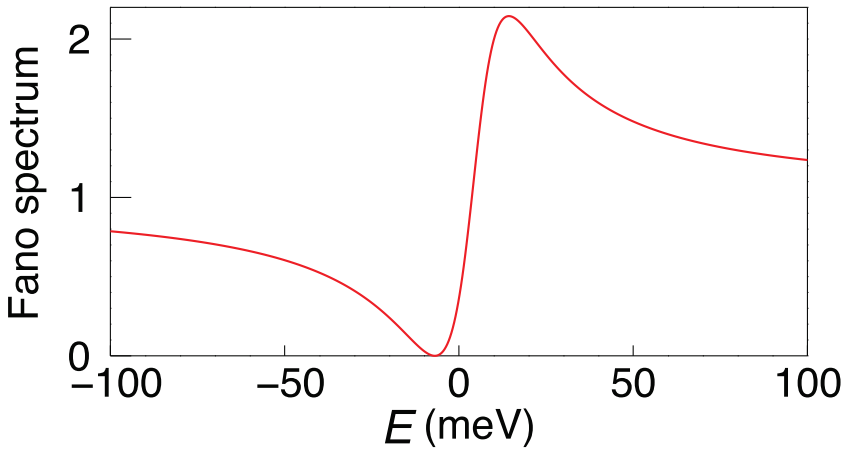

Figure 4.1: Fano spectrum represented by equation 4.1.

states. Figure 4.1 represents a Fano lineshape centered near zero energy with a finite asymmetry parameter ζ.

4.3 Impurity Kondo Resonance in SI-STM: Fano Resonance

The presence of the Kondo resonance in dense Kondo systems such as Ce-heavy-fermion compounds has been experimentally tested by high resolution photoemission electron spectroscopy and by inverse photoemission [5, 6, 7, 8]. While such measurements probe an ensemble of many-body states, STM can detect the properties of a single Kondo site. By the turn of the last century Kondo impurity states were imaged [1, 2, 9, 10] in which the tip-sample differential tunnelling conductance $dI/dV(\mathbf{r}, E) \equiv g(\mathbf{r}, E)$ is proportional to the local density of electronic states $LDOS(\mathbf{r}, E)$, in the weak tunneling limit. However, the manifestation of the many-body resonance as observed through tunneling is not the expected peak in the density of states near the chemical potential but rather resembles the Fano resonance described by equation 4.1.

The origin of the Fano resonance in Kondo impurity systems probed by STM became well understood by appealing to Fano's original ideas [3]. When an adatom, resulting in a magnetic moment, is placed on top of a metal surface, the binding energy of the occupied $4f^1$ state is positioned well below the chemical potential, as shown in figure 4.2a. For a large on-site correlation U and at sufficiently low temperatures, below T_K, the antiferromagnetic exchange interaction between electrons of the host metal and the localized magnetic state on the adatom creates the Kondo resonance close to the chemical potential as illustrated in figure 4.2b. Electrons originating from the probing tip have now three paths to tunnel into the sample. They can tunnel directly into empty bulk states above the chemical potential, E_F, of the metal (path 1 of figure 4.2c), into the Kondo resonance which lies close to E_F (path 2) or indirectly via a spin-flip process into the hybridized and localized state of the magnetic adatom (path 3). The two different paths which conserve the spin (paths 1 and 2) are chosen by the tunneling electrons with probabilities given by the tunneling matrix elements t_c and t_f for tunneling into bulk states and the Kondo resonance, respectively. As a result, the tunneling conductance $dI/dV(\mathbf{r}, E) \equiv g(\mathbf{r}, E)$, being a coherent quantum effect, is determined by the quantum interference between both channels [1, 4] and parameterized by

$$g(\mathbf{r}, E) \propto \frac{(\zeta + E')^2}{E'^2 + 1} \quad \text{where} \quad E' = \frac{E - \varepsilon_0}{\Gamma} \,. \tag{4.2}$$

Here E is the electron energy, ε_0 is the energy of the many-body state and Γ is proportional to the local hybridization strength of the local moment with the conduction sea. ζ is the ratio of the probabilities of tunnelling into the quasi-discrete localized many-body state or into the delocalized $\mathbf{k}$-space states of the host metal. If ζ were zero, indicating that there is no direct coupling to the quasi-discrete state, equation 4.2 predicts a dip in the conductance, indicative

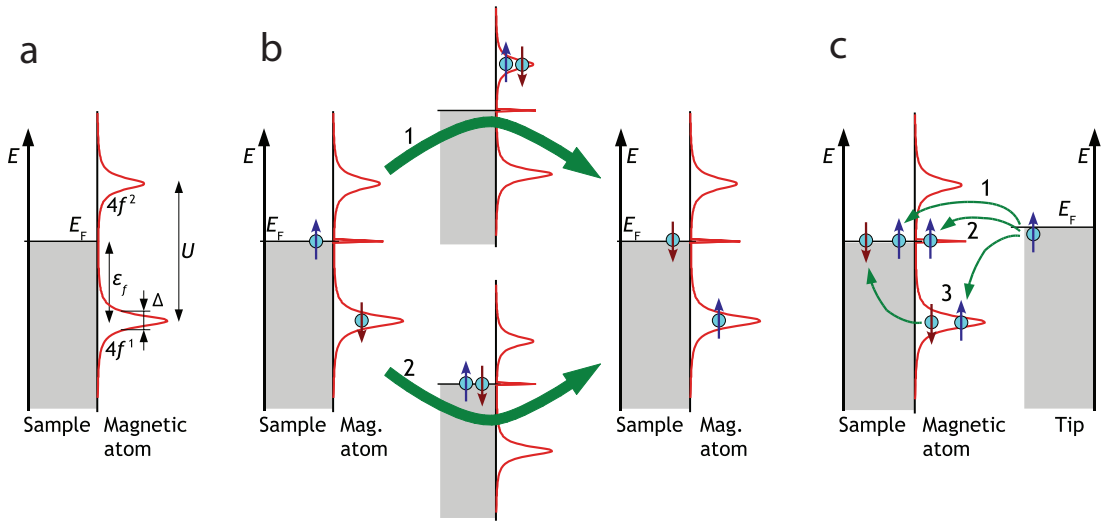

Figure 4.2: Origin of Fano resonance in SI-STM experiments. **a**, Schematic of the energy-dependent spectral function for a single magnetic adatom on a metallic surface. **b**, The Kondo resonance is formed by spin flip scattering processes which couple the f state to the conduction electrons of the metal, eventually leading to a quenching of the magnetic moment on the impurity adatom. The spin of the singly occupied $4f$ state can be flipped by a bulk electron of opposite spin via process 1 or 2 in which the adatom is either doubly occupied (process 1) or empty (process 2) during the intermediate step. **c**, Electrons from a probing STM tip can tunnel directly into the empty conduction states of the sample (path 1) or into the many-body Kondo state (path 2). These tunneling processes conserve the electron spin while the third process is an indirect transition via a spin-flip process on the magnetic adatom (3). The interference of the two tunneling paths leads to the Fano lineshape described by equation 4.1 [11].

of the spectral weight bound up in the many-body state and not available to the single-particle spectral function measured by tunnelling. As ζ increases, an asymmetric line shape develops, a consequence of the mixing of tunnelling paths.

4.3.1 Predictions for SI-STM Observables in Heavy Fermions

For real materials, the Kondo lattice screening processes must be more intricate because the initial unscreened **k**-space state can exhibit an intricate spin manifold and its screening can be due to multiple bands. But despite these complexities, a heuristic hypothesis for SI-STM observables in a heavy fermion system might include a generalization of the Fano spectrum to a 'Fano lattice' - an array of Fano spectra with the same periodicity as the underlying matrix of moment-contributing atoms which are undergoing Kondo screening. Such a generalization would dismiss the stark differences that should exist between a Kondo impurity and Kondo lattice system at low temperatures, the most distinctive being the structure of the density of states near the Fermi level.

Recently, a number of calculations dedicated to predicting STM observables determined that the electronic structure of heavy fermion materials should exhibit some characteristics of a Fano lattice. However, there is considerable disagreement about features at energies comparable to the hybridization gap. In the large-N mean field theory treatment presented by Maltseva *et al.* [12], the passage of electrons from the STM tip to the samples occurs cooperatively with a spin flip of the localized moment. This cotunneling process opens a direct tunneling channel between the tip and composite quasiparticle states of the Kondo lattice, which are modelled by the Kondo Hamiltonian in the usual way. The interference between the direct tunneling process and the cotunneling process is what gives rise to the distinctive double peak spectra, plotted in red in figure 4.3, showing distinctly the hybridization gap in the heavy fermion electronic structure with a background Fano line shape. In a separate mean field calculation by Figgins and Morr [13], similar spectra were generated while also accounting

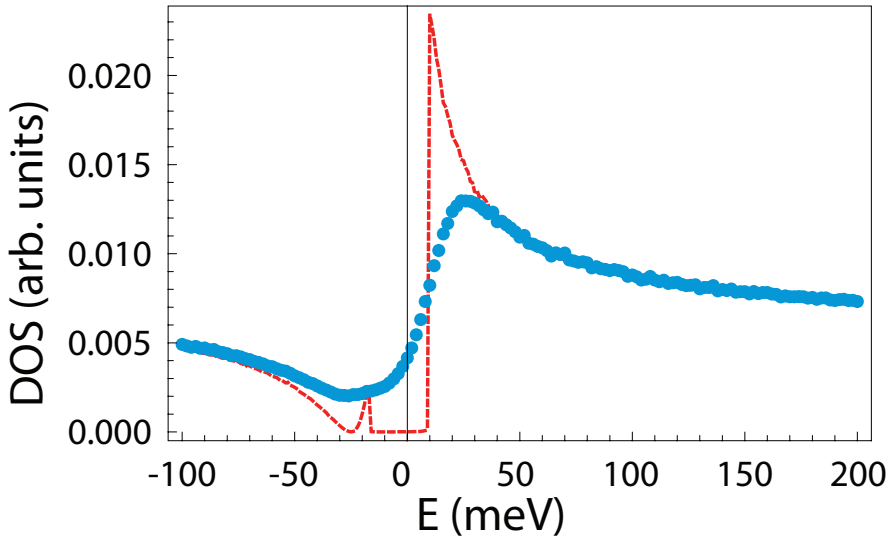

Figure 4.3: Two broad classes of predicted Fano lattice spectra for SI-STM. The red curve represents predictions from mean field theory showing a background Fano spectrum which is gapped close to the Fermi level due to the opening of a hybridization gap [12, 13]. The blue curve, properly representative of aFano spectrum can arise from models accounting for strong correlations [14], CEF states [15], magnetic interactions [13], or decoherence effects [12]. Figure from [14]

for the RRKY interaction. The presence of the magnetic interactions has a large effect on the tunneling conductance observed by STM and can in fact render the hybridization gap unobservable leading a conductance spectrum closer to that of the blue curve in the figure 4.3. Alternatively, disorder effects leading to decoherence can also close the gap in the tunneling spectra [12] once again leading to a typical Fano curve.

The DMFT calculations of Haule and Kotliar [15] meant to specifically address URu_2Si_2, as described in the last chapter, generate spatially resolved spectral functions that in the weak tunneling limit, would be observed by SI-STM. In the temperature scale above the HO transition, Fano spectra are the predicted observables atop the moment contributing U atoms, similar to the blue curve in figure 4.3. However, owing to the specific material for which the calcula-

tion was intended, the Fano spectrum is realized through the interactions of the localized U CEF states with the background *spd* bands without the need for a Kondo resonant state.

Most recently, Wölfle *et al.* [14] asserted that the Fano lattice should be the expected electronic signature of a heavy fermion material and that the hybridization gap as predicted by mean field theory is effectively filled in due to broadened heavy quasiparticle states up to the gap bandwidth. Starting from the low energy domain of the lattice Anderson model, the authors argue that the strong correlations generate a quasiparticle width, γ, which varies with energy as $\gamma \propto E^2/k_B T_K$ in the Fermi liquid regime, where T_K is taken to be the single impurity Kondo temperature, typically much higher than the coherence temperature of a heavy fermion. Consequently, at an energy comparable to the single ion Kondo scale, $\gamma \propto k_B T_K$, which is larger than the hybridization gap, the local f-electron DOS takes the form of a Lorentizian of width T_K. The Fano line shape then develops as usual in the STM conductance spectra as in a single impurity scenario. That the broadening of the quasiparticle width is induced by an *intrinsic correlation* makes the observation of a Fano lattice a universal observable applicable to all heavy fermion materials described the Anderson model.

4.4 Local Conductance Measurements of URu_2Si_2

The experiments to visualize the real space electronic structure of URu_2Si_2 were carried on the two cleave planes described in the last chapter. The Si terminated layer exposed in the pure compound and the U terminated layer from the Th-doped alloy exhibit distinct conductance spectra. However, it is only on the Si

surface, above the HO transition, that a Fano signature is observed, highlighting the differences in the bulk electronic structure projection onto the surface states. Nonetheless, upon descending into the 'hidden' order phase, the spectra from both surfaces equivalently and clearly manifest the onset of changing electronic structure.

4.4.1 $T > T_0$ - The Fano Lattice

In figure 4.4a, a typical Si-terminated topographic image is shown. Plotted in figure 4.4b, as open squares, is the typical spatially averaged spectrum on such surfaces at 19 K where $T > T_0$. The red line is a fit of by equation 4.2, revealing its excellent parameterization as a Fano spectrum (see appendix A). Figures 4.4c-e then show the atomically resolved images of the parameters of the Fano spectrum. Here $\varepsilon_0(\mathbf{r})$, $\Gamma(\mathbf{r})$, and $\zeta(\mathbf{r})$ are determined from fitting conductance curves, $g(\mathbf{r}, E = eV)$, for each pixel within the yellow box in figure 4.4a. Appendix A demonstrates the the high quality of the fits on two representative Si and U sites. Significantly, the maximum in both $\varepsilon_0(\mathbf{r})$ and $\zeta(\mathbf{r})$ and the minimum in $\Gamma(\mathbf{r})$ occur at the U sites (X in Fig. 4.4c-e) as would be expected for a Kondo lattice of U atoms. Specifically, that Γ is minimal on the U atoms supports a picture of a sharply defined state and diminished hybridization with the delocalized states, as expected from renormalization calculations (see Chapter 2, Renormalized Bands). Further support for the Fano picture is provided by the fact that ζ peaks at the same location where the coupling to the quasi-discrete state should be maximal, above the U atoms. These observations, in combination with theoretical predictions for such a phenomenology [12, 13, 14] strongly support that the **r**-space *Fano lattice* electronic structure of a heavy fermion can

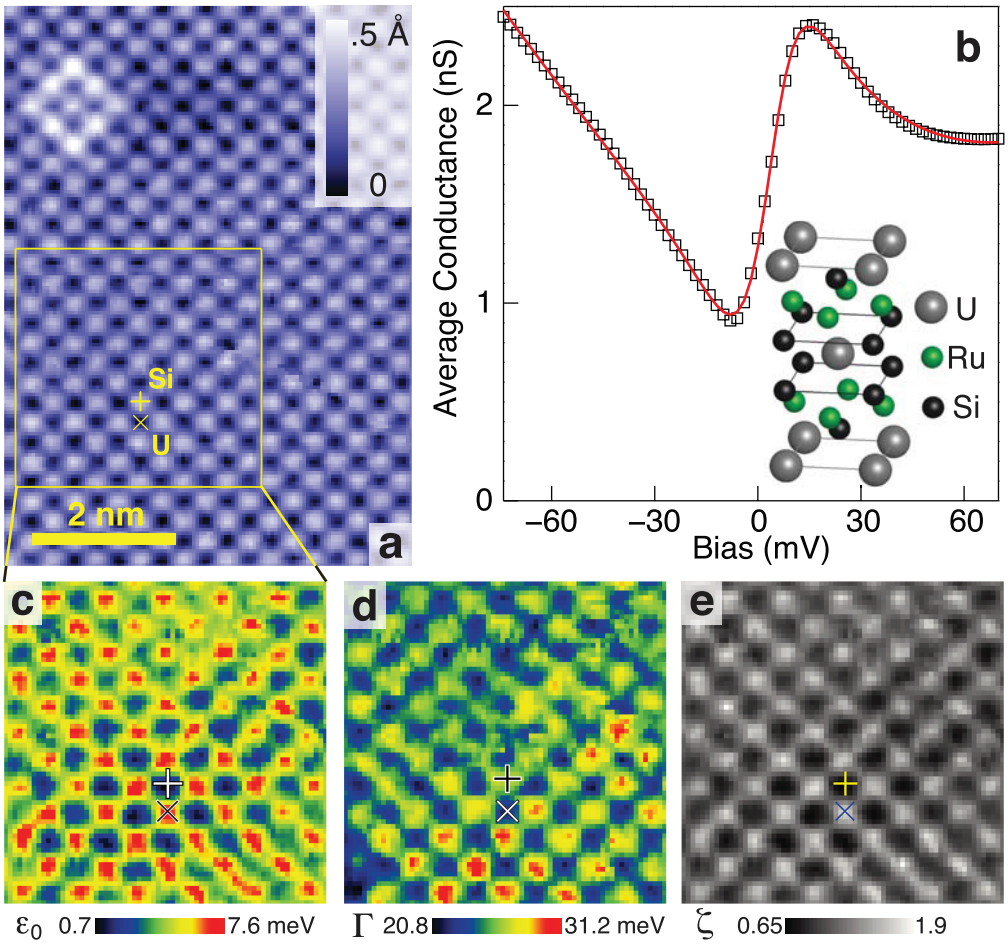

Figure 4.4: Imaging the Fano lattice in URu_2Si_2. **a**, A typical topographic image of the Si-terminated surface of URu_2Si_2. The Si site is marked with a + and the U site with an X. **b**, A typical spatially averaged Fano-like $\langle g(E) \rangle$ spectrum detected on all Si-terminated surfaces of URu_2Si_2 at $T = 19$ K. The inset shows the layered structure of the crystal with the U-terminated surface; the Si-terminated surface is two atomic layers below with each Si at the middle site between four U atoms. **c-e**, Image of the many-body state energy $\varepsilon_0(\mathbf{r})$,the hybridization width $\Gamma(\mathbf{r})$ and the ratio of electron tunnelling probability $\zeta(\mathbf{r})$, respectively, extracted from fitting the spatially resolved Fano spectrum according to equation 4.2. The FOV is indicated by the yellow box in **a** and U atoms are designated by an X.

now be visualized.

4.4.2 Evolution of the Density of States - $T < T_0$

For U-terminated surfaces (see figure 4.5a), the spatially averaged density of states $DOS(E) \propto \langle g(E) \rangle$ spectrum for $T > T_0$ is less structured than that of the Si-terminated surface in figures 4.4a and 4.5c. Typical $\langle g(E) \rangle$ spectra are shown as open squares for each listed temperature between 18.6 K and 1.9 K in the inset to Fig. 4.5a, with the top spectrum being characteristic of $T > T_0$. Upon cooling through T_0, strong changes are detected in the $DOS(E)$ in a narrow energy range (inset to figure 4.5a). By subtracting the spectrum for $T > T_0$, the modifications to the $DOS(E)$ due to the 'hidden' order state are shown to emerge rapidly below T_0 (figure 4.5b). They are not particle-hole symmetric, with the predominant effects occurring between ±4 meV. For the Si-terminated surfaces upon cooling below T_0, the background Fano lineshape of the $DOS(E)$ as reported in figure 4.4c-e is unchanged, as seen in figure 4.5c. In the inset to the same figure, the evolution of the $\langle g(E) \rangle$ spectrum between 19 K and 1.7 K is shown. In each case, the red line is the fit to the Fano spectrum at each temperature (excluding the data points in the bias range -7.75 mV to 6.75 mV) while the measured $\langle g(E) \rangle$ spectra are shown as open squares (see appendix A). Again, by subtracting the fitted Fano spectrum from the $\langle g(E) \rangle$ at each T value the temperature dependence of the hidden-order $DOS(E)$ modifications is determined (figure 4.5d). At no E value on either surface do these $DOS(E)$ spectra represent a complete gap. Finally, no changes are observed in the high-energy $DOS(E)$ as the temperature falls below T_0, (see appendix B) perhaps indicating that the basic Brillouin zone geometry is not altered by the transition. However, a true test of this hypothesis would require measurements to much larger biases.

Figures 4.5(b) and (d) render the emergence of new features at low ener-

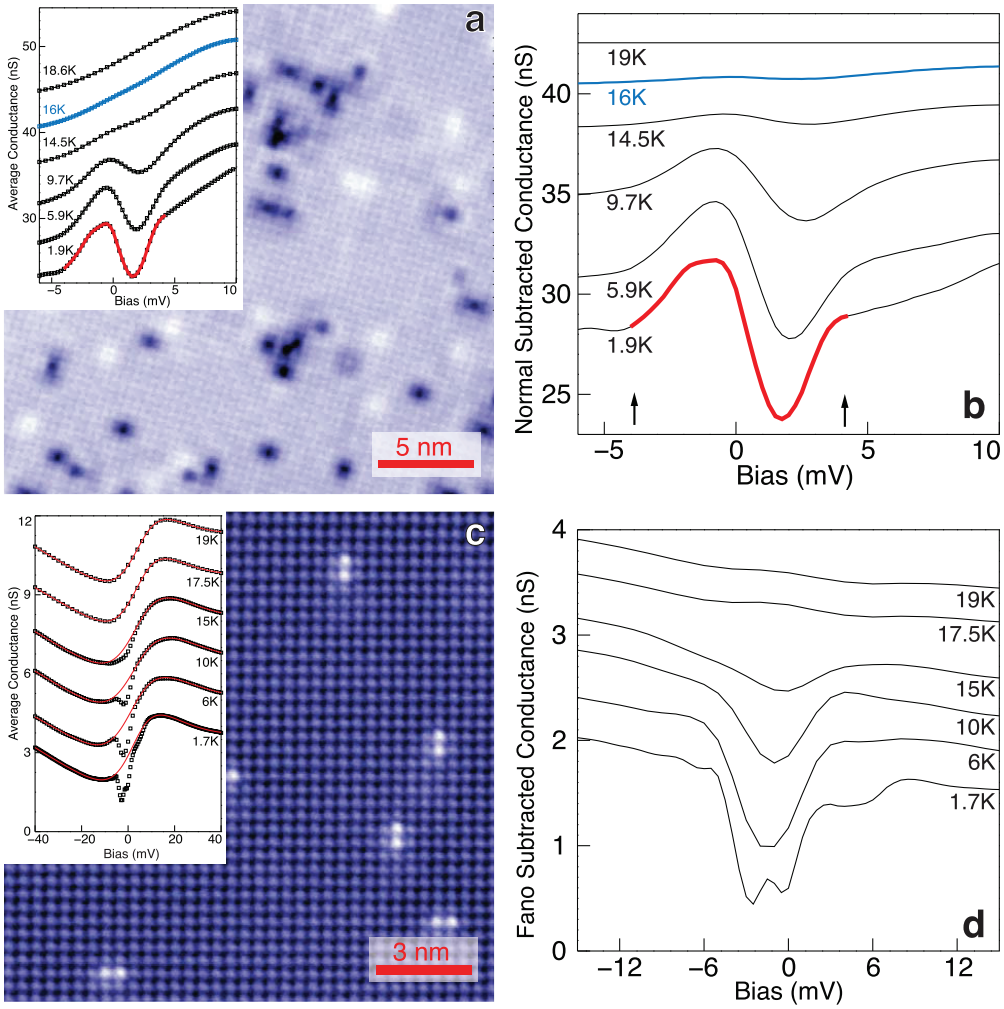

Figure 4.5: Evolution of DOS(E) upon entering the hidden-order phase. **a**,**c** Topographic image of the U-terminated and Si-terminated surface, respectively, with the temperature dependence of their spatially averaged spectra $\langle g(E) \rangle$ in the inset. Each of these spectra is shifted vertically by 5 nS for clarity. Blue data are within 1 K of T_0 for 1% Th-doped samples. **b**, Temperature dependence of DOS(E) modifications due to the appearance of the hidden order at the U-terminated surfaces. Each spectrum is derived by subtracting the spectrum for $T > T_0$ (and shifted vertically for clarity). The DOS(E) changes are limited to approximately ±5 meV. **d**, Temperature dependence of DOS(E) modifications due to the appearance of the hidden order at the Si-terminated surfaces. Each spectrum is derived by subtracting the fit to a Fano spectrum (equation (4.2)), which excludes data points in the range -7.75 mV to 6.75 mV. The DOS(E) changes are again limited to approximately ±5 meV.

gies in the density of states revealed through measurements on the U surface of $U_{0.99}Th_{0.01}Ru_2Si_2$ and the Si surface of URu_2Si_2, respectively. Based on the Si layer spectra, there is a clear formation of a soft gap while on the U layer there is a redistribution of spectral weight inside a narrow low energy band as compared to the 19 K spectrum (red highlighted portion of curve in figure 4.5b). The inferred gap width, associated with the 'hidden' order transition, from specific heat studies of these compounds [16] are in relatively good agreement with the SI-STM determined spectroscopic gap. Figure 4.6a shows that the DOS gap observed on the Si surface of the undoped sample is approximately 10mV while the specific heat measurements [16] give an estimate of 11mV. Based on Th dilution studies [17], the HO gap is reduced to values below 10mV, possibly down to 5mV at 1% doping. However, the U-layer spectra show no clear gap structure and a meaningful comparison is not possible at this time. Nonetheless, the narrow band in which the low temperature spectra deviate from those above the HO transition also has a 10mV width (see figure 4.6b).

While the effect of Th-doping is not immediately distinguishable in the low temperature spectroscopic features, the temperature suppressed onset of the 'hidden'order is captured by detecting the first deviations away from the 19 K data. In figure 4.5b, such an observation is made near 16 K as opposed to the 17.5 K, expected for a pure sample, and is in accord with bulk measurements [17].

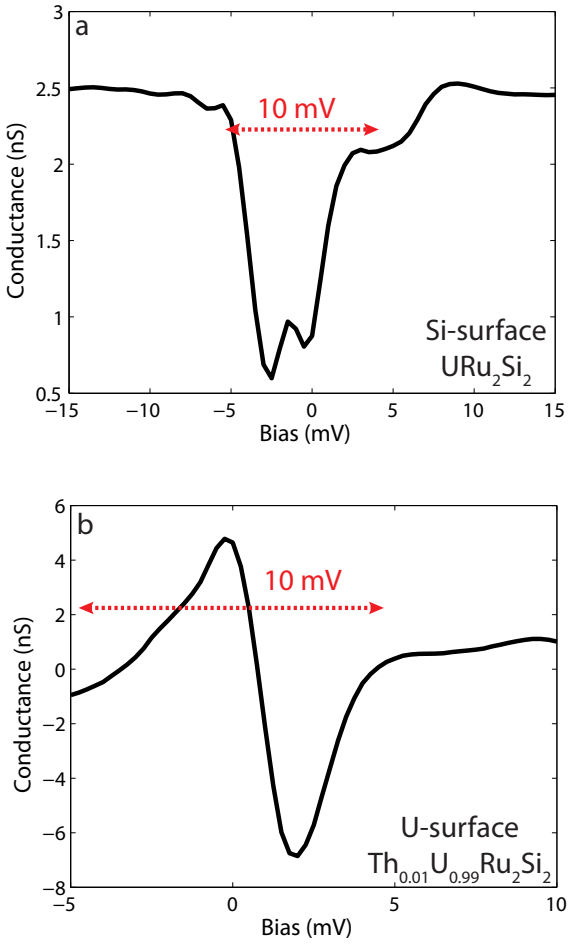

Figure 4.6: Comparison of the spectroscopic gap features of URu_2Si_2. **a**, Extracted gap feature on the Si surface of URu_2Si_2. **b**, Characteristic gap like feature on the U surface of $U_{0.99}Th_{0.01}Ru_2Si_2$. The estimated values of the gap are in good agreement with bulk thermodynamic measurement for both compounds

4.5 Discussion and Conclusions

At 19 K URu_2Si_2 is allegedly in a heavy fermion state [18, 16, 19]. In light of the theoretical discussion presented above, the observation of a Fano lattice, without the heavy fermion signature hybridization gap, can arise in one of several ways and which of these explanations is the correct one is unknown. In one case, it can be attributed to the details of the system involving decoherence effects [12] or additional magnetic interactions [13]. In another, broadened

quasiparticle states mask the gap [14], and in the most extreme case there is no Kondo hybridization gap at all [15]. Regardless, the finding strongly supports that the **r**-space 'Fano lattice' electronic structure of the heavy fermion state can now be visualized. Certainly, the universality of the Fano lattice needs to be experimentally verified in other heavy fermion compounds. As demonstrated, this observation may be contingent on having access to the correct sample termination layer, such as the Si surface in URu_2Si_2.

The descent into the 'hidden' order state is marked by alternations to the electronic structure in a narrow 10mV span about the chemical potential. The Si spectra show the development of a pseudogap in this window while the U spectra indicate a redistribution of spectral weight. The proposed mean field thermodynamic gap associated with the HO transition, [16], has a low temperature value equivalent to that of the spectroscopic pseudogap. In another set of STM experiments on the same compound [20], the authors have tried to strengthen the link by showing that the spectroscopic gap follows a temperature dependent power law that would be expected for a mean field transition. However, temperature dependent analysis on the the data presented in this thesis has not yet found an equivalent trend and alternatively likens the spectroscopic gap in URu_2Si_2 to the pseudogap in the cuprates in which the gap width remains essentially constant but deepens with diminishing temperature (see appendix C). Hence, the connection between the spectroscopic gap and the mean field HO gap is uncertain, the equivalence of their values being either coincidental or potentially more deeply connected. The question then remains as to what is the source of the low energy DOS alterations observed in the SI-STS. Addressing this issue requires exploring the momentum space structure of URu_2Si_2, the subject of the following chapter.

APPENDIX FOR CHAPTER 4 A

FANO FIT PROCEDURE

Above the hidden order transition temperature (17.5K), the measured LDOS spectrum at every point of the Si surface can be fitted with high quality to a Fano function plus quadratic background:

$$g(\mathbf{r}, E = eV) \propto \frac{(\zeta + E')^2}{E'^2 + 1} + aV^2 bV^2 + c, \qquad E' = \frac{V - \epsilon_0}{\Gamma/2} \tag{A.1}$$

To account for thermal broadening, in the fits this function was convolved with the derivative of the Fermi-Dirac distribution at every temperature. By varying the bias voltage interval over which the data is fit from [-40, 40mV] to [-75, 75mV], the Fano parameter lattice presented in figure 4.4 does not change qualitatively. Quantitatively, the mean values of ϵ_0 and Γ shift by 1.5 meV and 3 meV respectively, and ζ shifts by 0.2. The change of the standard deviation of these parameters is less than 5% so that the systematic effect of varying the bias interval over which the fit is performed is a primarily a rigid shift of Fano parameters, maintaining the shapes of their distribution. Examples of fits to a single spectrum, above 17.5K, at a Si site and at a U site are shown in Figure S1.

Below 17.5K, a dip is observed to open in the Si Layer LDOS spectrum in the vicinity of ϵ_0. This dip does not appear to be due to a drastic change in the Fano parameters with temperature but instead appears to be a non-Fano gap opening over a larger Fano lineshape that is not changing significantly with temperature. To test this hypothesis, the thermally broadened Fano function was fit at every temperature excluding the bias interval [-7.75, 6.75]. This produces the red lines over the data inset in figure 4.4c. The excellent agreement of these fits with the excluded data at 17.5K and 19K confirms the internal consistency of this

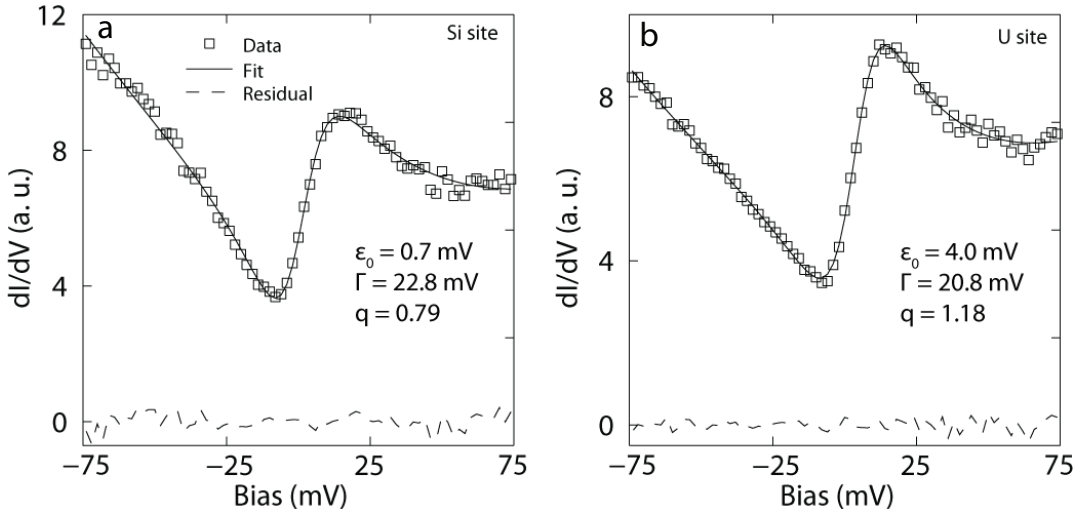

Figure A.1: Representative Fano fits to Si and U site spectra. Resulting fits of the Fano function in equation A.1 to individual measured spectra on a **a** Si site and on a **b** U site at T = 19K.

exclusion procedure.

APPENDIX FOR CHAPTER 4 B

STATIC HIGH ENERGY DOS FEATURES

Crossing into the 'hidden' order phase, the U surface exhibits a redistribution of spectral weight at low energies, close to the chemical potential (see figure 4.5). To address the question of whether there is an accompanying high energy spectral shifts, additional high bias DOS measurements were made. Figure B.1 shows the temperature dependent conductance spectra averaged over a 10nm×10nm area. Near zero bias, the dip-hump structure reported in the main text (see figure 4.5) is clearly seen to evolve with temperature. Features outside this narrow window, however, remain static and show no changes brought upon by the transition to the ordered state. Hence, the high bias data demonstrates that there are no DOS alterations up to ±100 mV in this portion of the electronic structure.

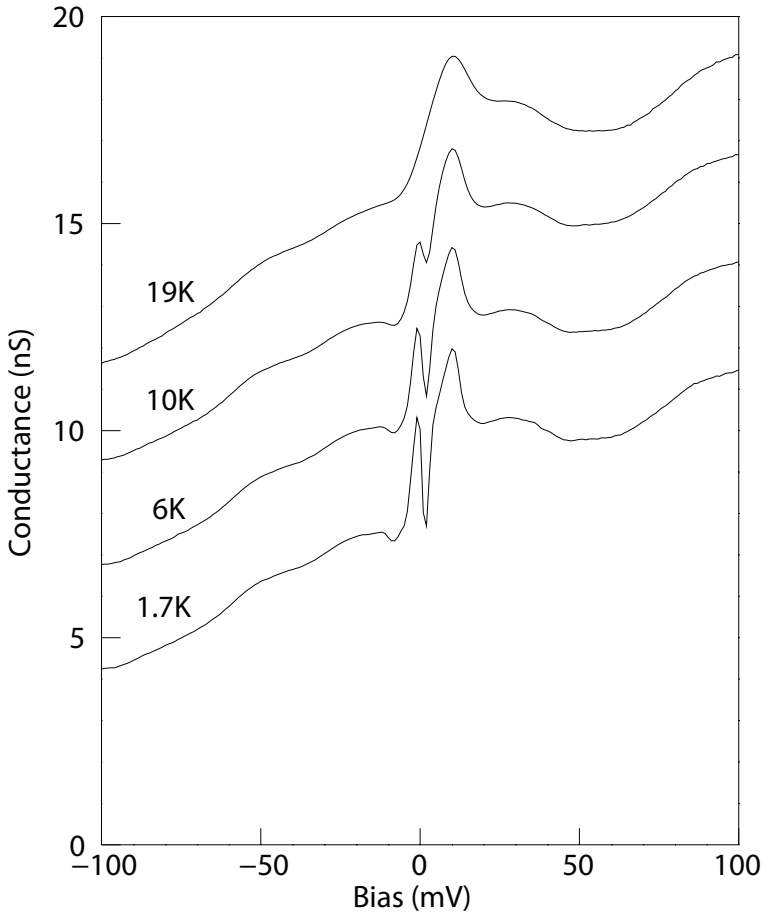

Figure B.1: Temperature dependent, 10nmx10nm spatially averaged high bias conductance spectra measured on the U-layer of $U_{0.99}Th_{0.01}Ru_2Si_2$

APPENDIX FOR CHAPTER 4 C

TEMPERATURE DEPENDENCE OF GAP DEPTH

The evolution of the electronic structure below T_0 reveals deepening depressions in the density of states with falling temperature. While there is clearly a gap feature in the Si spectra (figure 4.5d) the U data is more ambiguous with an energy window in which the DOS deviates from the normal state line shape (figure 4.5b). However, for comparison, the size of the depression from both data sets are plotted as a function of temperature in figure C.1. Both plots show a simple evolution of these features with temperature.

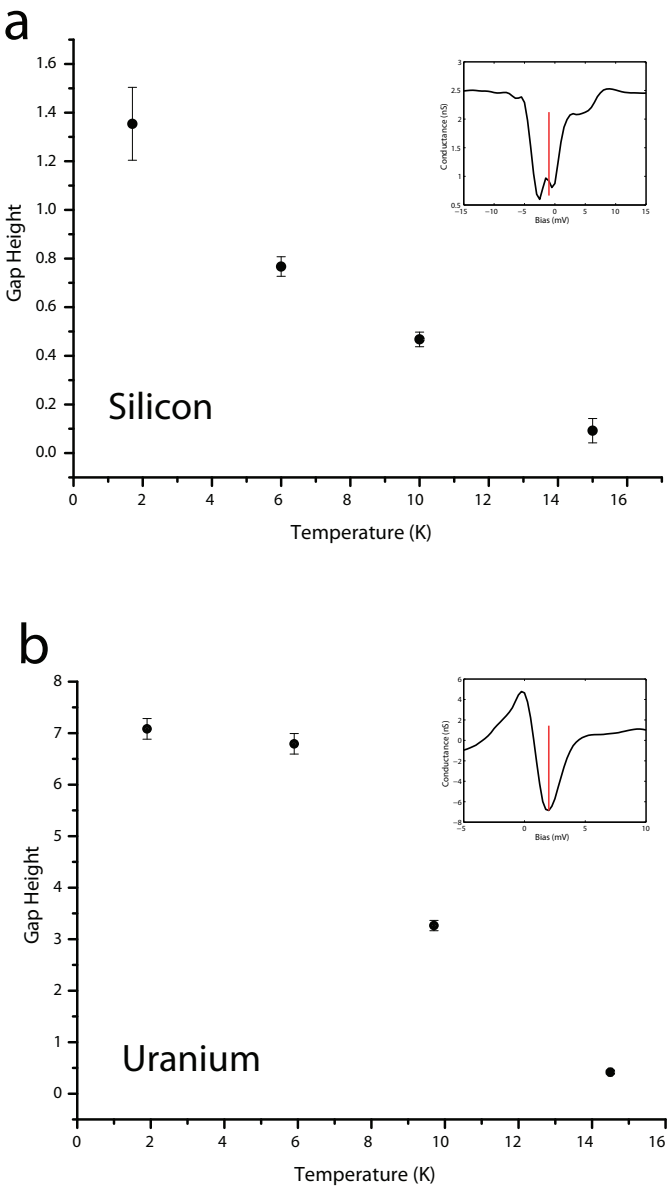

Figure C.1: DOS depression size as a function of temperature. **a**, The amplitude of the gap depth of the density of states on the Si terminated layer. **b**, The amplitude of the depression in the density of states just above the chemical potential

REFERENCES FOR CHAPTER 4

[1] Madhavan, V., Chen, W., Jamneala, T., Crommie, M. F., and Wingreen, N. *Science* **280**, 567–569 April (1998).

[2] Li, J., Schneider, W.-D., Berndt, R., and Delley, B. *Physical Review Letters* **80**, 2893–2896 March (1998).

[3] Fano, U. *Physical Review* **124**, 1866–1878 (1961).

[4] Plihal, M. and Gadzuk, J. *Physical Review B* **63**(8), 085404 February (2001).

[5] Im, H., Ito, T., Kim, H.-D., Kimura, S., Lee, K., Hong, J., Kwon, Y., Yasui, A., and Yamagami, H. *Physical Review Letters* **100**, 176402 April (2008).

[6] Jung, R.-J., Choi, B.-H., Oh, S.-J., Kim, H.-D., Cho, E.-J., Iwasaki, T., Sekiyama, A., Imada, S., Suga, S., and Park, J.-G. *Physical Review Letters* **91**, 157601 October (2003).

[7] Malterre, D., Grioni, M., and Baer, Y. *Advances in Physics* **45**, 299–348 (1996).

[8] Reinert, F., Ehm, D., Schmidt, S., Nicolay, G., Hüfner, S., Kroha, J., Trovarelli, O., and Geibel, C. *Physical Review Letters* **87**, 3–6 August (2001).

[9] Manoharan, H., Lutz, C., and Eigler, D. *Nature* **403**(6769), 512–515 February (2000).

[10] Knorr, N., Schneider, M., Diekhöner, L., Wahl, P., and Kern, K. *Physical Review Letters* **88**(9), 096804 February (2002).

[11] Ternes, M., Heinrich, A. J., and Schneider, W.-D. *Journal of Physics: Condensed Matter* **21**(5), 053001 February (2009).

[12] Maltseva, M., Dzero, M., and Coleman, P. *Physical Review Letters* **103**(20), 206402 November (2009).

[13] Figgins, J. and Morr, D. K. *Physical Review Letters* **104**(18), 187202 May (2010).

[14] Wölfle, P., Dubi, Y., and Balatsky, A. *Physical Review Letters* **105**, 246401 December (2010).

[15] Haule, K. and Kotliar, G. *Nature Physics* **5**(11), 796–799 September (2009).

[16] Maple, M., Chen, J., Dalichaouch, Y., and Kohara, T. *Physical Review Letters* **56**, 185–188 (1986).

[17] Lopez, A., Visani, P., Dalichaouch, Y., Lee, B. W., and Maple, M. B. *Physica B* **179**, 208–214 (1992).

[18] Palstra, T., Menovsky, A., Berg, J., and Dirkmaat, A. *Physical Review Letters* **55**, 2727–2730 (1985).

[19] Schoenes, J., Schönenberger, C., and Franse, J. *Physical Review B* **35**, 5375–5378 (1987).

[20] Aynajian, P., da Silva Neto, E. H., Parker, C. V., Huang, Y., Pasupathy, A., Mydosh, J., and Yazdani, A. *Proceedings of the National Academy of Sciences* **107**, 10383–10388 June (2010).

CHAPTER 5

VISUALIZING THE FORMATION OF HEAVY FERMIONS IN URu_2Si_2

5.1 Introduction

The passage into the 'hidden' order phase is accompanied by alterations to the **r**-space LDOS of URu_2Si_2. Based solely on the real space data, the cause of the changes and the link to the 'hidden' order is not certain. Certainly, that both share a common onset temperature and possibly the same gap energy scale points to a strong connection. Alongside, theories of the 'hidden' order fall into two basic classes describing susceptibilities to alterations in either the real or momentum space structure with ensuing changes in the other. As a Kondo lattice system, the interactions between spatially localized and delocalized states represents a crucial element of the active physics and hence information from both the **r**-space and **k**-space channels is crucial. Hence, unravelling the complex set of phenomena in URu_2Si_2 requires a simultaneous knowledge of both the real space and momentum space structure.

SI-STM techniques provide the necessary tools for the simultaneous study of the **r**-space and **k**-space electronic structure evolutions in URu_2Si_2. The tip-sample differential tunnelling conductance $dI/dV(\mathbf{r}, V) \equiv g(\mathbf{r}, E = eV)$ at locations **r** and sample-bias voltage V yields an image proportional to the local density of electronic states $LDOS(\mathbf{r}, E)$. Then the **k**-space electronic structure elements can be determined simultaneously by using quasiparticle interference imaging. [1, 2, 3, 4, 5, 6, 7, 8]. A summary of the method is provided in chapter 1.

5.2 Heavy f-electron Quasiparticle Interference Imaging

To determine the evolution of **k**-space electronic structure through T_0, heavy-electron quasiparticle interference (QPI) imaging was used [8, 9]. The Si-terminated surface has proved unproductive for this purpose because the Fourier transform of its $g(\mathbf{r}, E)$ images are so complex that the multiple bands cannot yet be disentangled. However, in recent studies of heavy-fermion QPI in $Sr_3Ru_2O_7$ it was shown that replacing 1% of the Ru atoms by Ti atoms produced intense scattering interference and allowed successful **k**-space determination [8]. Emulating this approach, 1% Th atoms were substituted on the U sites, which results in crystals usually cleaving at the U layer. The average spectrum on this U-terminated surface develops the narrow resonant $DOS(E)$ structure below T_0 (red data between vertical arrows in Fig. 4.5b), within which intense QPI are observed. The 1% Th substitution suppresses T_0 by only 1 K and does not alter the basic hidden order phenomenology [10, 11], so the phenomena reported are not caused by the dilute Th doping. Moreover, because the energy scale of the $DOS(E)$ alterations is consistent with Th-doped specific heat measurements [10] and because these alterations are already detectable in tunnelling within 1 K below the bulk transition (blue line in figure 4.5b), the electronic structure of the U-terminated surface appears to be bulk representative of the 'hidden' order phase. While it is conceivable that bulk quantities can remain unaltered while microscopic features change as a result of the Th doping, further comparison of the microscopics as well as corroboration by photoemission experiments on undoped URu_2Si_2, to be presented below, speak to the contrary.

For QPI studies of the hidden-order transition the conductance, $g(\mathbf{r}, \mathrm{E} = \mathrm{eV})$,

was measured in a 50nm×50nm field of view (FOV) with 250μV energy resolution and atomic spatial resolution on these U-terminated surfaces. Shown in figure 5.1a-f are simultaneous images of $g(\mathbf{r}, E)$ modulations measured at T = 1.9 K for six energies near E_F within the energy scale where the resonant feature appears below T_0 (figure 4.5b). Figure 5.1g-l shows the six $g(\mathbf{q}, E)$ Fourier transforms of each $g(\mathbf{r}, E)$ image from figure 5.1a-f (see appendix for processing). Four significant advances are already apparent in these unprocessed data. First, the wavevectors of the $g(\mathbf{r}, E)$ modulations are dispersing very rapidly (within the narrow energy range of $DOS(E)$ modifications in figure 4.5b); this is directly indicative of heavy fermions in the 'hidden' order state. Second, the magnitude of their characteristic $\mathbf{q}$ vectors, which are diminishing towards a small value as they pass through the Fermi energy from below (see Fig. 5.1i), suddenly jumps to a large value at a few millielectronvolts above E_F (see Fig. 5.1k). It therefore appears that the band supporting QPI is widely split in $\mathbf{k}$-space at this energy centered a few millielectronvolts above E_F. Third, the QPI oscillations are highly anisotropic in $\mathbf{q}$-space (figure 5.1g-l). Finally, the most intense modulations rotate by 45° when they pass through an energy just above the chemical potential (compare figure 5.1h and l), indicating a distinct $\mathbf{k}$-space electronic structure for the filled and empty gap-edge states. As shown further in figure 5.2, all of these effects are characteristics of the 'hidden' order state.

5.2.1 Evolution of the Momentum Space Structure

To determine the $\mathbf{k}$-space electronic structure evolution into the HO state, the temperature dependence of QPI data equivalent to those in figure 5.1 was measured from just above T_0 down to 1.7 K. The key results are shown in figure

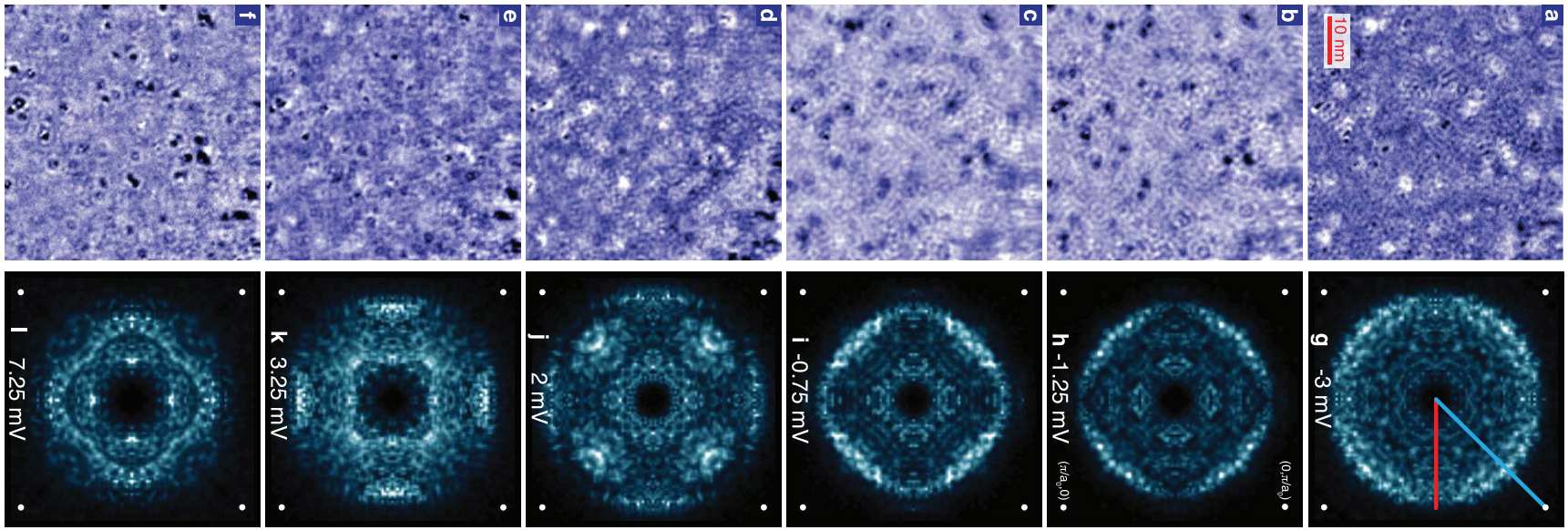

Figure 5.1: Energy dependence of heavy f-electron quasiparticle interference. **a-f**, Atomically resolved $g(\mathbf{r}, E)$ for six energies measured at the U-terminated surface. Extremely rapid changes in the interference patterns occur within an energy range of only a few millielectronvolts. **g-l**, Fourier transforms $g(\mathbf{q}, E)$ of the $g(\mathbf{r}, E)$ in **a-f**. The length of half-reciprocal unit-cell vectors are shown as dots at the edge of each image. Starting at energies below E_F (**g**), the predominant QPI wavevectors diminish very rapidly until **i**; upon crossing a few millielectronvolts above E_F, they jump to a significantly larger value and rotate through 45 °. Then they again diminish in radius with increasing energy.

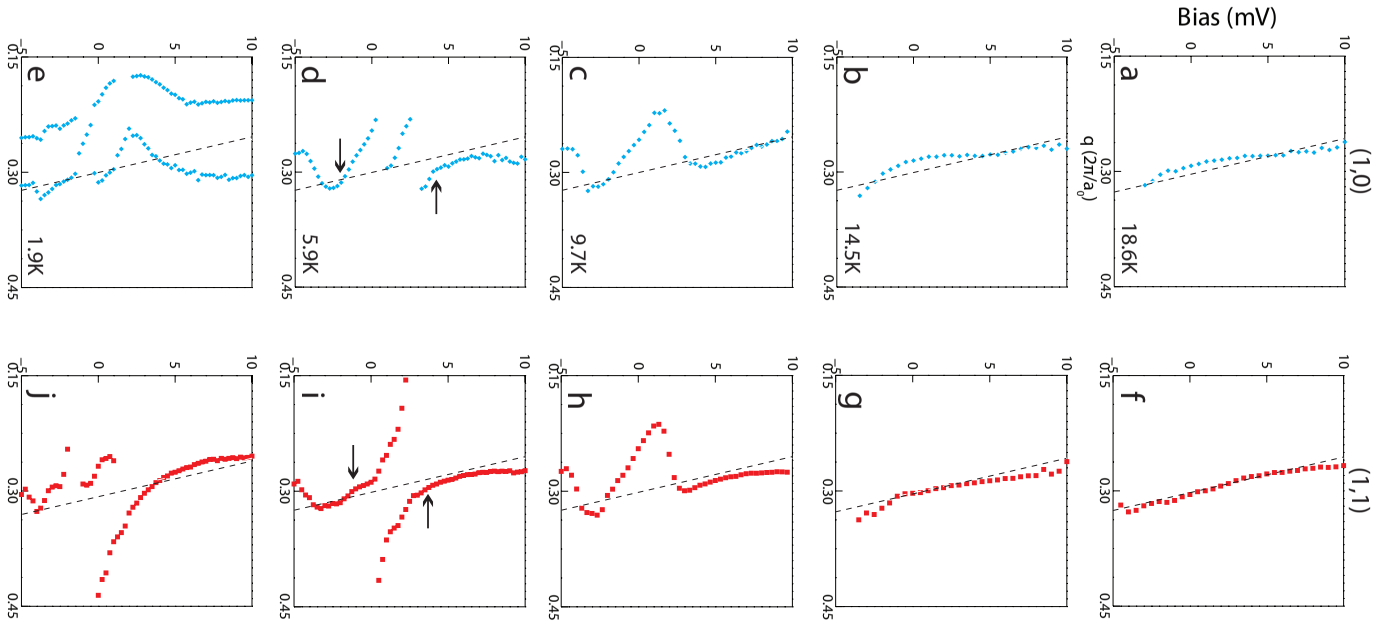

Figure 5.2: Emergence of the two new heavy bands below the 'hidden' order transition. **a-e**, Dispersion of the primary QPI wavevector as a function of T along the (1,0) direction (see Fig. 4g), starting with $T > T_0$. **f-j**, Dispersion of the primary QPI wavevector as a function of T along the (1,1) direction (see figure 5.1g), starting with $T > T_0$. Both sets of panels demonstrate the emergence of two heavy bands from the light ones above T_0, approximately shadowed by dashed lines in all the panels. The bands become well segregated in **k**-space within the hybridization gap, demarcated by black arrows in the 5.9K data. The QPI dispersion at 2K develops additional complex features.

5.2a-j with the relevant **q**-space directions indicated by the blue and red lines on figure 5.1g. Observed with falling temperature below T_0, is the rapid splitting of a light band (crossing E_F near (0, ±0.3) $2\pi/a_0$; (±0.3,0) $2\pi/a_0$ into two far heavier bands which become well separated in **k**-space and with quite different anisotropies. The hybridization energy range as estimated from the observed gap at the avoided crossing (see figure 2.6) is shown by horizontal arrows in figures 5.2d, i and appears anisotropic in **k**-space by a factor of about two. Finally, the $DOS(E)$ changes detected in **r**-space (figure 4.5), namely the development of a gap component and a redistribution of spectral weight in the 'hidden' order phase, occur within the same narrow energy range and develop in tandem over the same temperature scale as the momentum space hybridization features.

As an avenue for further study, at temperatures below 5.9K, the QPI linecuts (5.2e and j) show additional dispersions signaling the development of further changes in momentum space. In fact, some of this additional structure formation is also detected in the evolution of the $DOS(E)$ on the Si terminated surface. In figures 4.5d, the gap structure begins to exhibit new features at 1.9K within the energy range of the gap. Their origin is not yet understood and further work is needed to determine their relationship to the 'hidden' order state.

5.3 Discussion and Conclusions

As QPI is inherently a measure of elastic scattering momentum transfer **q** rather than the actual **k**-space structure, the comparison of the measured QPI dispersions to the momentum space structure requires additional information. For example, if the QPI were generated from intraband isotropic scattering processes

then the connection could be made through $|\mathbf{q}| = 2|\mathbf{k}|$ [1]. Indeed, support for such a hypothesis comes from ARPES [12, 13]: the light band which hybridizes with the f-states crosses the chemical potential close to $|\mathbf{k}| = 0.3(\pi/a_0)$. Equivalently, the light band in $\mathbf{q}$-space crosses the chemical potential at $|\mathbf{q}| = 0.3(2\pi/a_0)$, thus supporting the intraband isotropic scattering scenario, at least in a small window around the chemical potential. The observation allows for a simple translation between the QPI and the momentum space features.

The QPI observations in figure 5.1 and 5.2 reveal a light hole-like dispersing band crossing E_F near $\mathbf{k} = 0.3(\pi/a_0)$ above T_0 that undergoes rapid temperature changes below T_0. The resulting evolution splits the band into two far heavier ones that are widely separated in $\mathbf{k}$-space (figures 5.1g,l, 5.2c and d) within an energy range coincident with changes in spectrum near E_F measured on both the Si and U surfaces (figure 4.5). The original light band with $m^* \approx 8m_e$ does not account for the $m^* \approx 50m_e$ deduced from specific heat measurements for $T > T_0$ [14]; resolution of this issue will require future study and is briefly discussed in the next chapter. Nevertheless, below T_0 there arise two heavy bands, one of which crosses E_F with $m* \approx 53m_e$ in the (1,0) direction and another with $m* \approx 17m_e$ in the (1,1) direction (figure 5.2). Using the geometric mean to estimate the average over $\mathbf{k}$-space, $m^* \approx 28m_e$ from the QPI data while both thermodynamics [14, 15] and ARPES [12, 13] report $m^* \approx 18 - 29m_e$ for $T \ll T_0$. Moreover, the position of the heavy band in the HO state, as determined by ARPES [12, 13] sits 3-5meV below the chemical potential, in accord with the lower gap edge in the LDOS data (figure 4.5) and with the lower edge of the direct gap marked in figure 5.2. Finally, the spectroscopic signature of the transition temperature is detected to within to within 1 K of the bulk value [14, 10] (figure 4.5). Thus, there is excellent consistency between the electronic structure of the 'hidden'

order state deduced from thermodynamics, photoemission and the new SI-STM approach.

The dramatic alteration of the electronic structure observed through QPI in figure 5.2d and i bear a striking similarity to the Kondo lattice heavy fermion band structure, as depicted in figure 2.6. Thus, it appears that some sudden modification of the real space states periodic with the moment-contributing U atoms (4.5) generate a new set of heavy bands in momentum space (figures 5.1 5.2) and that the sum of these effects is directly tied to the onset of the 'hidden' order transition. The result raises the possibility of a rather complex set of Kondo interactions involving the U atoms, those which are responsible for the heavy fermion character above T_0, and those giving rise to the heavy bands below T_0. Compounding the intricacy, the effective mass below T_0, as derived from specific heat [14], is completely accounted for by the new heavy bands in the HO state.

Alternatively, if the 'hidden' order below T_0 were a conventional density wave, non-dispersive modulations at $\mathbf{Q}^*$ should appear in the gap-edge states both above and below E_F in $g(\mathbf{q}, E)$ and in the topographs, but no such phenomena are detected (see appendix D). Moreover, because the high spectral weight gap-edge states in the 'hidden' order phase are at completely different $\mathbf{k}$-space locations below and above E_F (figures 5.1 and 5.2) and the indirect gap does not straddle E_F [16], these effects are also exclusive of a conventional density wave.

It is tempting to associate the hybridization gap seen in both the $\mathbf{r}$-space (figure 4.5) and $\mathbf{k}$-space (figure 5.2) observables to the gap attributed with the 'hidden' order transition. But there is no known case, both theoretically or experimentally, in which the formation of a heavy fermion hybridization gap is

the fundamental signature of a broken symmetry leading to a phase transition. Nonetheless, the connection is beyond coincidence and the interplay will be expanded upon in the next chapter.

APPENDIX FOR CHAPTER 5 D

ABSENCE OF CONVENTIONAL DENSITY-WAVE STATES

In conventional metallic systems, the opening of an energy gap below some critical temperature usually occurs as a result of a diverging susceptibility of the **k**-space states surrounding E_F. The pre-existing band structure is unaltered except within a few $\pm\Delta$ of E_F. Exemplary of such transitions are those to Peierls charge-density-wave or spin-density-wave states [17]. The **r**-space modulations in charge and/or spin appear at a fixed wavevector $\mathbf{Q}^*$-which is the same for empty and filled gap-edge states, and the associated gap always spans E_F. In Kondo lattice systems, in contrast, the opening of a gap near E_F is due to a profoundly different phenomenon [18, 19, 20, 16]. Hybridization between the **r**-space and **k**-space electrons splits a light band into two heavy bands approximately separated in energy by the hybridization range ($\widetilde{V}_k$ in equation (2.23)) and segregated widely in **k**-space (figure 2.6).

To address the possibility that the HO state is a conventional density wave state, a search for the essential signatures was carried out. First, high-precision topographic images of both Si-terminated and U-terminated surfaces were acquired and analyzed over the same range of temperatures as in figure 5.1 searching for any additional, bias-independent, modulation wavevectors $\mathbf{Q}^*$ appearing below T_0 in the Fourier transform of the topograph (see figure D.1). Second, the temperature dependent $g(\mathbf{r}, E)$ were analyzed, in search of modulations at fixed $\mathbf{Q}^*$ which are the same for empty and filled gap-edge states. Third, the energy gap structure in **k**-space revealed by figure 5.2d and i were considered. Because these signatures are not observed at any temperature below T_0 for any topographs or $g(\mathbf{r}, E)$ maps and because the observed **k**-space alterations do not

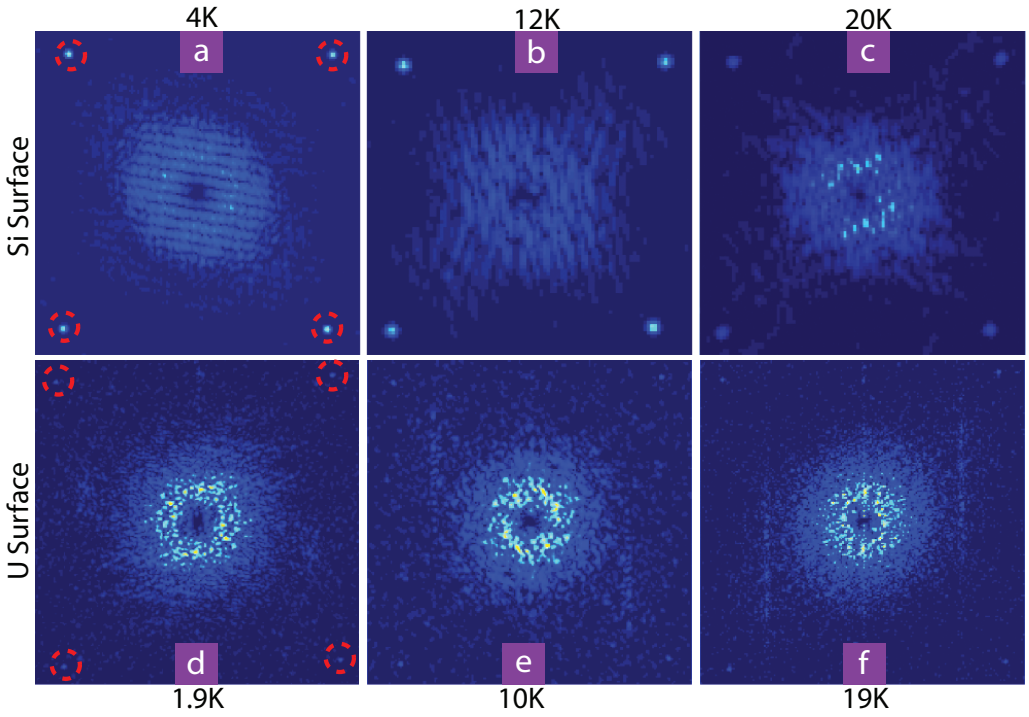

Figure D.1: Search for conventional density wave in topographic data. Fourier transform of the U-layer **a-c** and Si-layer **d-f** topographs across temperatures above and below the hidden order transition. The dotted red circles are a guide to find the regions of the Bragg peaks in each of the panels. There are no additional detectable **Q*** wavevectors signaling the presence of a conventional density.

result in a gap spanning E_F (Fig. 5.2d and i), there is firm evidence that a conventional density wave does not appear to be present at $T \ll T_0$ in URu_2Si_2.

APPENDIX FOR CHAPTER 5 E

EXTRACTION OF QPI MODULATION VECTORS VIA POWER SPECTRA DENSITY ANALYSIS

Real space modulations observed in the conductance maps arising from quasi-particle interference, are made manifestly clear by utility of Fourier transform techniques. To enhance the signal to noise ratio (S/N) of the modulation vectors in the conjugate representation (**q**-space), additional steps are employed. Starting from the 2-D power spectral density (PSD) of the conductance data, linear transformations are applied to restore the lattice symmetry that may have been distorted due to piezo relaxation effects of the STM actuators. Each energy layer is then symmetrized along the high crystalline symmetry directions (1,0) and (1,1) yielding enhanced visibility of the QPI wavevectors. Figure E.1 makes evident the significant improvement in S/N but with no change in the fundamental content of the data by applying this procedure.

The dominant QPI modulation wavevectors associated with the onset of hidden order are extracted from the **q**-space representation of the data by performing linecuts, with transverse multi-pixel averaging, along the (1,0) and (1,1) directions. By applying a Lorentzian fit, the magnitude of the QPI vector, q =|**q**|, can be determined with great precision and its energy dispersion traced as the procedure is applied to each energy layer of the conductance map. As a representative sample, a series of cuts along the (1,1) direction is shown in figure E.2.

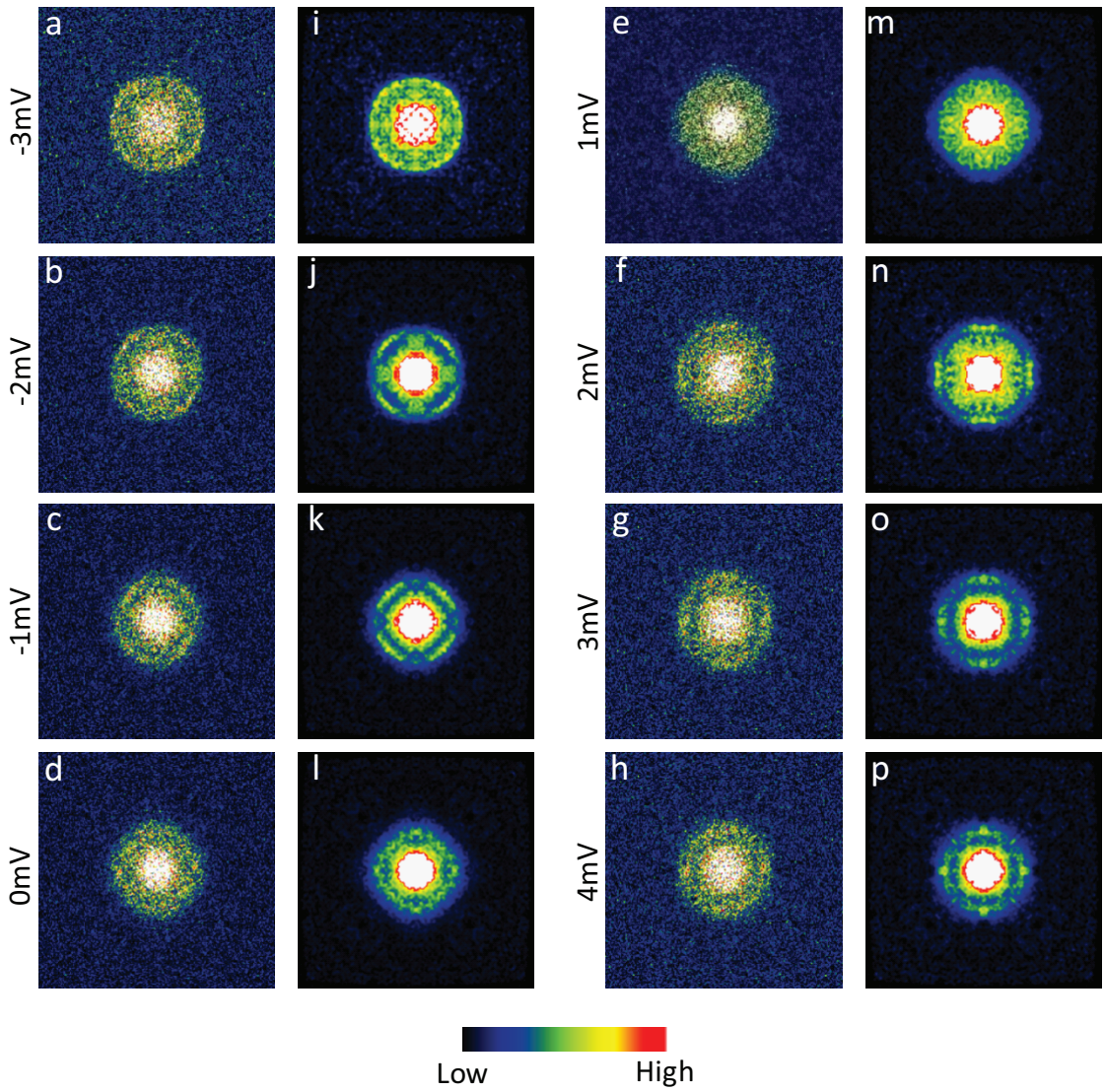

Figure E.1: Fourier transform QPI processing. Comparison between raw **q**-space data **a-h**, and **q**-space data treated with the procedure described in this section, **i-p**.

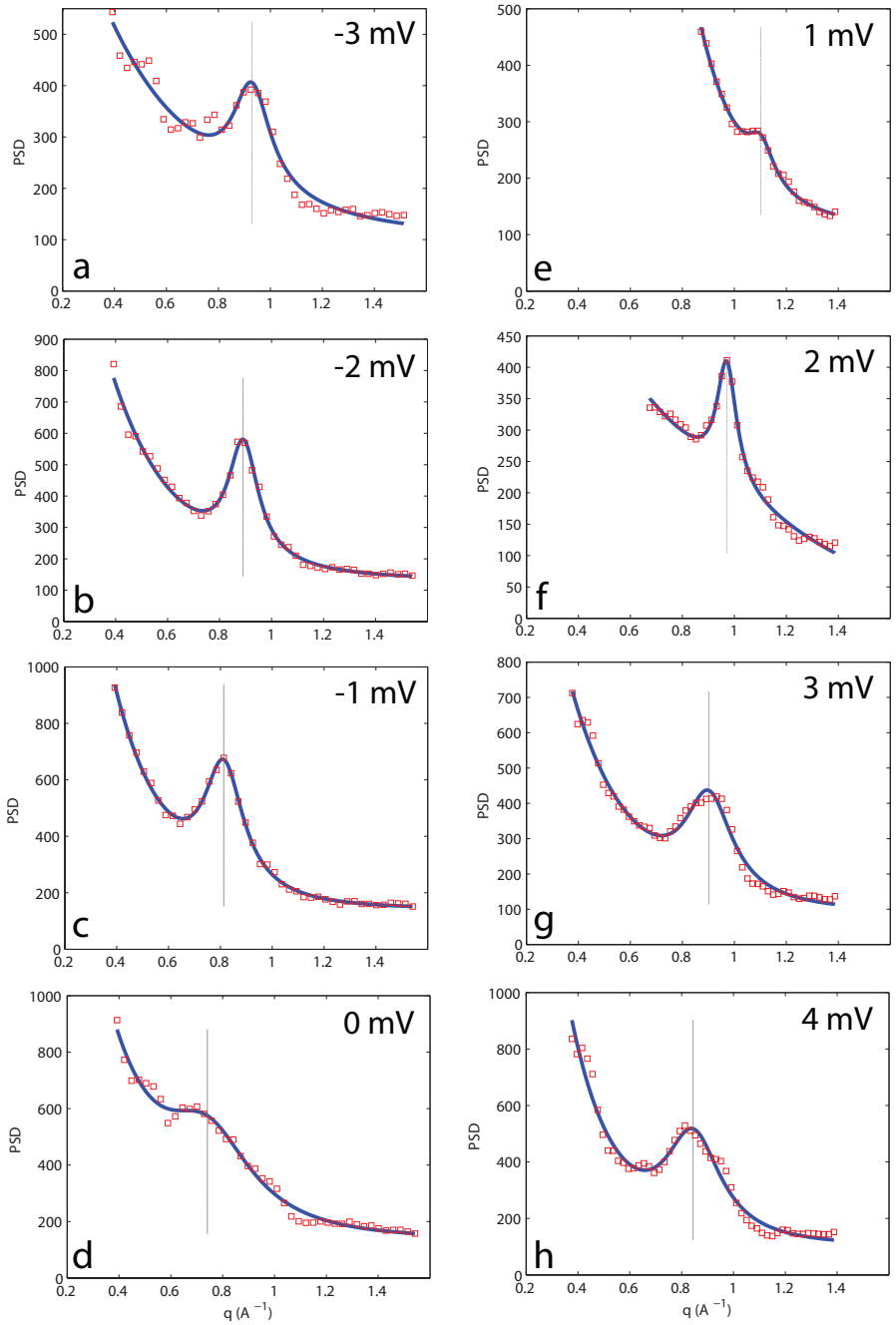

Figure E.2: Extracting QPI dispersion. The panels show a cut along the (1,1) direction of a sample of PSD layers represented in figure E.1. Each panels plots the processed PSD data (red squares) as well as a fit of an exponential background plus a Lorentizian peak (blue). The vertical line is a guide showing the extracted q value of the QPI peak. peak.

REFERENCES FOR CHAPTER 5

[1] Crommie, M. F., Lutz, C. P., and Eigler, D. M. *Nature* **363**, 524–527 June (1993).

[2] Wang, Q.-H. and Lee, D.-H. *Physical Review B* **67**(2), 020511 January (2003).

[3] Hoffman, J. E., McElroy, K., Lee, D. H., Lang, K. M., Eisaki, H., Uchida, S., and Davis, J. C. *Science* **297**, 1148–1151 (2002).

[4] McElroy, K., Simmonds, R. W., Hoffman, J. E., Lee, D.-H., Orenstein, J., Eisaki, H., Uchida, S., and Davis, J. C. *Nature* **422**, 592–596 April (2003).

[5] Hanaguri, T., Kohsaka, Y., Ono, M., Maltseva, M., Coleman, P., Yamada, I., Azuma, M., Takano, M., Ohishi, K., and Takagi, H. *Science* **323**, 923–926 February (2009).

[6] Kohsaka, Y., Taylor, C., Wahl, P., Schmidt, A., Lee, J., Fujita, K., Alldredge, J. W., McElroy, K., Lee, J., Eisaki, H., Uchida, S., Lee, D.-H., and Davis, J. C. *Nature* **454**, 1072–1078 August (2008).

[7] Wise, W. D., Chatterjee, K., Boyer, M. C., Kondo, T., Takeuchi, T., Ikuta, H., Xu, Z., Wen, J., Gu, G. D., Wang, Y., and Hudson, E. W. *Nature Physics* **5**(3), 213–216 January (2009).

[8] Lee, J., Allan, M. P., Wang, M. A., Farrell, J., Grigera, S. A., Baumberger, F., Davis, J. C., and Mackenzie, A. P. *Nature Physics* **5**, 800–804 September (2009).

[9] Figgins, J. and Morr, D. K. *arXiv:1001.3875v1* (2010).

[10] Lopez, A., Visani, P., Dalichaouch, Y., Lee, B. W., and Maple, M. B. *Physica B* **179**, 208–214 (1992).

[11] Yokoyama, M., Tenya, K., and Amitsuka, H. *Physica B* **312-313**(1-4), 498–500 March (2002).

[12] Santander-Syro, A. F., Klein, M., Boariu, F. L., Nuber, A., Lejay, P., and Reinert, F. *Nature Physics* **5**(9), 637–641 July (2009).

[13] Yoshida, R., Nakamura, Y., Fukui, M., Haga, Y., Yamamoto, E., nuki, Y., Okawa, M., Shin, S., Hirai, M., Muraoka, Y., and Yokoya, T. *Physical Review B* **82**, 205108 November (2010).

[14] Maple, M., Chen, J., Dalichaouch, Y., and Kohara, T. *Physical Review Letters* **56**, 185–188 (1986).

[15] Palstra, T., Menovsky, A., Berg, J., and Dirkmaat, A. *Physical Review Letters* **55**, 2727–2730 (1985).

[16] Coleman, P. *Heavy Fermions: electrons at the edge of magnetism*, 95–148. John Wiley (2007).

[17] Grüner, G. *Density Waves in Solids*. Perseus Publishing, (1994).

[18] Fulde, P., Keller, J., and Zwicknagl, G. *Solid State Physics* **41**, 1–151 (1988).

[19] Hewson, A. C. *The Kondo Problem to Heavy Fermion*. Cambridge University Press, (1993).

[20] Schofield, a. J. *Contemporary Physics* **40**, 95–115 March (1999).

CHAPTER 6

PERSPECTIVE ON THE 'HIDDEN' ORDER AND THE ROAD AHEAD

6.1 Essential Questions, Preliminary Answers

New perspective on both the general physics of a Kondo lattice (above T_0) and the emergence of the 'hidden' order from this state (below T_0) are revealed by SI-STM studies of URu_2Si_2. First, the Fano lattice is the spatially resolved spectroscopic image of the Kondo screening of U-atom moments for $T > T_0$. Second, the descent into the 'hidden' order state is accompanied by changes in both the real and momentum space structure. Specifically, the LDOS exhibits the opening of a soft gap and the redistribution of spectral weight within a narrow 8-10mV window about the chemical potential. In **k**-space, a light hole-like band splits into two heavy bands with an associated direct gap near $|\mathbf{q}| = 0.3(2\pi/a_0)$. Individually and as an aggregate, the observations raise several fundamental questions about the nature of the Kondo lattice, heavy fermions, and the 'hidden' order. Addressing them will be the focus of this chapter and while in most cases the answers are incomplete the conjectures provide a sharpened palette to initiate further study.

(1) Why is there no spectroscopic signature of the heavy fermion hybridization gap for $T > T_0$?

URu_2Si_2 is reported to be a coherent heavy fermion compound above T_0 [1, 2] starting at approximately 60 K. Accordingly, there should be a hybridization gap. There are a number of reasons that this gap is not observed in the SI-STM measurements as discussed in chapter 4. In the context of the Fano signature,

they included decoherence effects [3], magnetic interactions [4], strong intrinsic correlations [5], and even an absence of the Kondo effect [6]. There also exists the possibility that URu_2Si_2 is not a coherent heavy fermion for $T > T_0$ and that the observation of a Fano lattice is a representation of a matrix of U-centered incoherent Kondo many-body states. The formation of a gap below T_0 then could then be plausibly interpreted as stemming from the onset of coherence between the many-body states generating a heavy fermion, a view that is supported by momentum space measurements showing the simultaneous spawning of a new set of heavy bands. The main difficulty with an incoherent Kondo lattice is that observables such as resistivity and susceptibility [1, 2] precipitously drop below 60 K signaling developing coherence.

(2) Do the same set of states which generate the Fano lattice for $T > T_0$ also contribute to the formation of the heavy bands for $T < T_0$?

There are already two scenarios with opposite viewpoints on the matter. The first, based on the combination of proposals by Wölfle, Dubi and Balatsky [5, 7] claims that the 'Fano'like line-shape is the signature of the c-f hybridization, which would result in a hard hybridization gap but that is smeared out by intrinsic correlation effects. Such a hybridization process starts at high temperatures, around 120 K [8], and increases in strength down to approximately 20 K where the f-electrons by themselves develop some sort of heavy-mass coherent band, at least in the region of the Brillouin zone around the Γ point. At T_0, this heavy band develops an additional coherent hybridization with the conduction electrons giving rise to the observed heavy fermion bands. In this manner, there is a continuity in the set of states producing the Fano lattice and the coherent Kondo lattice band structure. Alternatively, the second scenario, proposed by

Yuan, Figgins, and Morr [9] argues that the bands generating the QPI dispersions above T_0 cannot account for the Fano signature at the same temperatures and hence its origins must reside in other electronic states not seen in the data acquired on the U terminated surface.

Consider the first proposal again: the Fano lattice represents the heavy fermion states above T_0 and its gapping the heavy fermion states below. The gapping of the bands which generate the Fano lattice reduces the effective mass from $50m_e$ to roughly $25m_e$. But most if not all of the new effective mass is accounted for in the heavy bands below T_0 and so the hidden order transition would have to completely gap out the old heavy bands and replace them with the new ones. In the present context this would then eliminate the background Fano lattice which is contrary to observation (see fig 4.5).

(3) Is the hybridization gap the 'hidden' order gap?

At first glance, the coincidental onset of the HO state and the formation of the heavy fermion bands and the relatively close energy scale of the gaps of the two would suggest that the gap associated with the phase transition is the same one as that of the band hybridization. But, both from a theoretical [10, 11, 12] and experimental [13, 14] perspective, the onset of a heavy fermion state has never been associated with a phase transition but rather with a smooth crossover as the renormalized f-level hybridizes with the Fermi sea. Moreover, since the gap in the data is not a hard gap which crosses the chemical potential its association with a second order mean field transition [2] is problematic. Nonetheless there are still some mysterious coincidences which promote the equivalence of the hybridization gap and the hidden order gap. A most notable one relates to the results from inelastic neutron scattering (INS) of Wiebe *et al.* [15] claim-

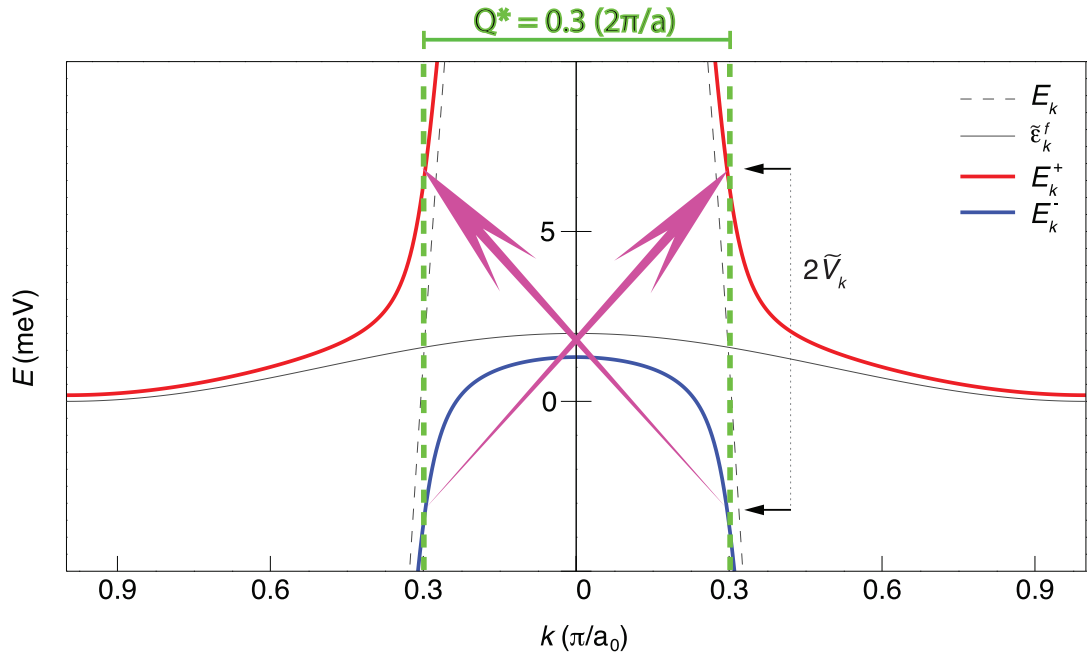

Figure 6.1: Schematic of INS measuring the hybridization gap. While INS in general measures an excitation energy and not necessarily an energy gap, the special configuration of the heavy bands shows that the INS excitation energy at $\mathbf{Q}^*$ would be equivalent to a measure of the hybridization gap.

ing that the entropy loss at the T_0 phase transition can be accounted for by the gapping of itinerant spin excitations at $\mathbf{Q}^* = 0.3(2\pi/a_0)$. The implication is that the excitation gap at $\mathbf{Q}^*$ from the reconstruction of the Fermi surface is indeed the 'hidden' order gap. Now, being a measure of excitation processes, INS cannot in general identify a gap directly. But, by considering the scenario in figure 6.1, which shows an approximate model of the bands measured by QPI (see figure 5.2d,i) and inelastic scattering process, depicted by the purple arrows, with a momentum transfer of $\mathbf{Q}^* = 0.3(2\pi/a_0)$, the INS excitation energy would be equivalent to a measure of the hybridization gap marked by the small black arrows. Hence, below T_0, the opening of the hybridization gap could also generate the spin excitation gap as reported by Wiebe *et al.*

The above observation compounds the confusion of the identity of the 'hid-

den' order gap and the hybridization gap. If the spin excitation gap observed by INS accounts for the entropy loss in the HO phase transition and derives from the configuration presented in figure 6.1 then the hybridization gap would be the 'hidden' order gap. In fact such an association is the basis for the hybridization wave theory of the 'hidden' order [7]. The origin of the phase transition is attributed to an additional translational symmetry breaking component at $|\mathbf{Q}^*| = 0.3(2\pi/a_0)$. The broken symmetry manifests itself not in a conventional density wave but a hybridization wave, modulating the hybridization strength between the conduction and f states at a wave vector of $\mathbf{Q}^*$.

There exist additional points of contact between the 'hidden' order and heavy fermion band formation. Using high resolution laser-ARPES, Yoshida *et al.* [16] tracked the evolution of the lower HO heavy band in URu_2Si_2 as a function of Rh substitution. Such alloying is known to suppress the 'hidden' order [17, 18] for even small concentrations. Their measurements found a tight relationship between the existence of the heavy band and the HO state. While such an experiment does not speak to the relation between the respective gaps it does provide further evidence that the heavy band is a signature, either direct or indirect, of the 'hidden' order transition.

Consider once again the last point raised in answering question 2 above, regarding the accounting of the effective masses above and below T_0 (or equivalently the density of states sitting at the chemical potential). As the majority of it resides in newly formed bands in the HO state, this must mean that most of the states of the Fermi surface which contributed above T_0 must have been gapped out. Hence, there is likely to be a gap that has not been observed by SI-STM, or ARPES. This could potentially be due to the nature of the measure-

ments being surface dominated while the band structure of URu_2Si_2 is known to be 3-dimensional.

6.2 Future Experiments

SI-STM has revealed a wealth of new information about fundamental heavy fermion physics and surprising microscopic signatures of the 'hidden' order. The success of the technique is motivating to push forward into the field where a probe which has access to both momentum and real space is essential. There are a number of experiments still to be conducted capable of elucidating some of the most important facets of heavy fermion physics and are expanded upon below. In the next chapter, the impurity effects of *Kondo Holes* are explored producing results which not only reaffirm the heavy fermion character of the 'hidden' order state but also unveil unexpected incommensurate modulations of the hybridization strength.

6.2.1 Universality of the Fano Lattice

There now exist theories which predict some form of Fano lattice for all coherent Kondo lattice systems [3, 4, 5], but there is so far only one instance of empirical verification. Indeed, the most basic of experiments would be to confirm the universality of the spatial spectroscopic signature found in URu_2Si_2. While there are many heavy fermion compounds, one which is suitable for STM studies, having a clean cleave plane, must be identified. Even then, the right cleave plane is necessary for in the case of URu_2Si_2 it is only the Si terminated surface

and not the U surface which exhibits the Fano spectrum.

6.2.2 Magnetic Field Dependence

STM studies of Kondo impurities systems have shown that in the presence of magnetic fields ranging from 0T - 7T, the observed resonance in the conductance spectrum splits [19]. The splitting is on the order of a few meV and agrees well with the predictions from Fermi liquid theory if interpreted as the lifting of the spin degeneracy of the local moment state. The experiment provides a definitive piece of evidence for the presence of Kondo physics. In the Kondo lattice case, the application of a magnetic field could be used as a more general test of Anderson model physics in the same way. If the Fano resonance or the QPI bands were to split then there would be a strong case for quenched moments as an active element of heavy fermion formation. Admittedly, such a signal could also arise if the Fano signature were attributed to low lying degenerate CEF states [20, 6] and further tests possibly involving temperature dependence would also need to be conducted to make a distinction.

6.2.3 Single-site Properties in U-based Heavy Fermions

As discussed in chapter 2, there are many differences between Ce-based and U-based heavy fermions. The former have a well established link to Kondo physics whereas for the latter the matter remains unresolved. Further still, the relation between Kondo lattice systems and their impurity counterparts is unexplored and would aid in understanding the extent of local physics in heavy fermions.

To this end U-doped $ThRu_2Si_2$, $U_xTh_{1-x}Ru_2Si_2$, would serve well for SI-STM studies of the Kondo impurity version of URu_2Si_2. Such a study has been undertaken for transport and thermodynamic observables [21] possibly uncovering some form of multichannel quadrupolar Kondo effect. Local spectroscopic measurements of such a phenomena would be unprecedented. Whether a Fano renonance would arise or some new signature, simply being able to distinguish such effects would be of fundamental importance. Even further, if a Kondo resonance state were to exists it would allow the opportunity to spatially image for the first time the cloud of screening electrons about each local moment [22].

6.2.4 Rh-doping

In URu_2Si_2, the substitution of Rh for Ru drastically suppresses the HO state [17, 18] and also the formation of the heavy bands below T_0 [16] for concentrations even less than 3 per cent. This means that it is not only in the vicinity of the Rh atoms that the LDOS should change but over the whole sample. However, it is not clear whether the electronic structure reassumes its form from the unordered state. Neutron scattering experiments on Rh-doped samples reveal pools of antiferromagnetic order [17, 18] directed along the c-axis and such ordering over the whole sample can be achieved with the application of pressure yielding an electronic structure very similar to that of the HO phase [23]. Thus, a great deal can be inferred about the relationship between the 'hidden' order and the heavy fermion electronic structure from $U(Ru_{1-x}Rh_x)_2Si_2$.

6.3 Concluding Remarks

The 'hidden' order state of URu_2Si_2 still remains an illusive piece of physics. But what is now quite clear from experiments is that the transition at T_0 is intimately linked to the formation of new heavy fermion bands and that most likely these are the only surviving ones since they carry the bulk of the effective mass. Furthermore, there are a confluence of several observations which render the formulation of a consistent hypothesis extremely difficult for there even remains some uncertainty about the 'normal' phase of this material. Nonetheless, the data and analysis presented thus far mark a new understanding in the low temperature phase of URu_2Si_2 and map out for the first time the evolution of a heavy fermion electronic state. In this way, URu_2Si_2 presents an almost textbook case for the study of heavy fermion properties.

REFERENCES FOR CHAPTER 6

[1] Palstra, T., Menovsky, A., Berg, J., and Dirkmaat, A. *Physical Review Letters* **55**, 2727–2730 (1985).

[2] Maple, M., Chen, J., Dalichaouch, Y., and Kohara, T. *Physical Review Letters* **56**, 185–188 (1986).

[3] Maltseva, M., Dzero, M., and Coleman, P. *Physical Review Letters* **103**(20), 206402 November (2009).

[4] Figgins, J. and Morr, D. K. *Physical Review Letters* **104**(18), 187202 May (2010).

[5] Wölfle, P., Dubi, Y., and Balatsky, A. *Physical Review Letters* **105**, 246401 December (2010).

[6] Haule, K. and Kotliar, G. *Nature Physics* **5**(11), 796–799 September (2009).

[7] Dubi, Y. and Balatsky, A. V. *arXiv:1011.5315v1* (2010).

[8] Aynajian, P., da Silva Neto, E. H., Parker, C. V., Huang, Y., Pasupathy, A., Mydosh, J., and Yazdani, A. *Proceedings of the National Academy of Sciences* **107**, 10383–10388 June (2010).

[9] Yuan, T., Figgins, J., and Morr, D. K. *arXiv:1101.2636v1* January (2011).

[10] Coleman, P. *Physical Review B* **29**(6), 3035–3044 March (1984).

[11] Evans, S., Chung, T., and Gehring, G. *Journal of Physics: Condensed Matter* **1**, 10473–10486 (1989).

[12] Schweitzer, H. and Czycholl, G. *Zeitschrift für Physik B Condensed Matter* **74**(3), 303–313 (1989).

[13] Stewart, G. *Reviews of Modern Physics* **56**, 755–787 October (1984).

[14] Stewart, G. *Reviews of Modern Physics* **73**(4), 797–855 October (2001).

[15] Wiebe, C. R., Janik, J. a., MacDougall, G. J., Luke, G. M., Garrett, J. D., Zhou, H. D., Jo, Y.-J., Balicas, L., Qiu, Y., Copley, J. R. D., Yamani, Z., and Buyers, W. J. L. *Nature Physics* **3**(2), 96–99 January (2007).

[16] Yoshida, R., Nakamura, Y., Fukui, M., Haga, Y., Yamamoto, E., nuki, Y., Okawa, M., Shin, S., Hirai, M., Muraoka, Y., and Yokoya, T. *Physical Review B* **82**, 205108 November (2010).

[17] Yokoyama, M., Amitsuka, H., Itoh, S., Kawasaki, I., Tenya, K., and Yoshizawa, H. *Journal of the Physics Society of Japan* **73**, 545–548 March (2004).

[18] Baek, S.-H., Graf, M. J., Balatsky, A. V., Bauer, E. D., Cooley, J. C., Smith, J. L., and Curro, N. J. *Physical Review B* **81**, 132404 April (2010).

[19] Otte, A. F., Ternes, M., von Bergmann, K., Loth, S., Brune, H., Lutz, C. P., Hirjibehedin, C. F., and Heinrich, A. J. *Nature Physics* **4**(11), 847–850 September (2008).

[20] Cox, D. *Physical Review Letters* **59**, 1240–1243 (1987).

[21] Amitsuka, H. and Sakakibara, T. *Journal of the Physics Society of Japan* **63**, 736–747 February (1994).

[22] Affleck, I., Borda, L., and Saleur, H. *Physical Review B* **77**(18), 180404 May (2008).

[23] Hassinger, E., Knebel, G., Matsuda, T., Aoki, D., Taufour, V., and Flouquet, J. *Physical Review Letters* **105**, 216409 November (2010).

CHAPTER 7

KONDO HOLES - ABSENT MOMENTS

7.1 Introduction

The experiments described so far have led to a direct visualization of the alterations to the electronic structure of URu_2Si_2 that are brought upon by the development of heavy fermions: a soft gap opens in the density of states, there is a redistribution of spectral weight close to the chemical potential, and most dramatically a light band is observed to split into two highly distinct heavy bands within an avoided-crossing energy range often referred to as the 'hybridization gap', $\Delta_h \propto 2V_h$, where V_h is the hybridization matrix element coupling the c and f electrons. And while the onset of such changes is coincident with the HO transition, there is abundant evidence that URu_2Si_2 is a simple heavy fermion at low temperatures. Based on specific heat measurements, the enhanced Sommerfeld coefficient implies an effective mass of roughly $25m_e$ [1] with thorium dilution contributing only a mild diminishment [2]. An equivalently augmented mass has also been inferred from calculations of carrier damping in Hall transport data [3]. Alternatively, effective masses determined by cyclotron frequencies in quantum oscillation experiments [4, 5] probing various branches of the Fermi surface give values as high as $30m_e$. From a spectroscopic viewpoint, ARPES has established the presence of a slowly dispersing quasiparticle band of f character sitting just below the chemical potential [6, 7], a strong signature of heavy bands. Collectively and in conjunction with the discoveries presented thus far in this dissertation, all of the observations definitively demonstrate the archetypical heavy fermion character of URu_2Si_2 at low temperatures.

Exploration of heavy fermion physics has inevitably led to the introduction of defects which either directly distort the array of magnetic moments or which perturb the band of light electrons. Surprisingly, over the last 35 years there has been very little systematic work done in understanding the effect of impurities on the Kondo lattice, both from an experimental and theoretical perspective. Experiments have mainly focused on macroscopic effects with some preliminary speculation regarding the microscopics and only recently have more sophisticated computational method been implemented to describe the local real-space electronic structure alternations induced by defects. The range of unexplained phenomena not only relates to the fundamental properties of the heavy fermion state but also the unconventional superconductivity and non-fermi liquid like behavior which it spawns. Thus, a clear understanding of how the Kondo lattice responds to impurities would shed light on several outstanding problems in correlated electron physics.

7.2 Kondo Holes

Local moments constitute the backbone of the physics in a coherent Kondo lattice and their removal in small quantities provides a fundamental form of defect known as a 'Kondo-hole'. They arise when a single non-magnetic atom is substituted within the array of otherwise magnetic f-electron atoms (figure 7.1). Typically La replaces Ce and Th substitutes for U in the respective rare-earth and actinide Kondo lattice materials. Although there is excellent experimental understanding of the electronic properties at the corresponding dual structure, the Kondo resonance in magnetic impurity systems [8, 9, 10, 11, 12], the atomic-scale electronic phenomena surrounding Kondo-holes have remained completely un-

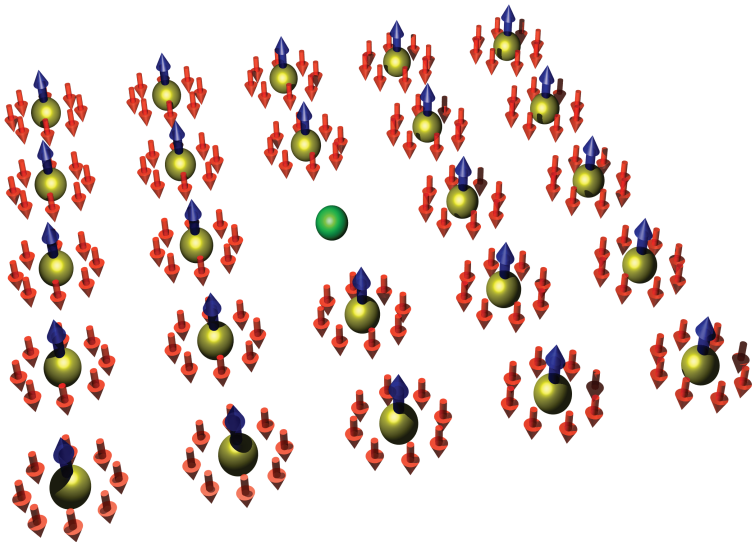

Figure 7.1: Kondo hole. The removal of a magnetic moment (blue) from the Kondo lattice of screened moments, produces a Kondo hole (green). The effective hybridization of the conduction electrons and the f-electrons at such a position is altered breaking the translational symmetry of the system.

explored.

7.2.1 Macroscopic Effects

Understanding the electronic structure of a Kondo-hole could be of great fundamental and practical consequence to the study and application of rare-earth and actinide metals. This is because key experiments designed to study heavy-fermion physics in these systems have long explored the macroscopic effects of random substitution of spinless atoms for magnetic atoms [13, 2, 14, 15, 16, 17, 18]. For example, when non-magnetic La is substituted for magnetic Ce atoms in $CePd_3$ an upturn in resistivity is observed at low temperatures and has been postulated to arise from the presence of a resonance within the heavy fermion

pseudogap with a Kondo-like contribution to the specific heat and magnetic susceptibility [16]. A very similar resistivity minimum in Th-doped URu_2Si_2, has similarly been interpreted as a change in the Kondo binding energy which effectively couples the local moments to the conduction sea [2]. The disruption of the Kondo lattice by Kondo holes has also been shown in $CeCoIn_5$ to suppress superconductivity and alter non-Fermi liquid like properties [17, 18] implying a very intimate connection in between the unconventional ground states and the heavy fermion state. So, while the macroscopic effects of Kondo hole doping are evident, without a knowledge of the alternations to the electronic structure their origins are still speculative. The long term experimental challenge has therefore been to visualize (i) alterations to the Kondo interaction strength, (ii) the formation of in-gap states, and (iii) the extent of the deformation of the heavy fermion lattice at an individual Kondo hole.

7.2.2 Preliminary Theoretical Understanding

The impact of Kondo-holes on both the local many-body electronic structure and the hybridization process generating the heavy fermions, has been studied theoretically for the last 25 years. Predictions include that: (i) the hybridization and its related effects in the density of states $N(\epsilon)$ will be progressively degraded by increasing densities of Kondo-holes [19, 20, 21] eventually destroying the heavy fermion state, (ii) a unique bound impurity state should exist within the reduced hybridization gap at each Kondo-hole site [20, 21, 22] (iii) the electrical resistivity should exhibit a minimum and then increase with falling T at low temperature [19, 23], and (iv) in non s-wave HF superconductors, the superconductivity should be strongly suppressed by pair breaking scattering at each

Kondo-hole [24]. Contemporary theoretical analysis [22] describes atomic-scale variations at a Kondo-hole in the hybridization strength V_h, the density of states $N(\epsilon)$ and the antiferromagnetic correlation. Additionally, the presence of an impurity bound-state whose spectroscopic signature is a sharp peak in inside the hybridization gap also follows from the numerical studies. Figure 7.2a shows the numerical evaluation of the perturbations to the hybridization strength, V_h, surrounding a Kondo-hole. The key observation is that V_h oscillates spatially with wavevector $\mathbf{Q}^* \approx 2\mathbf{k}_F^c$ where $\mathbf{k}_F^c$ is the Fermi wavevector of the original light (un-hybridized) conduction band, as illustrated in figure 7.2b [22]. Such hybridization oscillations would be highly distinct from the Fermi-level Friedel oscillations which have been observed at $\mathbf{q}(\epsilon = 0) = 2\mathbf{k}_F^{HF}$ where $\mathbf{k}_F^{HF}$ is the Fermi wavevector of the heavy fermion band (figure 7.3, 5.1, and5.2). Since the hybridization matrix element, V, also sets the range of the hybridization gap Δ_h [25, 26], as depicted in figure 7.3, a measure of the spatial structure of the gap would give direct information about the strength of c-f interactions. A measurement of this kind has not been possible until now.

7.2.3 Theory for the Local Effects of Kondo Holes

An analytical theory for understanding the expected electronic structure at an individual Kondo hole has been formulated by Dubi and Balatsky. As the theory has not yet been published at the time of the writing of this dissertation, it is referenced here by permission.

The correction to the gap around the impurity is altered by the coherence between the c and f electrons induced by the presence of the impurity Kondo

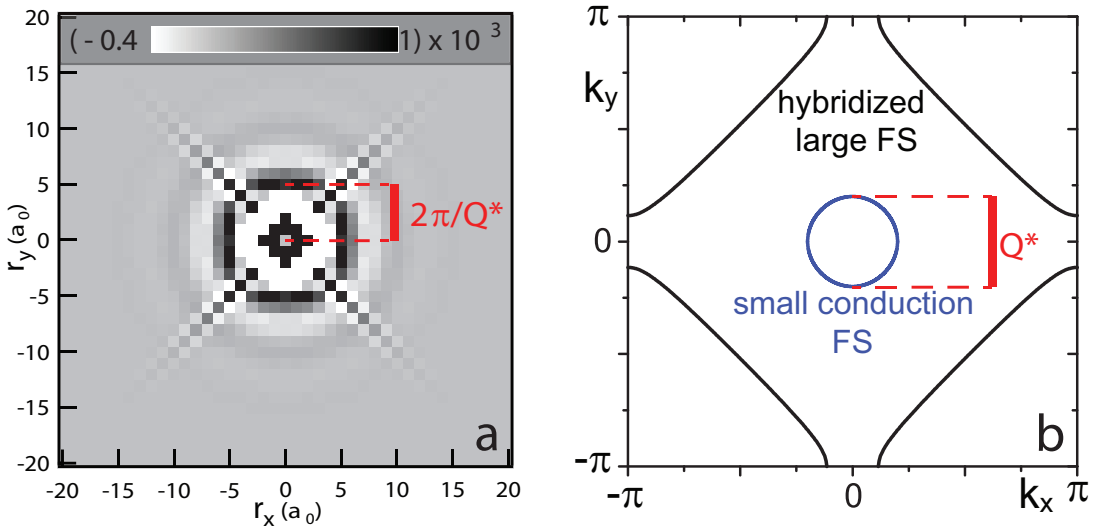

Figure 7.2: Numerical simulation of modulations to c-f hybridization strength due to a Kondo hole. **a**, Real-space modulations to the hybridization strength centered around a Kondo hole at position (0,0). The wavelength of the oscillations is set by the wavevector $\mathbf{Q}^*$. **b**, Fermi surface for an electron-like band showing both the unhybridized light band in blue and the fully hybridized band in black. The diameter of the sheet for the light band is $|\mathbf{Q}^*|$, and directly sets the scale for the hybridization oscillation wavelength [22].

hole. So near the chemical potential an incoming quasiparticle with dominant f character with momentum k is scattered into a c-electron with momentum k' of the same energy. A double sum over the momenta accounts for all possible scattering processes in the Brillouin zone. However, certain scattering events have a higher weight and these are the ones in which $k \approx k'$ and $\epsilon_f \approx \epsilon_{\mathbf{k}}$, the energies of the f level and the conduction band. Thus, this sets up the conditions for the dominant oscillation wavevector Q^* by solving $\epsilon_f \approx \epsilon_{\mathbf{k}'}$.

The above argument can be made analytically as follows. The effect of a Kondo hole is evaluated through its effect on the self-consistent solution of the

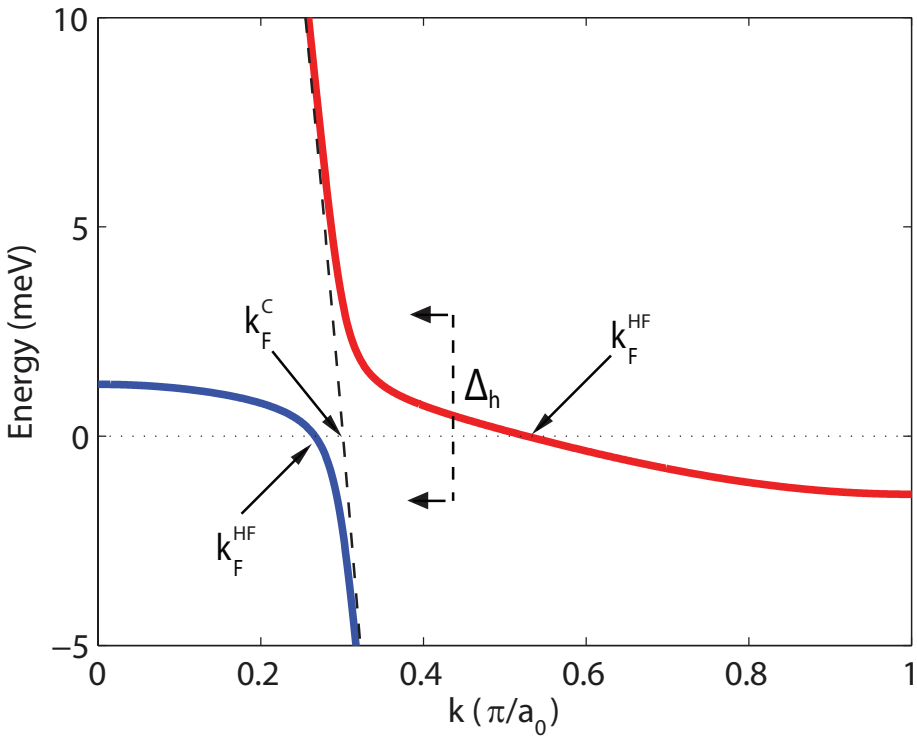

Figure 7.3: Heavy Fermion band structure showing essential Fermi wavevectors, $\mathbf{k}_F$. The original unhybridized light band, shown as a dashed line, crosses the chemical potential at $\mathbf{k}_F^C$. The heavy bands, shown in red and blue, cross the chemical potential at $\mathbf{k}_F^{HF}$. The hybridization gap is labelled as Δ_h and is defined by the energies of the heavy bands which correspond to the wavevector $\mathbf{k}_F^C$.

mean field Anderson model. Starting with the Hamiltonian

$$\begin{aligned} H &= H_0 + H_{int} \\ H_0 &= \sum_{\mathbf{k},\sigma} \epsilon_{\mathbf{k}} c^\dagger_{\mathbf{k}} c_{\mathbf{k}} + \epsilon_f \sum_i f^\dagger_{\mathbf{r}_i} f_{\mathbf{r}_i} \\ H_{int} &= U \sum_i c^\dagger_{\mathbf{r}_i} c_{\mathbf{r}_i} f^\dagger_{\mathbf{r}_i} f_{\mathbf{r}_i} \end{aligned} \tag{7.1}$$

the full interaction between the holes and localized f-electrons mediated by H_{int} is decomposed into a mean field interaction. The resulting mean-field hybridization term

$$H_h = V_h \sum_i c^\dagger_{\mathbf{r}_i} f_{\mathbf{r}_i} + \text{h.c.} \tag{7.2}$$

must be determined self-consistently through the mean-field equation for V_h

which is assumed to be $\mathbf{r}_i$ independent because of translational invariance

$$V_h = \frac{U}{2}\langle f^\dagger_{\mathbf{r}_i} c_{\mathbf{r}_i}\rangle \, . \tag{7.3}$$

Diagonalization of equation 7.2 constrained by the self-consistency condition yields a solution for V_h

$$V_h = \frac{e^{\frac{1}{4U\rho_0}}\sqrt{W_1 + e^{\frac{1}{2U\rho_0}}\left(W_2 - \epsilon_f\right) + \epsilon_f}\sqrt{W_2 - \epsilon_f + e^{\frac{1}{2U\rho_0}}\left(W_1 + \epsilon_f\right)}}{-1 + e^{\frac{1}{U\rho_0}}} \, . \tag{7.4}$$

Within the mean field solution of the total Hamiltonian, V_h assumes its usual definition in the energy bands

$$E^{\pm} = \frac{1}{2}(\epsilon_{\mathbf{k}} + \epsilon_f) \pm \sqrt{\left(\frac{\epsilon_{\mathbf{k}} - \epsilon_f}{2}\right)^2 + V_h^2} \tag{7.5}$$

and defines a gap between the upper and lower band.

The next step is to evaluate the effect of a single Kondo hole on the self-consistent solution of V_h. For that the Nambu Green's functions formalism is used and the associated mean-field equation takes the form

$$V_h(r) = -iU \int F(r, r, \epsilon) d\epsilon \tag{7.6}$$

where $F(r, r, \epsilon)$ is the off-diagonal Green's function and will in turn depend on V_h. Thus, equation 7.6 defines another self-consistency condition. Assuming that the both F and V_h can be written in terms of a spatially uniform part and another with small amplitude variations, $F = F_0 + \delta F(r)$ and $V_h = V_0 + \delta V(r)$, with V_0 given by equation 7.4, the correction to the hybridization potential is

$$\delta V(r) = -iU \int \delta F(r, r, \epsilon; V_0) d\epsilon \, . \tag{7.7}$$

The bare Green's function from the mean-field Hamiltonian with no impurity, can be written as

$$\hat{G}_0 = \begin{bmatrix} G_{0,c}(k,\epsilon) & F_0(k,\epsilon) \\ F_0^*(k,\epsilon) & G_{0,f}(k,\epsilon) \end{bmatrix} \tag{7.8}$$

where

$$\begin{aligned} G_{0,c}(k,\epsilon) &= \frac{\epsilon - \epsilon_f}{(\epsilon - \epsilon_{\mathbf{k}})(\epsilon - \epsilon_f) - V_0^2} \\ G_{0,f}(k,\epsilon) &= \frac{\epsilon - \epsilon_{\mathbf{k}}}{(\epsilon - \epsilon_{\mathbf{k}})(\epsilon - \epsilon_f) - V_0^2} \\ F_0(k,\epsilon) &= \frac{V_0}{(\epsilon - \epsilon_{\mathbf{k}})(\epsilon - \epsilon_f) - V_0^2} \ . \end{aligned} \tag{7.9}$$

To assess the effect of the Kondo hole potential, the focus will be on the modifications to the hybridization that the impurity generates through additional scattering between the Fermi sea and the f-electrons. For a potential that is localized in space, the impurity Hamiltonian can be expressed as

$$H_{imp} = V_{imp}(c_{r=0}^\dagger f_{r=0} + f_{r=0}^\dagger c_{r=0}) \ . \tag{7.10}$$

Then, the lowest order correction to the Green's function is

$$\hat{G}_1(k,k',\epsilon) \approx V_{imp}\hat{G}_0(k,\epsilon)\cdot\tau_1\cdot\hat{G}_0(k,\epsilon) \tag{7.11}$$

where τ_1 is the first Pauli matrix. The position dependence of the correction to the anomalous part of the Green's function $\delta F(r,\epsilon)$, which also generates the position dependence for V_h, can now be written in terms of the bare Green's function

$$\delta F(r,\epsilon) \approx V_{imp}\int dk dk' \mathrm{e}^{i(k-k')r}(G_{0,c}(k,\epsilon)G_{0,f}(k',\epsilon) + F_0(k',\epsilon)F_0(k,\epsilon)) \ . \tag{7.12}$$

Changing the integration variable to energy with the inverted dispersion $k^c(\epsilon)$,

$$\delta F(r,\epsilon) \approx V_{imp}N_0^2\int d\epsilon' d\epsilon'' \mathrm{e}^{i(k^c(\epsilon')-k^c(\epsilon''))r}\frac{(\epsilon-\epsilon')(\epsilon-\epsilon_f)+V_0^2}{\left[(\epsilon-\epsilon'')(\epsilon-\epsilon_f)-V_0^2\right]\left[(\epsilon-\epsilon')(\epsilon-\epsilon_f)-V_0^2\right]} \tag{7.13}$$

with N_0 the density of states at the Fermi level, and $k^c(\epsilon)$ describing the inverse dispersion of the original conduction electrons. The difference between the Green's function for the conduction and f electrons is manifest in the asymmetry between ϵ' and ϵ'' in the equation above.

The integrand in equation 7.13 has two poles

$$\epsilon' \, , \, \epsilon'' = \epsilon_p = \epsilon - \frac{V_0^2}{\epsilon - \epsilon_f} \tag{7.14}$$

which dominate the integral leading to the approximation

$$\delta F(r, \epsilon) = \exp\left(2ik^c(\epsilon_p(\epsilon))r\right) = \exp\left[2ik^c\left(\epsilon - \frac{V_0^2}{\epsilon - \epsilon_f}\right)r\right] \, . \tag{7.15}$$

At this point the spatial modulations to the correction term are energy dependent. However, since the strongest modulations derive from where $k \approx k'$ and $\epsilon_f \approx \epsilon_{\mathbf{k}}$ the main regions of interest are the edges of the direct gap as they satisfy the two conditions. In equation 7.5, the gap edges correspond to the energies $\epsilon = \Delta_h^{\pm} = \epsilon_f \pm V_0$ leading a specific value for the argument of k^c

$$\begin{aligned} \epsilon - \frac{V_0^2}{\epsilon - \epsilon_f}\bigg|_{\epsilon=\Delta_h^{\pm}} &= \epsilon_f \pm V_0 - \frac{V_0^2}{(\epsilon_f \pm V_0) - \epsilon_f} \\ &= \epsilon_f \pm V_0 \mp V_0 \\ &= \epsilon_f \, . \end{aligned} \tag{7.16}$$

Finally, the period of oscillation of $\delta F(r, \epsilon)$ at the direct gap edge can be expressed as

$$\delta F(r, \Delta_h^{\pm}) \sim \exp(2ik^c(\epsilon_f)r) \, . \tag{7.17}$$

Since $k^c(\epsilon)$ describes the inverse dispersion of the original conduction electrons, its evaluation at ϵ_f corresponds to the wavevector, Q^*, of the avoided crossing in between the f and conduction bands. As a consequence of the relationship

between F and V_h through equation 7.6, the correction to the hybridization is also found to exhibit the same characteristic modulation wavevector. Hence, the presence of a Kondo hole generates ripples in the strength of c-f interactions with a wavelength that is very close to the Fermi wavevector of the unhybridized conduction band. To reemphasize, the oscillation wavevector Q^* lies within the range of avoided momentum values in the fully hybridized electronic structure demonstrating the effect of locally broken composite heavy quasiparticles.

7.3 SI-STM Visualization of Kondo Holes

The heavy fermion state of URu_2Si_2 at low temperatures makes its 1% Th-doped alloy, $U_{0.99}Th_{0.01}Ru_2Si_2$, an ideal case to visualize the electronic structure of a Kondo hole resulting from the absent f-electron in the dopant Th atoms. Figure 7.4a shows a topographic image of the Uranium-termination surface of $U_{0.99}Th_{0.01}Ru_2Si_2$. The site of each Th atom corresponds to an atomic-scale dark spot, whose density is in good agreement with the known Th atom density. The remaining panels in the figure show the conductance $g(\epsilon)$ measured under three different conditions. Panel 7.4b plots the spatial average of $g(\epsilon)$ away from Th sites measured above 16 K where the heavy fermion bands are not detected (see chapter 5). Panel 7.4c shows the same spatial average measured at 1.9 K away from Th sites; there are clear changes in the $N(\epsilon)$ which are produced by the appearance of the coherent heavy fermion band structure and the empirical definition of $\Delta_h^{\pm}$ is in terms of the points where $N(\epsilon)$ departs from its smooth high-temperature values (indicated by vertical arrows). The final panel, 7.4d, plots $g(\epsilon)$ averaged over several representative Th sites measured at 1.9 K. At these lo-

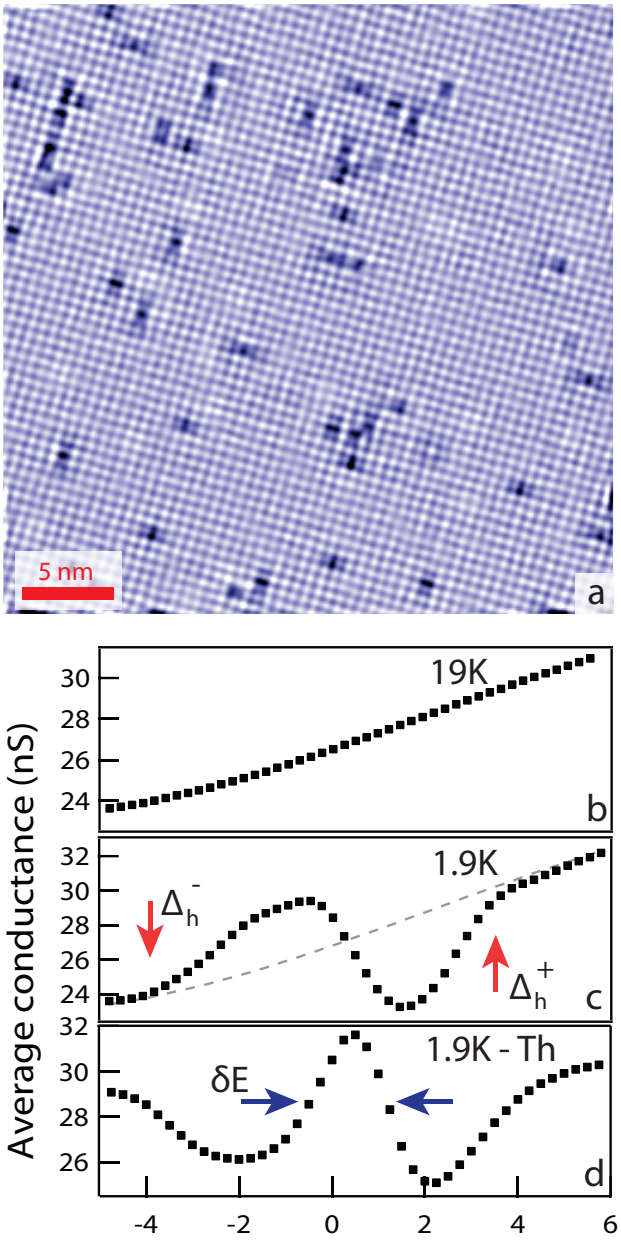

Figure 7.4: Identifying the effect of Kondo holes. **a**, Topograph of U-terminated surface showing atomic corrugation and black spots which are believed to be the substituted Th atoms. The dopants appear both in clusters and singly. **b**, The tunneling density of states $N(\epsilon)$ measured at $T \approx 19$ K just above T_0. **c**, The tunneling density of states $N(\epsilon)$ measured at $T \approx 2$ K after the heavy fermion bands have become established (see chapter 5). The magnitude of the hybridization gap Δ_h can be determined by identification of the energy range where $N(\epsilon)$ deviates from the 19 K data due to the HF band structure as shown by the vertical arrows. **d**, The tunneling density of states $N(\epsilon)$ averaged over several representative Th atom sites at $T \approx 2$ K. The sharp feature which sits just off of the chemical potential has a width of approximately 1 mV.

cations the hybridization gap is reduced from the average (see appendix F) and a sharp ($\delta E \approx 1$ meV) peak in $N(\epsilon \approx 0)$ forms. This is the long-sought electronic impurity bound-state at a Kondo hole [19, 20, 21, 24, 22] (see also appendix H).

The local hybridization strength in **r**-space can be determined using the range of energies between Δ_h^+ and Δ_h^- for which $g(\mathbf{r}, \epsilon)$ is distinct (figure 7.4c) from the featureless trace observed at high temperatures (figure 7.4b). The visualization of the spatial variations of the empirically defined measure of the hybridization, Δ_h, requires defining the concept of a *hybridization gap map* for heavy fermion compounds. The result for a 40nm×40nm U-termination field of view is shown in figure 7.5a. Surprisingly, the hybridization strength varies over approximately 5 mV within distances of only a few nanometers, in what appears to be a highly disordered spatial arrangement. However, this discovery is precisely what has long been predicted for Kondo-hole doped heavy fermion systems [19, 20, 21, 24].

Fourier analysis of the hybridization gap map reveals the second exciting discovery, that the complex fluctuations in $\Delta_h(\mathbf{r})$ originate predominantly from a simple harmonic structure. The power spectral density (PSD), $\Delta_h(\mathbf{q})$ of $\Delta_h(\mathbf{r})$ in figure 7.5a is shown in figure 7.5b (see appendix for processing algorithm). The image captures vividly that the hybridization strength modulates in real space with a characteristic wave vector $\mathbf{Q}^*$, as identified by the bright ring. The inset along the (1,0) direction demonstrates the high S/N ratio of the periodic structure of hybridization oscillations. Within the errors of the measurements (shown in figure 7.6), the observation is in excellent accord with the theoretical predictions from figure 7.2a and equation 7.2.3 demonstrating that the hybridization modulations originate from the presence of a local Kondo hole and

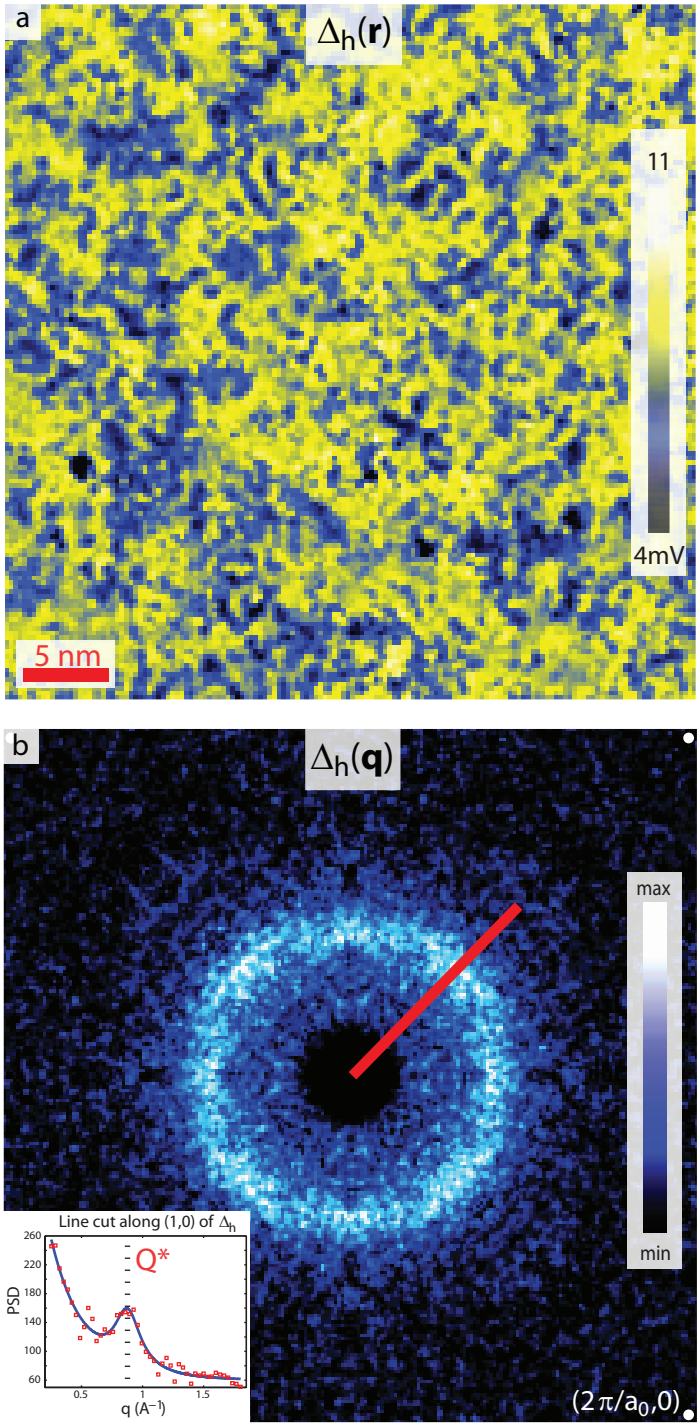

Figure 7.5: Hybridization gap map. **a**, Real space visualization of the hybridization oscillations Δ_h induced by Kondo holes. **b** Fourier transform of $\Delta_h(\mathbf{r})$ revealing the dominant modulation wavevector $\mathbf{Q}^*$ of the hybridization oscillation induced by Kondo holes. The inset plots the line cut (in red) through the bright blue ring showing the prominent intensity at the wavevector $\mathbf{Q}^*$. For scale, the Bragg peaks are shown as white spots in the corners of the image.

furthermore that the wavelength is set by the wavevector $\mathbf{Q}^*$ associated with the avoided crossing in between the conduction band and the renormalized f-level. To illustrate the point more concretely, figure 7.6a and b plot the URu_2Si_2 heavy fermion band structure, determined using quasiparticle interference imaging, along with and associated changes in the density of states $N(\epsilon)$ from 19 K (see chapter 5). Both panels have the same vertical energy axes and hence a direct comparison of features is presented between the momentum space and real space observations. In figure 7.6a there are a number of crucial observations. First, within uncertainty, only the light band is observed to occupy those states at $\mathbf{Q}^*$ near the chemical potential, labelled by $2\mathbf{k}_F^C$. Second, the heavy bands at low temperatures cross the Fermi level at $\mathbf{q} = 2\mathbf{k}_F^{HF}$ and hence the low temperature $\mathbf{Q}^*$ modulated hybridization oscillations are fundamentally distinct from a standard Friedel-type response.

The final observation makes the crucial connection between the empirically defined hybridization gap and the hybridization gap arising from the momentum space structure: by extending the lines marking the location of the gap edges Δ_h^+ and Δ_h^- from figure 7.6b (dashed lines) onto the dispersion bands in panel a, it is strongly indicative, within the measurement error, that the hybridization gap energy range defined in real space coincides with the energy range of avoided crossings in the band structure. The importance of the connection rests in having found a consistent definition of the hybridization energy scale and that the observed modulations in real space are reflective of a fundamental energy scale in heavy fermion physics.

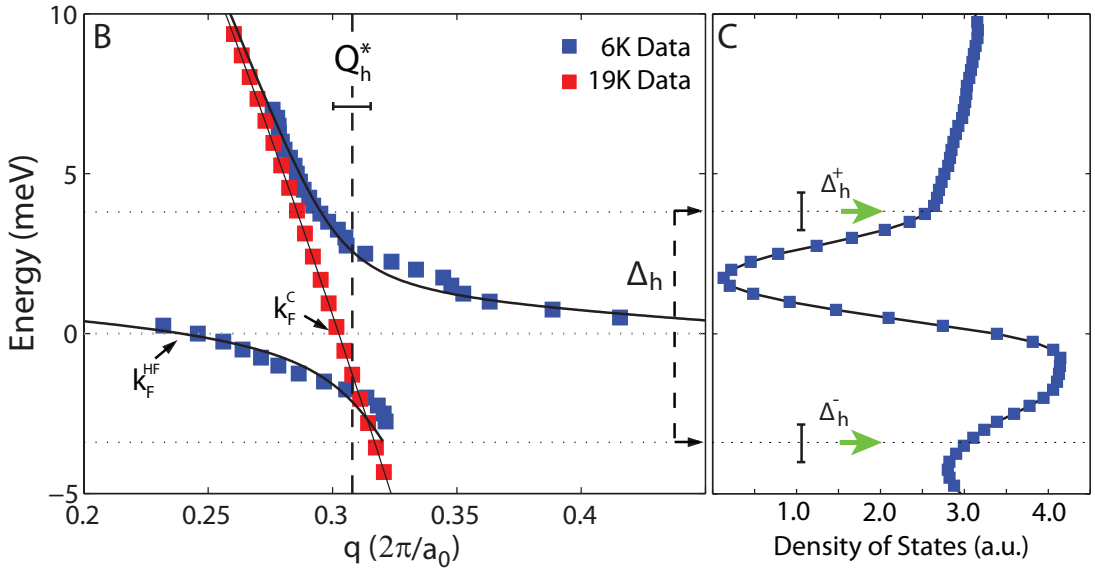

Figure 7.6: The hybridization gap in the DOS and momentum space electronic structure. **a**, QPI peak dispersion data for 19 K (red squares)and 6 K (blue squares) showing the formation of two new heavy bands at low temperatures. The solid black lines are guides tracing the dispersion of the data. The original light band seen at 19 K crosses the chemical potential at $2\mathbf{k}_F^C = \mathbf{Q}^* = 0.305 \pm 0.015(2\pi/a_0)$. At 6 K, the heavy bands are observed to cross at some other $\mathbf{q} = 2\mathbf{k}_F^{HF}$. The range demarcating the hybridization gap, labelled by Δ_h, is determined from the real space DOS as labelled in **b** panel. **b**, 2 K DOS of states with 19 K background subtracted revealing the empirically determined hybridization gap edges, Δ_h^+ and Δ_h^- (green arrows). The precision in determining the gap edges is shown by the error bars of length 1.2 mV.

7.4 Discussion and Conclusions

The atomic-scale electronic structure of a Kondo hole directly confirms two main predictions. First, the suppression of the hybridization strength at the substitution site [19, 20] and the resulting induced hybridization oscillations at $\mathbf{Q}^* \approx 2\mathbf{k}_F^C$ ([22] and equation 7.2.3). Second, the formation of an impurity bound-state observed at each Kondo hole (figure 7.4d and appendix H).

There is a considerable amount of insight that is gained about heavy fermions from the new discoveries. While at first it may seem puzzling that the

hybridization oscillations modulate at a wavevector that is avoided at the Fermi level, the result actually is a demonstration of the composite nature of the heavy quasiparticles. At a Kondo hole, where the f-level is locally removed, there is in effect an enhancement of *spd* spectral weight coming from the light band involved in the hybridization. The compensation effect of the system, similar to the Friedel response, produces ripples in the hybridization strength at the only present **q**-vector which was supported before hybridization. Considered another way, the system can only respond at the sole wavevector available which can modulate the relative coupling of the distinct *spd* and f electrons in order to maintain a coherent heavy fermion state in the rest of the system.

Furthermore, while still not clear from the present analysis, if the observed bound-state at each Kondo hole were doubly degenerate, it would provide a microscopic source for the higher order scattering process needed to produce the resistivity minimum similar to that in Kondo metals [25] but now in dilute Kondo hole system. Such upturns in resistivity have been observed for Th-doped URu_2Si_2 [2], La-doped $CePd_3$ [16, 28], La-doped $CeOs_4Sb_12$ [29] and have generated much speculation regarding the effects Kondo holes. It is now becoming possible to develop a microscopic understanding using SI-STM techniques.

Direct determination of the Kondo-hole electronic structure in different materials using SI-STM techniques would allow for a number of outstanding problems to be readdressed in detail. Beyond the fundamentals of heavy fermion physics itself, the nature of non-Fermi liquid behavior in heavy fermion materials stands as one broad example [17]. In connection with unconventional superconductivity, Kondo holes provide a channel to explore the pairing sym-

metry that would arise from a heavy state and how the coherence of the Kondo lattice itself influences the superfluid state [18]. More concretely, and already within reach, hybridization oscillations provide a window into extracting the contributions of interactions such as superexchange and RKKY leading to the heavy fermion coherent state [22]. This would be accompanied by a more exact understanding of the degree of coherence of the heavy quasiparticles based on how strongly the hybridization gap is washed away or over what spatial length scales the hybridization oscillations persist.

APPENDIX FOR CHAPTER 7 F

HYBRIDIZATION GAP MAP WITH MARKED TH-ATOMS

The breaking of the translational symmetry imposed by the Th atoms modulates the *c-f* hybridization strength. In addition, the local value of the hybridization strength is suppressed at the Th sites. Figure F.1 shows the same hybridization gap map as in figure 7.5a but with the Th sites in the given field of view marked in red. The red marks predominantly occupy locations of darker color, corresponding to a lower value of the hybridization gap. Averaged over all pixels associated with the Th sites, the value of the gap is 0.5 mV lower than the average over the rest of the map. However, there are additional dark regions in the map which do not correspond to the location of Th atoms. These may be due to sub-surface Th atoms which are not visualized. To ensure that the suppression of the gap value on the set of points marked in red cannot be replicated by a random selection of sites, randomly selected points were generated and their gap values evaluated and averaged. Over several thousand trials, it was found that a random distribution of points equal in number to the Th marked sites would not yield a reduced average gap value as that observed in the data. The average spectra over the Th atoms is presented in figure 7.4d.

A change of 0.5 mV in the hybridization strength is approximately 7% of average value and admittedly lies just within the error estimate of 0.6 mV of the average, determined from the standard deviation of $\Delta_h(\mathbf{r})$. Furthermore, the definition of the hybridization gap at the Th sites is slightly more ambiguous as demonstrated by the spectra in appendix H. There, the deviations from the high temperature data are not as sharply defined as they are for the average spectra (see figure 7.4b and c). However, the same algorithm (see appendix G) detects

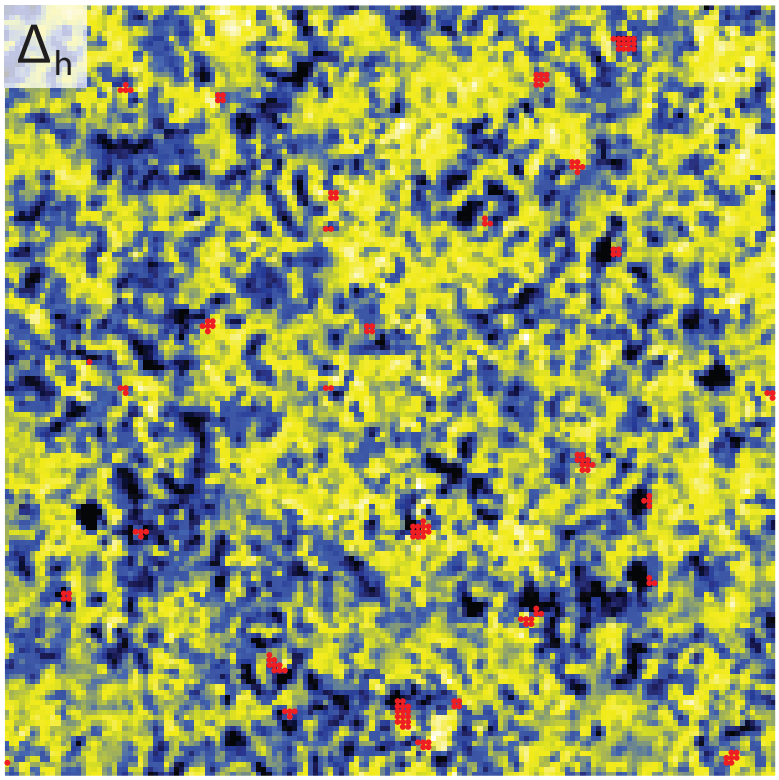

Figure F.1: Hybridization gap map, $\Delta_h(\mathbf{r})$, with marked Th sites. The red marks correspond to the position of Th sites as determined from the topograph of the same field of view. Typically, the Th sites correspond to the darker lower valued regions.

a shift in the inflection points near the edges of both the on-site and off-site spectra. It is based on this scheme a small shift is seen in the gap width.

APPENDIX FOR CHAPTER 7 G

HYBRIDIZATION GAP MAP ALGORITHM

The hybridization gap in URu_2Si_2 is derived from STM spectroscopic measurements mapping the local value of the conductance in a 40nm×40nm field of view (FOV) discretized across 200×200 pixels. As variations in the scale associated with the hybridization gap are small, high energy resolution is required, with the current data having an energy spacing of 250μV.

The hybridization gap is determined by finding the energies for which the low temperature conductance curve begins to deviate from the high temperature data, where there are no observed heavy fermion bands. Figure G.1 shows the average spectrum from the data with the deviations from the 19K marked by arrows. These points identify the edges of the hybridization gap Δ_h^+ and Δ_h^-. The algorithm to extract quantitatively the energy position for the whole set of spectra (40 000 in total) involves fitting the interval around the Δ_h^+ and Δ_h^- with a low order polynomial, shown in red in figure G.1, and then extracting the inflection point. This generates the maps $\Delta_h^+(\mathbf{r})$ and $\Delta_h^-(\mathbf{r})$ for which the dominant modulation wavevectors can be seen by taking the PSD density as presented in figure G.2. To increase the S/N, the PSD has been symmetrized. Furthermore, the center mass, representative of disorder effects, has been removed to enhance the color contrast at the higher wavevectors.

As demonstrated in the PSD plots of figure G.2, each gap edge also modulates with $\mathbf{q} = \mathbf{Q}^* \approx 0.3(2\pi/a_0)$ but with the dominant modulation wave vectors rotated by 45 degrees with respect to one another. It is also found that $\Delta_h^-(\mathbf{r})$ modulates more strongly than $\Delta_h^+(\mathbf{r})$ and thus to make the full ring of wavevectors visible in the PSD for the full gap, $\Delta_h(\mathbf{q})$ (see figure 7.5b), the right PSD

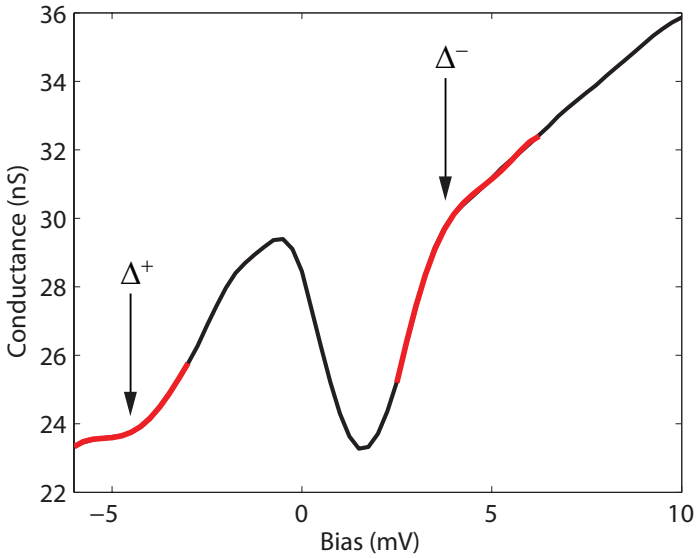

Figure G.1: Identifying the Δ_h^+ and Δ_h^-. The black vertical arrows mark where the low T data begins to vary from the high T data, where the heavy bands are not observed. The red portions represent fits to low order polynomials whose inflection points define the gap edges.

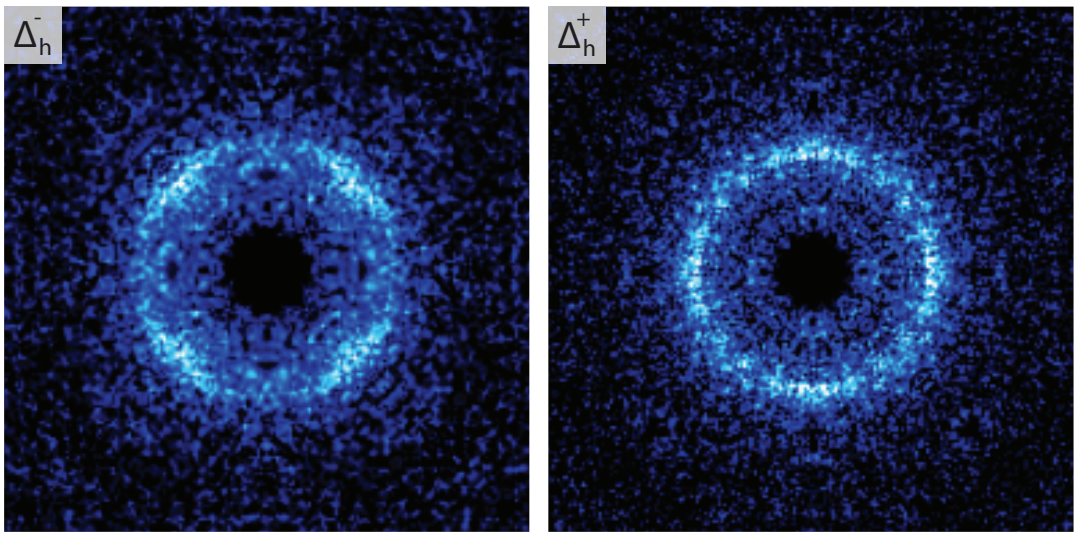

Figure G.2: Power spectral density of Δ_h^+ and Δ_h^-. The dominant modulation vectors for both edges have the same magnitude, Q* but their most intense direction are rotated 45 degrees from one another.

amplitude was augmented by 5% and then added in quadrature to the left edge PSD.

APPENDIX FOR CHAPTER 7 H

TEMPERATURE DEPENDENCE OF TH-SITE DOS

To further demonstrate that the Th-sites develop a resonance feature in the DOS the temperature dependence of the conductance spectra is plotted in figure H.1. As the temperature drops below the point where heavy bands start to form, near 16K, the conductance spectra begin to show the accumulation of spectral weight near the chemical potential. In contrast to non-Th sites (see chapter 5), where the lowering of temperature mostly redistributes spectral weight, there seems to be no complete compensating diminishment of spectral weight within the plotted energy window, even when the weakly changing background is accounted for.

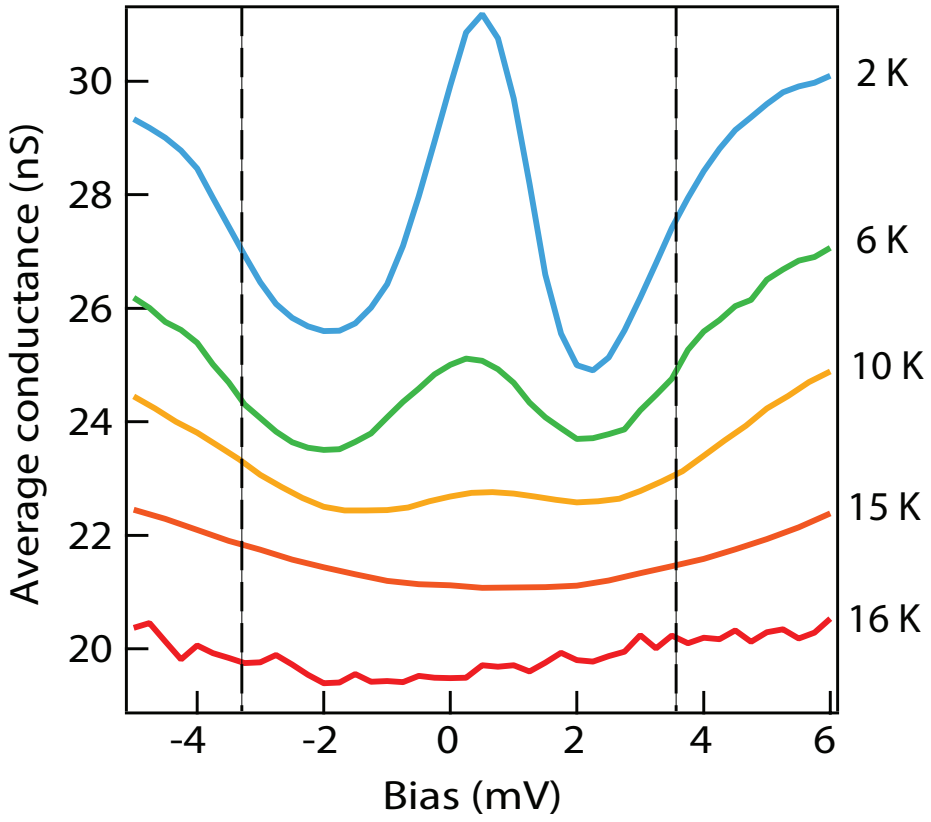

Figure H.1: Temperature dependence of DOS at Th sites. Starting at temperatures coinciding with the formation of heavy bands, the DOS at the Th sites, develops a resonance structure. In contrast to other locations which mostly show a redistribution of spectral weight around the chemical potential, the Th-site spectra show a growing peak against the background without compensating depressions elsewhere.

REFERENCES FOR CHAPTER 7

[1] Maple, M., Chen, J., Dalichaouch, Y., and Kohara, T. *Physical Review Letters* **56**, 185–188 (1986).

[2] Lopez, A., Visani, P., Dalichaouch, Y., Lee, B. W., and Maple, M. B. *Physica B* **179**, 208–214 (1992).

[3] Schoenes, J., Schönenberger, C., and Franse, J. *Physical Review B* **35**, 5375–5378 (1987).

[4] Ohkuni, H., Inada, Y., Tokiwa, Y., Sakurai, K., Settai, R., Honma, T., Haga, Y., Yamamoto, E., Nuki, Y., and Yamagami, H. *Philosophical Magazine B* **79**(7), 1045–1077 (1999).

[5] Hassinger, E., Knebel, G., Matsuda, T., Aoki, D., Taufour, V., and Flouquet, J. *Physical Review Letters* **105**, 216409 November (2010).

[6] Santander-Syro, A. F., Klein, M., Boariu, F. L., Nuber, A., Lejay, P., and Reinert, F. *Nature Physics* **5**(9), 637–641 July (2009).

[7] Yoshida, R., Nakamura, Y., Fukui, M., Haga, Y., Yamamoto, E., nuki, Y., Okawa, M., Shin, S., Hirai, M., Muraoka, Y., and Yokoya, T. *Physical Review B* **82**, 205108 November (2010).

[8] Madhavan, V., Chen, W., Jamneala, T., Crommie, M. F., and Wingreen, N. *Science* **280**, 567–569 April (1998).

[9] Li, J., Schneider, W.-D., Berndt, R., and Delley, B. *Physical Review Letters* **80**, 2893–2896 March (1998).

[10] Manoharan, H., Lutz, C., and Eigler, D. *Nature* **403**(6769), 512–515 February (2000).

[11] Knorr, N., Schneider, M., Diekhöner, L., Wahl, P., and Kern, K. *Physical Review Letters* **88**(9), 096804 February (2002).

[12] Otte, A. F., Ternes, M., von Bergmann, K., Loth, S., Brune, H., Lutz, C. P., Hirjibehedin, C. F., and Heinrich, A. J. *Nature Physics* **4**(11), 847–850 September (2008).

[13] Lin, C., Wallash, A., Crow, J., Mihalisin, T., and Schlottmann, P. *Physical Review Letters* **58**(12), 1232–1235 (1987).

[14] Yokoyama, M., Tenya, K., and Amitsuka, H. *Physica B* **312-313**(1-4), 498–500 March (2002).

[15] Petrovic, C., Budko, S., Kogan, V., and Canfield, P. *Physical Review B* **66**(5), 054534 August (2002).

[16] Lawrence, J., Graf, T., Hundley, M., Mandrus, D., Thompson, J., Lacerda, A., Torikachvili, M., Sarrao, J., and Fisk, Z. *Physical Review B* **53**, 12559–12562 (1996).

[17] Paglione, J., Sayles, T. A., Ho, P.-C., Jeffries, J. R., and Maple, M. B. *Nature Physics* **3**, 703–706 September (2007).

[18] Bauer, E. D., Yang, Y.-f., Capan, C., Urbano, R., Miclea, C., Sakai, H., Ronning, F., Graf, M., Balatsky, A., Movshovich, R., Bianchi, A., Reyes, A., Kuhns, P., Thompson, J., and Fisk, A. *submitted to Proceedings of the National Academy of Sciences* (2011).

[19] Tešanović, Z. *Physical Review B* **34**, 5212–5216 (1986).

[20] Sollie, R. and Schlottmann, P. *Journal of Applied Physics* **69**, 5478–5480 (1991).

[21] Sollie, R. and Schlottmann, P. *Journal of Applied Physics* **70**, 5803–5805 (1991).

[22] Figgins, J. and Morr, D. K. *arXiv:1001.3875v1* (2010).

[23] Wermbter, S., Sabel, K., and Czycholl, G. *Physical Review B* **53**, 2528–2536 February (1996).

[24] Hirschfeld, P., Vollhardt, D., and Wölfle, P. *Solid State Communications* **59**(3), 111–115 (1986).

[25] Hewson, A. C. *The Kondo Problem to Heavy Fermion*. Cambridge University Press, (1993).

[26] Coleman, P. *Heavy Fermions: electrons at the edge of magnetism*, 95–148. John Wiley (2007).

[27] Dordevic, S., Basov, D., Dilley, N., Bauer, E., and Maple, M. *Physical Review Letters* **86**(4), 684–687 January (2001).

[28] Petukhov, K. *Journal of Magnetism and Magnetic Materials* **272-276**, E105–E106 May (2004).

[29] Rotundu, C., Andraka, B., and Schlottmann, P. *Physical Review B* **76**, 054416 August (2007).

CHAPTER 8

FINAL REMARKS

Heavy fermion physics stands as a fantastic example of the profoundly rich phenomena that arise from strong electronic interactions. The work presented in this dissertation has been primarily inspired by the desire to test the fundamental ideas that have been proposed over the last three decades to understand these highly complex systems. In working towards a consistent interpretation of experimental results there is an emerging realization that even the fundamental ideas and their applications are still open research areas, for the vast range of behavior that are attributed to emerge from the Kondo lattice may in fact have alternate origins. Nonetheless, the present set of observations also reaffirm by direct visualization some of the most basic structures believed to underly heavy fermion physics. And in fact, the entrance of SI-STM onto the stage is beginning to inspire a new found interest in readdressing those very ideas which have been taken for granted for so long but have escaped direct measurement. In a system where the highly intertwined worlds of the localized and itinerant strongly define the electronic landscape, a technique capable of probing both of their respective naturally defined spaces is essential.

Of course, there remain a number of topics which were beyond the scope of the present experiments but which represent fundamental areas for research. The original inception of the Kondo lattice by Doniach involved the competition of two energy scales, one which would conceive an antiferromagnet while the other spawn heavy quasiparticles. The boundary of these two regimes has prompted notions of quantum criticality but how exactly the transition occurs in unknown. How the Kondo effect breaks down at such a boundary point,

whether quantum critical or not, defines the next generation of experiments for which SI-STM could be invaluable. Such a research agenda would require a long term effort to find new materials appropriate for STM studies.

However, in the more immediate future, the next steps for SI-STM involve a systematic progression involving a more complete characterization of deemed heavy fermion materials. There remains much uncertainty about the role of Kondo physics, multichannel behavior, multipolar effects, localization effects which although paint a colorful canvas also reveal an understandably tangled perception. And in the same way that SI-STM has greatly enhanced the understanding of unconventional superconductivity in the cuprates, the same potential exists for heavy fermions. The next decade promises to hold a renewed excitement in the fundamental understanding of heavy fermions as experimental, theoretical and computational methods begin to offer new perspectives on a classic field of strong electronic correlations.